University of Alberta

LIGHT DOSIMETRY FOR INTERSTITIAL PHOTODYNAMIC THERAPY: APPLICATION TO THE TREATMENT OF PROSTATIC CARCINOMA

by

Dwayne J. Dickey

A thesis submitted to the Faculty of Graduate Studies and Research in partial fulfillment of the requirements for the degree of **Doctor of Philosophy**.

Department of Electrical and Computer Engineering

Edmonton, Alberta
Fall 2004

Library and Archives Canada

Published Heritage Branch

395 Wellington Street
Ottawa ON K1A 0N4
Canada

Bibliothèque et Archives Canada

Direction du Patrimoine de l'édition

395, rue Wellington
Ottawa ON K1A 0N4
Canada

Your file Votre référence
ISBN: 0-612-95923-6
Our file Notre référence
ISBN: 0-612-95923-6

The author has granted a non-exclusive license allowing the Library and Archives Canada to reproduce, loan, distribute or sell copies of this thesis in microform, paper or electronic formats.

The author retains ownership of the copyright in this thesis. Neither the thesis nor substantial extracts from it may be printed or otherwise reproduced without the author's permission.

L'auteur a accordé une licence non exclusive permettant à la Bibliothèque et Archives Canada de reproduire, prêter, distribuer ou vendre des copies de cette thèse sous la forme de microfiche/film, de reproduction sur papier ou sur format électronique.

L'auteur conserve la propriété du droit d'auteur qui protège cette thèse. Ni la thèse ni des extraits substantiels de celle-ci ne doivent être imprimés ou aturement reproduits sans son autorisation.

In compliance with the Canadian Privacy Act some supporting forms may have been removed from this thesis.

While these forms may be included in the document page count, their removal does not represent any loss of content from the thesis.

Conformément à la loi canadienne sur la protection de la vie privée, quelques formulaires secondaires ont été enlevés de cette thèse.

Bien que ces formulaires aient inclus dans la pagination, il n'y aura aucun contenu manquant.

Canada

For Marcie

Acknowledgements

I must first and most importantly express gratitude and respect to John Tulip and Ronald Moore for their support, guidance, and insight.

I would also like to thank Ben Bathgate for his assistance over the course of this project.

I must extend my appreciation to Ron Sloboda for his detailed and sobering edits to this thesis.

Finally, I must thank Gerald Beaudoin and Kevin Partridge for their patience with my unique personality type.

Contents

1 Introduction **1**

2 Tissue Characterization using the P3 Approximation **9**

2.0.1 Models of Light Propagation 10

2.0.2 Quantification of Light using Transport Theory 11

2.0.2.1 Transport Theory and the Transport Equation . . . 14

2.0.2.2 Transport Theory and the Pn-Approximation . . . 14

2.0.3 Mathematical Theory of the P3 Approximation 17

2.0.4 Grosjean Theory 22

2.1 Validation of the P3 Approximation 23

2.1.1 Plane Wave Geometry. 24

2.1.1.1 Results 27

2.1.2 Spherical Geometry 28

2.1.2.1 Results 32

2.2 Implications 32

3 Predicting Fluence from Cylindrical Diffusing Fibreoptics: Huygens-Diffusion Theory **36**

3.0.1 Light Dosimetry for Interstitial PDT Using Diffusion Theory 37

3.0.1.1 The Huygens Radiator and Formulation of the Fluence for Huygens-Diffusion Theory 38

3.1 Validation of Huygens-Diffusion Formulation 45

3.2 Implications 50

4 Analysis of Prostatic Optical Properties **54**

4.1 Employing the P3 Approximation to Examine Prostatic Optical Properties . . . 55
4.1.1 Discussion . . . 57
4.2 Examination of Boundary Effects . . . 58
4.2.1 Implications . . . 62

5 Photodosimetry System for PDT **64**
5.1 Introduction . . . 64
5.1.1 Comprehensive Light Delivery System. . . . 67
5.2 Light Delivery System . . . 67
5.2.1 Laser Sources . . . 68
5.2.2 Tissue Characterization . . . 68
5.2.3 Fibreoptic Switch . . . 69
5.2.4 Delivery Fibreoptics . . . 71
5.2.5 Control System Software . . . 72
5.2.6 Treatment of Dunning R3327-AT and -H Tumour . . . 74
5.3 Results . . . 75
5.4 Discussion . . . 76
5.5 Treatment of Canine Prostate . . . 77
5.5.1 Method . . . 77
5.5.2 Results . . . 78
5.5.3 Discussion . . . 78
5.6 Conclusions . . . 79

6 PDT Dose: Quantifying Drug and Oxygen **91**
6.1 The Photosensitizer . . . 92
6.1.1 Results . . . 96
6.1.2 Implications . . . 98
6.2 Oxygen and the Photodynamic Dose. . . . 100

7 Conclusion **106**

Bibliography **110**

A Mathematica Formulation of the P3-Approximation for an Isotropic Point Source 116

B Mathematica Formulation of a Huygens-Diffusion Theory 129

C Intra-arterial drug delivery 134

List of Figures

2.1 Geometry for radiance measurements with an isotropic point source 15

2.2 Equipment arrangement for acquiring radiance measurements. . . . 26

2.3 Fibre arrangement for acquiring fluence measurements. The detector probe may be replaced with a radiance probe for measurements from an isotropic source. 26

2.4 Comparing the P3 Approximation radiance and fluence against experimental measurements in Phantom 1. 29

2.5 Comparing the P3 Approximation radiance and fluence against experimental measurements in Phantom 2. 30

2.6 Comparison of the Grosjean Theory (using P3 Approximation generated optical parameters) to experimental fluence measurements. . 31

2.7 Experimental radiance and fluence measurements from an isotropic source compared to the predictions of the P3 Approximation in Phantom 3. 33

2.8 Experimental radiance and fluence measurements from an isotropic source compared to the predictions of the P3 Approximation in a tissue Phantom 4. 34

3.1 Geometry of an isotropic point source. The physical size source is modeled with ρ, with the point source theoretically located at the origin, i.e.$r = \rho = 0$. 40

3.2 Cylindrical source, modeled with an array of infinitesimal point sources aligned on the middle of the diffuser 44

3.3 Comparing the lateral diffusion measurements to those predicted by Huygens-Diffusion Theory radiator. 48

3.4 Fluence measurements in various phantom media as compared with the theoretical values predicted by the Huygens-Diffusion fluence model. The dry field measurements were made in air. The low absorption phantom had optical parameters of σ_s = 22 mm^{-1}, σ_a = 0.001 mm^{-1} and g = 0.81while the absorbing/scattering phantom had optical parameters of σ_s = 22 mm^{-1}, σ_a = 0.07 mm^{-1} and g = 0.81. 49

3.5 Experimental fluence produced by an array of cylindrical diffusers compared to the predictions of Huygens-Diffusion Theory. 51

3.6 Fluence predictions from an array of 3 cylindrical diffusers compared to Huygens-Diffusion Theory 52

4.1 Measurement points used to optically characterize post-mortem prostate. 59

4.2 Typical radiance measurements used predict prostatic optical parameters. 59

4.3 Theoretical examination of the effects of changing prostatic scattering properties on the fluence. 60

4.4 Arrangement to examine boundary effects of the boundary conditions at the prostatic capsule on radiance measurements. 60

4.5 Examination of the change in radiance near the prostatic boundary after the addition of Intralipid 61

5.1 Schematics of the radiance probe. 81

5.2 Schematic of the light delivery system in delivery mode 82

5.3 Schematic of light delivery system in detection mode 83

5.4 Photograph of light delivery system. The control computer is shown in the background. 84

5.5 Icosahedral arrangement of fibre optics. The cylindrical diffuser's long axes run into the plane of the page. 84

5.6 Isodose plots for seven cylindrical fibre optic. Grey indicates the area occupied by the diffuser. Red indicates a high dose; violet indicates the penetration depth. 85

5.7 Gadolinium perfusion MRI of rat implanted with Dunning R3327-H flank tumour. 86

5.8 Rat with Dunning R3327-H tumour treated with the switched light delivery system 87

5.9 Changes in tissue transmissivity during PDT in Dunning R3327-AT and -H tumours. 88

5.10 Hemoglobin absorption from 600 to 770 nm 89

5.11 Monitoring the tissue optical parameters of the large male mongrel dog 89

5.12 Changes in tissue transmissivity during treatment of purpose-bred beagle. 90

6.1 Examination of fluorescence as a function of concentration. 97

6.2 Schematic of delivery system with fluorescence drug detection. . . . 99

6.3 Integration of a pulse oximetry based system into the computer controlled light delivery system. 101

6.4 A plot of Eq(6.5) (α = 0.1), illustrating the temporal change in oxygen concentration. 103

6.5 Comparison of Eq(6.5) (α = 0.052) with the relative changes in light transmissivity in an -H tumour. 104

List of Tables

4.1 Spatial examination of prostatic scattering parameters (see Figure 4.1). σ_a and g remained constant at 0.07 mm^{-1} and 0.96, respectively. 58

List of Symbols

Abbreviations

PDT – photodynamic therapy

PCa – prostatic carcinoma

MC – Monte Carlo

HpD – haematoporphyrin derivative

ALA – 5-aminolaevulinic acid

PPIX – protoporphyrin IX

BPD-MA – benzoporphyrin derivative monoacid ring A

mTHPC – meta-tetrahydroxyphenylchlorin

AlPc – aluminum phthalocyanine

mTHPC – Meta-tetrahydroxyphenyl bacteriochlorin

TRUS – transrectal ultrasound

HbO_2 – oxyhemoglobin

Hb – deoxyhemoglobin

Symbols

$L(\vec{r}, \mu)$ – radiance (specific intensity) [W mm^{-2} sr^{-1}]

$\phi(r)$ – fluence (irradiance) [W mm^{-2}]

r – radius [mm]

σ_s – scattering coefficient [mm^{-1}]

σ_a – absorption coefficient [mm^{-1}]

g – anisotropy factor.

σ_t – total attenuation coefficient [mm^{-1}]

mfp – mean-free-path [mm]

σ_s' – effective scattering coefficient [mm^{-1}]

σ_{tr} – transport coefficient [mm^{-1}]

σ_{eff} – effective transport coefficient [mm^{-1}]

δ – penetration depth [mm]

$P_n(\mu)$ – Legendre Polynomials

λ – wavelength of light

E – extinction coefficient [L mol^{-1} cm^{-1}]

C – concentration [mol L^{-1}]

r_{nec} – radius of necrosis [mm]

t – time [s]

$E_1(x)$ – exponential integral

P_{th} – threshold toxic product [photons mm^{-3}]

Φ – quantum efficiency

Chapter 1

Introduction

Prostatic Carcinoma (PCa) is the most common occurring cancer among men. One in 8 men will develop prostate cancer during his lifetime. One in 28 will die from the disease. Prostate cancer will account for over 86% of cancer related deaths in men over 70 [National Cancer Institute of Canada, 2003]. Since 1988, prostate cancer incidence rates have risen by 30%. This is due, in part, to the PSA and its ability to detect earlier stage cancer. Early stage cancer is treatable with conventional methods, but advanced cases of PCa are resistant to conventional treatment modalities: the prostate tends to become resistant to hormone therapy in late stage disease; chemotherapy is generally ineffective against PCa; radiation can control the symptoms of late stage disease but the radiation required to eliminate the disease risks damage surrounding healthy tissues. Thus, a new effective treatment for PCa is needed.

Experimental treatment modalities for localized PCa include cryotherapy, hyperthermia and photodynamic therapy (PDT). In its early development, cryotherapy had equivalent survival rates, stage for stage, as radical prostatectomy but with advanced imaging techniques to guide cryoprobe placement, it is showing encourag-

ing results. However, predicting interstitial temperatures surrounding the ice ball is difficult, even with real-time monitoring, and demarcation of the boundary of injury is typically inaccurate. With the risk of rectal injury, a conservative approach risks survival of peripheral tumour tissue where 80% of PCa occur [McNeil et al., 1986]. Unlike cryotherapy, transillumination of tissue for PDT is potentially more accurate and predictable. Photodosimetry is direct and, at least to the first order, static for a given optical field whereas cryogenic coagulation is secondary to thermal conduction and is hence dynamic.[1]

Photodynamic therapy (PDT) is a potentiall oncological treatment modality requiring 3 components: a photosensitive drug (photosensitizer), an appropriate light source, and oxygen. The photosensitizer, upon accepting a photon of the appropriate wavelength, with the presence of oxygen, produces an environment toxic to cellular components. Clinically, PDT has shown to be an effective treatment for superficial diseases such as bladder, lung, and skin cancers.[Henderson and Dougherty, 1992]. Ideally, a patient would be administered a non-toxic photosensitizer that is preferentially retained by malignant tissues. The sensitizer would be activated by a wavelength of light that penetrates deeply into tissues with tumour destruction being possible with no damage to adjacent tissues [Carruth, 1986]. In the most general terms, the effects of PDT are quantified by the PDT Dose, which describes how much energy absorbed by the photosensitizer in the target volume is converted to a toxic product [MacDonald and Dougherty, 2001]. To determine the PDT dose, all 3 elements of the PDT reaction must be quantified. Presently, there are few methods to quantify the drug dose distribution and oxygen concentration, none of which are presently being used in clinical interstitial PDT. Therefore, for safe PDT, the onus is on accurate light dosimetry. Despite primarily considering the

[1]Tissue undergoes optical transformation during PDT but light transmission is static in unphotosensitized tissues, whereas all tissues will be thermodynamically active.

photophysical component of PDT, clinical implementation of PDT for PCa is still a multidisciplinary problem, requiring the engineered fusion of photophysics and photochemistry to produce a non-invasive, medically viable procedure [Henderson and Dougherty, 1992].

Photodynamic effect was first demonstrated by Raab [1900], showing that acridine orange could kill paramecia. Later, Jesionek and Tappeienner [1903] illustrated that eosin, a relatively non-potent photosensitizer, could kill cancerous tissues. But it was Policard [1924] that showed tumour tissues exhibited more fluorescence than healthy tissues—indicating preferential accumulation of the photosensitizer in malignant tissue masses. Ronchese [1954] attempted to exploit this effect to create a visual demarcation between malignant tissues and healthy tissues. Using a different photosensitizer, hematoporphyrin derivative (HpD), Lipson et al. [1964] exploited preferential accumulation in malignant tissues to detect cervical cancer, also observing that this photosensitizer could kill the cancerous tissues. Dougherty [1974] rediscovered the implementation of fluorescein for the treatment of cancer. After discovering that singlet oxygen was the toxic species in PDT [Weishaupt et al., 1976], Dougherty implemented the more phototoxic HpD to show that PDT could successfully treat and destroy murine tumour models [Dougherty et al., 1975]. This landmark success in PDT was sadly replete with technological limitation. The combination of xenon arc lamp, lenses and filters functioned to deliver the necessary 630 nm light for superficial treatment of implanted tumours. However, with this equipment, only superficial malignancies could be treated. Furthermore, models or methods of determining the amount of light energy delivered to the tumour were not studied and a correlation between the efficacy of PDT to the amount of photosensitizer and light could not be easily drawn.

With the advent of commercially available tuneable lasers and fibreoptic technologies, PDT went through a rebirth, spurring development of both light delivery and

photosensitizers. Lasers gave physicians and researchers the flexibility to deliver a predictable and reproducible amount of light to a target. Fibreoptics terminated in different geometrical diffusers could be used to tailor the light according the geometry of the patient's illness, permitting light to be delivered to virtually any place in the body with minimal trauma to the patient. Early studies showed that the scattering and absorbing characteristics of light in human tissues varied with respect to wavelength, that the optics of tissues varied between patients and that longer wavelengths passed more readily through most human tissues, until about 800nm when the water absorption becomes significant [Wilkisch and Jacka, 1984]. The chemical composition of HpD was studied and purified to create the photosensitizer, Photofrin® (which also preferentially absorbs light energy at 630 nm). Photofrin® was approved for use in the United States in the 1980s (with Canada following shortly thereafter), producing a benchmark for which technology could strive. Photodosimetry studies then became focused around the photodynamics of Photofrin® and 630 nm light. PDT proved to be a powerful oncological diagnostic and treatment modality. However, it was primarily limited to the treatment of superficial malignancies. Many began to theorize that PDT could be used to treat solid malignancies, such as prostate cancer. Prostate cancer is multifocal, necessitating photodestruction of the entire gland to confidently eradicate the disease[Arnfield et al., 1989]. Because of the limited transmission of 630nm light, this would necessitate multiple fibreoptic sources for uniform irradiation [Bolin et al., 1987]. However, for interstitial treatment, the ratio of Photofrin® accumulation in malignant tissues to healthy tissues was not significant enough to avoid damage to proximate tissues without careful light dosimetry. Accurate tissue characterization and proper light dosimetry would potentially enable a lethal dose of light to be delivered to the periphery of the gland (or any solid internal malignancy for that matter). Several different models for light dosimetry have been explored, but most methods were ei-

ther clinically infeasible in that they did not provide results in a timely fashion, were too invasive, and/or were not accurate. In particular to the treatment of prostatic carcinoma, many *in-vivo, ex-vivo* or animals models were studied to determine the optics of prostatic tissue at the 630 nm wavelength used to photoactivate Photofrin® [Arnfield et al., 1992, 1993, Chen and Hetzell, 1998], resulting in a reasonable notion of light dosimetry; although, it was still difficult to predict light energy levels close to the source and boundaries where accurate dosimetry was most necessary. Further studies, however, illustrated that tissue optics would be dynamic over the course of the PDT reaction [Chen et al., 1997]. Therefore, dosimetry would also have to account for the changes in tissue optics due to PDT itself.

Photofrin® has some clinical disadvantages: the relatively poor penetration of 630 nm light and an extended period of cutaneous photosensitivity of approximately 6 weeks that followed treatment, during which a patient would have to avoid any sort of bright light. The next generation of photosensitizers that were developed were taken up more rapidly by tissues, cleared faster and photoactivated at longer wavelengths [MacDonald and Dougherty, 2001]: AlPc (680 nm), Foscan (652 nm) and BPD-MA (690 nm). However, the optics of tissues at longer wavelengths have not been extensively studied, once again resulting in difficulty determining how the drug/light combination was related to photodynamic effect in the target. However, many people still attempted treatment of the prostate in both animal and human models [Chen et al., 1997, Lee et al., 1997, 1999]. Conservative approaches were generally taken to ensure that surrounding tissues were not harmed. As of 1998, there were still no accurate, clinically viable methods of determining interstitial tissue optics, calculating light fields or monitoring the progress of PDT; as a result, the clinical implementation of PDT remained limited to superficial disease. Since PDT has shown to be an effective treatment for even the most refractory prostatic tumour cell lines, there is reason to continuing research into the application of PDT

to PCa [Xiao et al., 2002]. A general, minimally invasive tool for determining tissue optical parameters is needed for both research and clinical environments. Furthermore, accurate representation of the light fields are required to safely determine the region of photodynamic necrosis, but this requires knowledge of the target optical parameters. Finally, a method of efficiently delivering and monitoring interstitial PDT is required.

Exploiting the technological advances in computer, laser and fibreoptic technology, to create a solid photophysical foundation using an novel implementation of Transport Theory, this thesis delineates the light dosimetry and hardware implementation for interstitial PDT, focusing on the treatment of prostatic carcinoma. The mathematics and protocols may be extended to treat any solid interstitial malignancy. In particular, the following concepts will be addressed:

Chapter 2 - Tissue Characterization using the P3 Approximation: The first step to accurate light delivery is determining the tissue optical parameters. The P3 Approximation is an approximate solution to the Transport Equation that provides an analytical solution to determine tissue optical parameters. This fast, elegant method of calculating optical parameters is a minimally invasive method that supplies the necessary information for accurate light delivery. The P3 Approximation is validated by comparing its calculated predictions to the known optical parameters of a tissue phantom in 2 geometries: 1 dimensional plane-wave and 3-dimensional with an isotropic point source.

Chapter 3 - Predicting Fluence from Cylindrical Diffusing Fibreoptics: Huygens-Diffusion Theory: Clinical irradiation of disease is primarily achieved using fibreoptics terminated with a cylindrical diffusing tip; and therefore, a method of predicting the light distribution from these cylindrical sources is necessary. Using Huygens' theory as basis of wavefront propagation and a unique implementation

of Diffusion Theory, this chapter describes how a cylindrical light source can be mapped as a finite array of infinitesimally small point sources. To predict light distribution, one requires *a priori* knowledge of the target optical parameters. The optical parameters are supplied by the P3 Approximation, described in Chapter 2.

Chapter 4 - Analysis of Prostatic Optical Properties: Every PDT session must be individually tailored for each patient; however, a baseline knowledge of the optical behavior of the target tissue is prudent. Prostatic optical parameters have been studied, but results are inconsistent and primarily limited to 630 nm light. Therefore, using the P3 Approximation, the optical properties of *postmortem* prostate is studied and implications of the findings to *in vivo* application are explained.

Chapter 5 - Photodosimetry System for PDT: Combining the mathematical theory in Chapters 2 and 3, with the practical knowledge of prostate optics of Chapter 4, this section describes a prototype light delivery and monitoring system for PDT. This comprehensive light delivery system is capable of predicting tissue optical parameters, calculating the necessary light fields for PDT and monitoring the changes in tissue transmissivity. Some preliminary results in the treatment of Dunning R3327-H and -AT flank tumours are detailed, and preliminary results treating canine prostate are given.

Chapter 6 - PDT Dose: Quantifying Drug and Oxygen: There are several resolutions that must be made in order to bring PDT to full clinical realization, namely the quantification of photosensitizer and oxygen (the 2 other components for a photodynamic reaction). Both drug and oxygen levels can be quantified, but methods employable in clinical PDT have not been developed. Fluorescence detection of the photosensitizer is a promising method of quantifying the drug detection and the status of the PDT reaction. Similarly, oxygen quantification could be indirectly quantified using a practice similar to the clinically used pulsed oximetry. Both

methods are optical in nature and could potentially be integrated into the dosimetry system described in Chapter 5.

Chapter 2

Tissue Characterization using the P3 Approximation

There are two classes of measurements that may be used to determine tissue optical parameters: direct and indirect [Wilson et al., 1987]. Direct methods use thin tissue samples[1] from which the fractional light absorbance or the scattered light flux is directly measured to determine the optical coefficients. Indirect methods are based on bulk models from which the optical parameters are determined by applying at least one light propagation model. Human tissues tend to have high albedo and have small mean-free-paths,[2] which complicates direct measurement techniques since optically thin samples are hard to obtain. When the samples are thin enough to avoid multiple scattering, the microscopic inhomogeneities of tissue become evident. Furthermore, direct measurements are virtually impossible to obtain, since a sample must be removed and prepared for measurement. Therefore, to use direct measurements, one must study the optical parameters of *postmortem* tissue samples, but it is unknown if *postmortem* tissue is optically similar to an *in*

[1] Samples must be thin enough that multiple photon scattering is negligible.
[2] Albedo and mean-free-path are further discussed in §2.0.2

vivo specimen. Furthermore, it is unknown how the prostatic optical parameters will change between patients. To be safe, light delivery should be tailored for each patient with tissue characterization directly preceding treatment. Hence, an *in vivo* measurement is necessary.

Indirect techniques can be used in bulk samples and may therefore be performed *in vivo*; yet, indirect measurements still have some key limitations: it is impossible to know the optical parameters for all points in the tissue volume; indirect techniques must account for detector and source geometries. Approximations to the propagation models simplify calculations tend to be made to light propagation models, which can limit its general utility, save for the geometry in which the approximations were made. For example, Diffusion Theory, in some of its forms, is accurate only away from sources and boundaries, and within a certain range of optical characteristics.[3] Still, for application to PDT, indirect methods are preferred for determining *in vivo* tissue optics since procuring and analyzing tissue samples for clinical application is unrealistic.

2.0.1 Models of Light Propagation

Most light propagation models pre-date PDT. Several models are capable of predicting radiation transport in turbid media (such as human tissues): computational models such as Monte Carlo [Wilson and Adam, 1983], a rigorous approach using Maxwell's Equations [Ishimaru, 1978] and Transport Theory [Sen and Wilson, 1990]. Monte Carlo (MC) can reliably predict tissue optical parameters; however, MC requires a great deal of computing power and time. Even with modern computing powers, the time required for MC is generally too long for clinical application. Every tissue in the human body is sufficiently inhomogeneous that it is impossible

[3]Diffusion Theory is discussed further in Chapter 3

to monitor diffraction and polarization, rendering a rigorous solution to Maxwell's Equations an infeasible approach for determining tissue optics. By ignoring polarization and diffraction effects, photons may be treated as propagating neutral particles. Under such conditions, Transport Theory may be invoked to model light propagation through tissue. Transport Theory is equivalent to Maxwell-Boltzmann Kinetic Theory of Gases, and is capable of analytically predicting the movement of uncharged radiation through turbid media. Compared to numerical solutions (like MC), analytical solutions can be rapidly calculated, which offers clinical utility for PDT [Star, 1989]. Since Transport Theory satisfies speed and accuracy requirements, yet is general enough to be used in a wide variety of applications, it is the preferred light propagation model for PDT. It should be known that MC still has some clinical application. Its reliability provides a basis against which other propagation models can be compared [Wilson and Adam, 1983, Prahl et al., 1989].

2.0.2 Quantification of Light using Transport Theory

There are 2 basic parameters used to quantify light energy. Radiance, $L(\vec{r}, \mu)$ (also known as specific intensity), quantifies the light power impinging upon a point in space, at a specific angle (units of [W m^{-2} sr^{-1}]), where the position is represented by $\vec{r}$ and $\mu = \cos\theta$. The angle θ represents the angle between the coordinate system origin and the orientation in which the radiance is measured.[4] Fluence, $\phi(r)$, quantifies the total light impinging upon a point in space from all angles (units of [W m^{-2}]). Radiance and fluence are related through the simple equation

$$\phi(r) = \int_{4\pi} L(r, \mu) d\omega \tag{2.1}$$

For PDT light dosimetry, we ultimately want to know $\phi(r)$ at all points in the target

[4]In general coordinates, $L(\vec{r}, \mu)$ will often be written as $L(\vec{r}, \hat{s})$ as in Eq(2.3) . See Figure 2.1.

volume to the quantity light energy in order to prevent damage to proximate tissues. To calculate either the radiance or the fluence, the optical parameters of the medium must be known. All of the coefficients describe slightly different physically statistical distributions in tissue. All the coefficients are based on the 3 main, independent optical parameters used to describe light-matter interactions in Transport Theory :

σ_s– scattering coefficient [mm^{-1}];

σ_a– absorption coefficient, [mm^{-1}]; and

g – anisotropy factor.

Both σ_s and σ_a are coefficients describing the likelihood of a photon undergoing either a scattering or absorption event, respectively, per unit pathlength in tissue. The anisotropy factor, g, indicates the cosine of the average angle through which light will be scattered, if it is scattered. Through the combination of σ_s, σ_a and g, similarly named coefficients are used to describe light propagation, most of which are artefacts from solutions to Eq(2.1).

σ_t, the total attenuation coefficient ($\sigma_t = \sigma_s + \sigma_a$), with units of mm^{-1}, describes the probability of a photon interaction occurring.

Using σ_t, the albedo and mean-free-path can be defined. The albedo is the ratio of the scattering coefficient to the total attenuation coefficient,

$$\text{Albedo} = \frac{\sigma_s}{\sigma_t} .$$

Most tissues in the human body, save dark organs like the liver and spleen, have an albedo close to unity, i.e. $\sigma_s/\sigma_t > 0.99$ [Doiron et al., 1982]. The mean-free-path indicates the distance a photon will travel before undergoing either scattering or absorption, and is described as

$$\text{mfp} = \frac{1}{\sigma_t} .$$

The optical parameters listed hereafter emerge from the solutions to the Diffusion

Equations.[5] The reduced scattering coefficient, σ_s',

$$\sigma_s' = \sigma_s(1 - g),$$

describes accumulation of light from scattering. In a medium where light scattering is isotropic ($g = 0$), σ_s' reduces to the scattering coefficient. In a completely forward scattering medium ($g = 1$), $\sigma_s' = 0$, indicating no light will ever be scattered back to the detection point. The distance between scattering events is intuitively calculated by its inverse, $\frac{1}{\sigma_s'}$.

Using the reduced scattering coefficient, we can define the transport coefficient as $\sigma_{tr} = \sigma_a + \sigma_s'$, which also accounts for possible scattering and absorption events. In a completely anisotropic medium ($g = 1$), the transport coefficient reduces the absorption coefficient.

The effective transport coefficient, σ_{eff}, emerges from solutions to the Diffusion Equations:

$$\sigma_{eff} = \sqrt{3\sigma_a(\sigma_a + \sigma_s')}.$$

The inversion of σ_{eff} describes the (total) penetration depth of a photon, δ, which is defined as

$$\delta = \frac{1}{\sqrt{3\sigma_a(\sigma_a + \sigma_s')}}. \tag{2.2}$$

It has been suggested that resolution of δ is of primary importance in order to determine photodynamic kill effect [Jacques, 1992]. For prostatic tissue, $\delta_{514nm} \approx 1$ mm, $\delta_{630nm} \approx 4$ mm, $\delta_{690nm} \approx 8$ mm. Therefore, longer wavelengths of light are generally preferred for interstitial PDT applications since a lethal light dose to a larger volume.

[5]Diffusion Equations are shown by Eq(3.1) and Eq(3.2), and will be solved in Chapter 3.

2.0.2.1 Transport Theory and the Transport Equation

Originating in 1903 as the theory of radiative transfer, Transport Theory has been used to solve problems relating to atmospheric visibility, marine biology, and neutron transport [Ishimaru, 1978]. Central to Transport Theory is the transport equation (also known as the equation of radiative transfer), which is equivalent to the Maxwell-Boltzmann collision equation. In general coordinates, for a homogeneous medium, the Transport Equation is

$$\hat{s} \cdot \nabla L(\vec{r}, \hat{s}) + \sigma_t L(\vec{r}, \hat{s}) = \sigma_s \int_{4\pi} L(\vec{r}, \hat{s}') f(\hat{s}', \hat{s}) d\hat{s}' + S(\vec{r}, \hat{s}) \tag{2.3}$$

where

$\hat{s}$ – the unit vector in the direction of measurement;

$\hat{s}'$ – the unit vector directed towards the source;

$f(\hat{s}', \hat{s})$ – the scattering phase function, which describes the probability of scatter from $\hat{s}'$ to direction$\hat{s}$; and

$S(\vec{r}, \hat{s})$ – the source function (specific to geometry of the source and detectors).

2.0.2.2 Transport Theory and the Pn-Approximation

An examination of Eq(2.3) reveals that exact solutions to the transport equation are difficult to obtain: documented exact solutions only exist for a 1-dimensional, source free ($S(r) = 0$) transport equation[Sen and Wilson, 1990]. There are, however, a number of approximations that will furnish accurate, analytical results in a variety of geometries. One of these, the Pn-Approximation [6] is a classical approximation to the transport equation [Chandrasekhar, 1960]. In this solution, the

[6]The Pn-Approximation is also referred to as "the method of spherical harmonics".

Figure 2.1: Geometry for radiance measurements with an isotropic point source

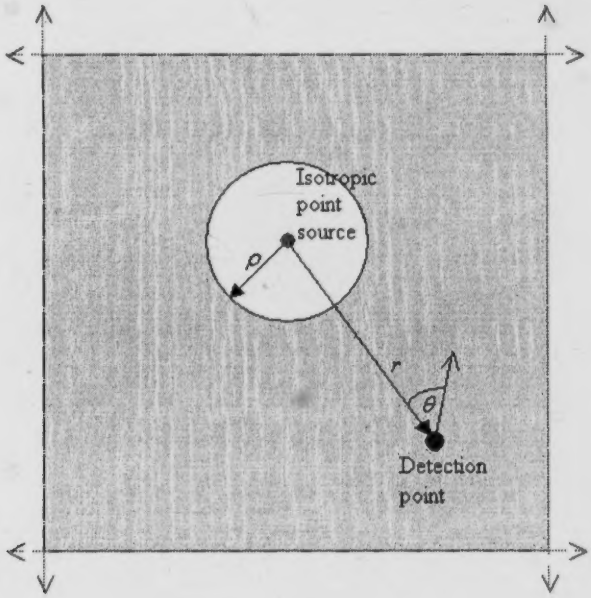

radiance, $L(\vec{r}, \hat{s})$, is decomposed into independent angular and spatial components with the angular component represented by Legendre Polynomials, such that

$$L(\vec{r}, \hat{s}) = \frac{1}{4\pi} \sum_{i=0}^{\infty} (2i + 1) L_i(\hat{r}) P_i(\hat{s} \cdot \hat{s}'). \tag{2.4}$$

This is an intuitively reassuring solution since the Legendre Polynomials form a complete orthogonal basis set in many boundary value problems in spherical coordinates. One may truncate the series solution at any value of n, with increasing accuracy for increasing n. The Pn-Approximation has been shown to be an accurate method of determining radiative transfer (assuming that Transport Theory is indeed representative of the behavior of uncharged radiation). Sen and Wilson [1990] compared the results of the source free ($S(r) = 0$), 1-dimensional P3 Approximation and P5-Approximation in a homogeneous medium to an exact solution of the transport equation in the same geometry, finding approximately 10% variation with the P1-

Approximation, less than 5% variation with the P3 Approximation and less than 1% variation with the P5-Approximation when compared to the exact solution, with accuracy increasing for all approximations as the radius from the sources increased.

Two extensions of the Pn-Approximation have been applied to PDT, but only one has been used in clinical application. The first extension is Diffusion Theory, which truncates the series solution after the first 2 terms of Eq(2.4)). and assumes that the medium is isotropic: $\frac{\sigma_s}{\sigma_t} > 0.99$.[7] Diffusion Theory is the classical method used in PDT to determine tissue optical parameters and calculating the delivered light dose. Diffusion Theory has been used to reproducibly predict the optical parameters of wide array of tissues [Welch and van Gemert, 1995, Wilson et al., 1987, Lilge and Wilson, 1993]. Diffusion Theory quantifies light by the fluence, $\phi(r)$. To use Diffusion theory to calculate tissue optical parameters, one must accurately vary the source-to-detector distance. This is possible yet impractical for interstitial clinical applications. As well, the most commonly used Diffusion formulations are only accurate away from sources and boundaries.

The second implementation of the Pn-Approximation is P3 Approximation (which truncates the solution after the first 4 terms of Eq(2.4)); although clinically applicable, its utilization in PDT was limited to theoretical application. In a plane wave geometry, Star [1989] illustrated that the results of the P3 Approximation correlated with the predictions of Monte Carlo simulations. Radiance furnished by the P3 Approximation potentially overcomes most of the limitations of Diffusion Theory, namely the albedo requirements and the spatial requirements for accurate Diffusion measurements. Radiance data are obtained by setting the detector a known distance from the source, then rotating the detector (a radiance probe) about a single point in space to obtain a complete profile of the angular dependence of light flux passing

[7]Diffusion Theory is occasionally referred to as the P1-Approximation, but should be considered a separate entity from the Pn-Approximation because of the albedo requirements to maintain its validity.

through the point. This single space measurement is minimally invasive and potentially more accurate, offering a clear advantage to the P3 Approximation over using Diffusion Theory for determining optical parameters of a tissue volume, where the source-to-detector distance must be varied to extract the optical parameters. Of course, higher order approximations than $n = 3$ exist, but are difficult to use in practical situations, requiring more boundary conditions and exponentially greater computing requirements to accurately resolve the radiance [Sen and Wilson, 1990].

By first using the theory of the P3 Approximation in a plane wave geometry (described in detail by Star [1989] and Dickey et al. [1998]), this chapter explores the methodology of obtaining experimental radiance measurements and confirms the accuracy of the P3 Approximation to predict the optical parameters of tissue phantoms in this simple geometry. With confidence in its potential, the novel derivation of the P3 Approximation with an isotropic point source is detailed to create a physically viable radiance model. The predictions of the 3-dimensional model are then compared against the known optical parameters of Intralipid tissue phantoms.[8]

2.0.3 Mathematical Theory of the P3 Approximation

The geometry for an isotropic point source is shown earlier in Figure 2.1. The radius, ρ, models the physical dimensions of the spherical source, in which an isotropic point source is located at $r = \rho = 0$. A solution will exist for any $r > \rho$. To obtain the radiance in this geometry, one starts with the transport equation in spherical coordinates with an isotropic point source:

$$\mu \frac{\partial}{\partial r} L(\vec{r}, \mu) + \frac{(1-\mu^2)}{r} \frac{\partial}{\partial r} L(\vec{r}, \mu) + \sigma_t \frac{\partial}{\partial r} L(\vec{r}, \mu) = \sigma_s \int_{-1}^{1} f(\mu') L(\vec{r}, \mu') d\mu' + \frac{P_0 \sigma_s e^{-\sigma_t r} f(\mu)}{16\pi^2 r^2}, \tag{2.5}$$

[8] Intralipid tissue phantoms are explained further in §2.1

with

$\mu = \cos\theta$;

$f(\mu)$ – scattering phase function (see Eq(2.7) below); and

P_0 – the initial power of the source.

The basis of the P3 Approximation is that we propose a solution of the form:

$$L(r,\mu) = \sum_{i=0}^{3}(2i+1)L(r)P_i(\mu). \tag{2.6}$$

For the Pn-Approximation, the scattering phase function is also written as a series of Legendre Polynomials [Davison, 1957], such that $f(\mu) = \sum_{i=0}^{\infty}(2i+1)b_nP_i(\mu)$. The scattering phase function describes the distribution of the scattered light from a single scattering event. The Heyney-Greenstein scattering phase function has been shown to be a reliable method of describing the scattering pattern in tissues Flock et al. [1986]. It is represented by setting $b_n = g^n$, such that

$$f(\mu) = \sum_{n=0}^{3}(2n+1)g^nP_n(\mu). \tag{2.7}$$

Eq(2.7) and Eq(2.6) are substituted back into Eq(2.5), which is then multiplied by $P_m(\mu)$ and integrated over all space ($4\pi\, sr$). Using the orthogonality relations,

$$\int_{-1}^{1}P_n(x)P_m(x) = \frac{\delta_{mn}}{2n+1},$$

$$(1-x^2)\frac{\partial}{\partial x}P_n(x) = nP_{n-1}(x) - nxP_n(x),$$

and

$$(2n+1)P_n(x) = (n+1)P_{n+1}(x) + nP_{n-1}(x),$$

we obtain the following differential equation, which is dependent only upon r:

$$\begin{aligned} &\tfrac{\partial}{\partial r}[(n+1)L_{n+1}(r) - nL_{n-1}(r)] + \\ &\tfrac{1}{r}[n(n+1)L_{n-1}(r) - n(n+1)L_{n+1}(r)] + 2(2n+1)\sigma_t L_n(r) \;=\; \tfrac{1}{2\pi}(2n+1)^2\sigma_s g L_n(r) + \tfrac{P_0 g^n}{16\pi^2 r^2}(2n+1)e^{-\sigma_t r}. \end{aligned} \tag{2.8}$$

The solution to the differential equation, Eq(2.8), is a summation of the particular and homogeneous (source free) equations, such that:

$$L(r) = L_{part}(r) + L_{homo}(r).$$

A particular solution is proposed, of the form:

$$L_n(r) = A_n e^{-\sigma_t r}. \tag{2.9}$$

This solution is an intuitive classical description of the attenuation of uncharged radiation [Chandrasekhar, 1960, Ishimaru, 1978, Attix, 1986]. Substituting Eq(2.9) back into Eq(2.8) and taking $n = 0, 1, 2, 3$, we obtain 4 linear equations for A_n, shown below in matrix form:

$$\begin{bmatrix} \frac{-\sigma_s}{4\pi} + \sigma_t & -\sigma_t & 0 & 0 \\ \frac{2}{r} - \sigma_t & 3\left[\frac{-9g\sigma_s}{4\pi} + \sigma_t\right] & \frac{-2}{r} - 2\sigma_t & 0 \\ 0 & \frac{6}{r} - 2\sigma_t & 5\left[\frac{-5g^2\sigma_s}{4\pi} + \sigma_t\right] & \frac{6}{r} - 3\sigma_t \\ 0 & 0 & \frac{12}{r} - 3\sigma_t & 7\left[\frac{-7g^3\sigma_s}{4\pi} + \sigma_t\right] \end{bmatrix} \begin{bmatrix} A_0 \\ A_1 \\ A_2 \\ A_3 \end{bmatrix} = \begin{bmatrix} \frac{P_0\sigma_s e^{r\sigma_t}}{16\pi^2 r^2} \\ \frac{P_0\sigma_s g e^{r\sigma_t}}{16\pi^2 r^2} \\ \frac{P_0\sigma_s g^2 e^{r\sigma_t}}{16\pi^2 r^2} \\ \frac{P_0\sigma_s g^3 e^{r\sigma_t}}{16\pi^2 r^2} \end{bmatrix}$$

The system for A_n is easily soluble. Having obtained the particular solution, one must find a solution to the homogeneous (source free) equation. The homogeneous solution is obtained implementing the exact same steps used to find the particular

solution. Thus, we propose a homogeneous solution of the form:

$$L_n(r) = B_{mn} e^{\sigma_{0n} r}. \tag{2.10}$$

This will also give 4 linear equations for 16 coefficients, such that $B_{mn} = B_{mn} C_n$. The quantity, σ_{0n}, is akin to σ_t, shown in Eq(2.9). The set of equations is listed in Eq(2.11), in matrix form.

$$\begin{bmatrix} \frac{-\sigma_s}{4\pi} + \sigma_t & -\sigma_{0n} & 0 & 0 \\ \frac{2}{r} - \sigma_{0n} & 3\left[\frac{-3g\sigma_s}{4\pi} + \sigma_t\right] & \frac{-2}{r} - 2\sigma_{0n} & 0 \\ 0 & \frac{6}{r} - 2\sigma_{0n} & 5\left[\frac{-5g^2\sigma_s}{4\pi} + \sigma_t\right] & \frac{6}{r} - 3\sigma_{0n} \\ 0 & 0 & \frac{12}{r} - 3\sigma_{0n} & 7\left[\frac{-7g^3\sigma_s}{4\pi} + \sigma_t\right] \end{bmatrix} \begin{bmatrix} B_{0n} \\ B_{1n} \\ B_{2n} \\ B_{3n} \end{bmatrix} = \begin{bmatrix} 0 \\ 0 \\ 0 \\ 0 \end{bmatrix} \tag{2.11}$$

Setting $B_{0n} = 1\, C_n$, we can recursively find B_{1n}, B_{2n}, B_{3n}. For a homogeneous system of equations to have a solution, the determinant of the coefficients of the system must be equal to zero. Rewriting Eq(2.11) as $\widetilde{D}\widetilde{B} = 0$, we therefore require that the determinant of $\widetilde{D}$ is equal to zero ($\det \widetilde{D} = 0$), thereby resulting in an easily soluble quartic equation for σ_{0n}. The smallest σ_{0n} is the effective transport coefficient, indicating the effective depth that diffuse radiation radiation will penetrate.[9]

Combining the homogeneous and particular solutions, we obtain a final solution for

[9]The details of the Mathematica® calculations and final form of A_n, B_{mn}, and σ_{0n} are included in Appendix A.

the radial component of the radiance:

$$L_i(r) = (\sum_{j=0}^{3} B_{ij} e^{\sigma_{0i} r}) + A_i e^{-\sigma_i r}. \tag{2.12}$$

Eq(2.12) is introduced back into Eq(2.6) to obtain the complete solution for the radiance, finally giving:

$$\begin{aligned} L(r,\mu) \;=\; & (\sum_{i=0}^{3}(2i+1)B_{0i}P_i(\mu))C_0 e^{\sigma_{00} r} + (\sum_{i=0}^{3}(2i+1)B_{1i}P_i(\mu))C_1 e^{\sigma_{01} r} + \\ & (\sum_{i=0}^{3}(2i+1)B_{2i}P_i(\mu))C_2 e^{\sigma_{02} r} + (\sum_{i=0}^{3}(2i+1)B_{3i}P_i(\mu))C_3 e^{\sigma_{03} r} + \\ & \sum_{i=0}^{3}(2i+1)A_i P_i(\mu) e^{-\sigma_i r}. \end{aligned} \tag{2.13}$$

Because we require a bounded solution is required such that $L(\infty, \mu) = 0$, this forces $C_2 = C_3 = 0$. The final coefficients C_n are determined by applying the boundary conditions to the complete solution. For this formulation, the Fresnel Reflection function is used to describe the boundary conditions at $r = \rho$. Modeling the environment at $r < \rho$ as being optically clear, and at $r > \rho$ as a scattering environment, the Fresnel boundary condition for unpolarized light takes the form:

$$\int_0^1 R(\mu) L_s(\rho, \mu) P_s(\mu) d\mu = \int_{-1}^0 -L_s(\rho, \mu) P_s(\mu) d\mu, \tag{2.14}$$

where $R(\mu)$ is the Fresnel reflection factor and $L_s(\rho, \mu)$ is the radiance on the surface of the source (refer to Figure 2.1). Essentially, Eq(2.14) indicates the light that is reflected will be a function of the light that is transmitted. Eq(2.14) assumes that the light strikes the boundary at $r = \rho$ perpendicularly. For light in medium 1 incident on the boundary with medium 2 ($n_2 > n_1$), at an angle of θ_2, the Fresnel reflection

function can be approximated with

$$R_1(\theta_1) = 1 + D_1[e^{-\alpha_1 \cos\theta_1} - 1]. \tag{2.15}$$

The coefficients D_1 and α_1 are calculated by fitting to the Fresnel formula at $\cos\theta_1 = 0.5$ and $\cos\theta_1 = 1$. This approximation of the Fresnel reflection function is accurate within 1% [Keijzer et al., 1988]. The coefficients C_1 and C_2 are determined by inserting Eq(2.15) into Eq(2.14). We have 2 remaining unknown coefficients, so 2 equations are needed, which can be resolved by setting $s = 1$ and $s = 3$. This boundary condition is commonly evoked in Transport Theory and is described in further detail by Star [1989].

With a solution for the radiance, one integrates over all space to obtain a solution for the fluence, as illustrated in Eq(2.1). Readily exploiting the orthogonality properties of the Legendre polynomials, one obtains the following expression for the fluence:

$$\phi(r) = 4\pi L_0(r) + \frac{P_0 \sigma_s e^{-\sigma_t r}}{4\pi r^2} \tag{2.16}$$

2.0.4 Grosjean Theory

The Grosjean Theory is another approximate solution to determine light transport in turbid media [Grosjean, 1956]. It has a relatively simple formalism, which accurately predicts the fluence away from the sources and boundaries. For an isotropic point source, it is given by

$$\phi_{grosjean}(r) = \frac{\gamma}{4\pi D r} e^{-\alpha r} + \frac{1}{4\pi r^2} e^{-\frac{5kr}{4}}, \tag{2.17}$$

where

$k = \sigma_{tr} + \sigma_a$;

$\alpha \cong \sqrt{3\sigma_a(\sigma_a + \sigma_{tr})}[1 - \frac{2\sigma_a}{5(\sigma_a+\sigma_{tr})}]$;

$D = \frac{\sigma_a}{\alpha^2}$; and

$\gamma = \frac{2\sigma_a}{\sigma_{tr}} \frac{k^2-\alpha^2}{\alpha^2-\sigma_a k}$.

This method has been used extensively to examine the optical parameters of the Dunning R3327-AT tumour and as a fluence model to be used in PDT [Arnfield et al., 1989]. There are obvious similarities between the Grosjean Approximation, Eq(2.17), and the P3-fluence, Eq(2.16). This lends some preliminary confidence that the P3 Approximation should be compatible with the accepted model, the Grosjean Theory.

2.1 Validation of the P3 Approximation

To validate the P3 Approximation, radiance measurements are used to predict the optical parameters of a tissue phantom with known optical parameters. As well, the results of the P3 Approximation are compared with an established theory of light transport, Grosjean Theory. The tissue phantoms are a mixture of Intralipid-10%™ to mimic scattering effects and methylene blue to control the absorption of the medium. Intralipid-10%™ is a fat emulsion used for intravenous feeding of patients, but is also extensively used by the biomedical optics community to emulate turbid media. The "10%" refers to 10 g of lipids per 100 mL of emulsion, such that a 100 mL sample has 10g soybean oil, 1.2 g lecithin, and 2.2 g glycerine anhydrous.[10] The optical parameters of Intralipid phantoms have been well-studied;

[10]When making a tissue phantom, the quantity of Intralipid™ is referenced in terms of the stock solution. For example, a 100 mL phantom consisting of 6% Intralipid and 0.5% methylene blue and 93.5% distilled water will have 6mL Intralipid-10%™, 0.5 mL methylene blue, and 93.5 mL of distilled water. Hereafter, Intralipid-10%™ will simply be referred to as Intralipid.

their optical parameters can be readily calculated. The scattering coefficient, σ_s, of pure intralipid can be calculated with

$$\sigma_s = (2.54 \times 10^9)\lambda^{-2.4}\,\mathrm{cm}^{-1}, \tag{2.18}$$

where λ is the wavelength of the light in nanometers [van Stavaren et al., 1991]. The scattering effects of distilled water and methylene blue were considered to be negligible at our operating wavelengths. The absorption coefficient was found using

$$\sigma_a = EC \ln 10\,\mathrm{cm}^{-1}. \tag{2.19}$$

The extinction coefficient, E [L mol^{-1} cm^{-1}], was measured spectroscopically at the wavelength in question ($E = 4.17 \times 10^4$ L mol^{-1} cm^{-1} at 630 nm). C [mol L^{-1}] is the concentration of the methylene blue. The absorption effects of the distilled water and the Intralipid are ignored since their absorption coefficients are known to be several orders of magnitude smaller than that of methylene blue at the concentrations used. For all experiments using a phantom, the Intralipid has components identical to those described by van Stavaren et al. [1991].

2.1.1 Plane Wave Geometry.

Radiance was measured using a side-viewing probe (radiance probe). The probe was a flat cleaved 400 μm fibre with a 700 μm right-angle prism mounted on the distal end, which was protected by a thin glass sheath. The outer diameter of the probe, including the sheath, was 1.4 mm. This radiance probe was identical to those described by Ballangrud et al. [1996]. The side-viewing probe was secured in a calibrated rotating stage that allowed 360 degree rotation. Light collected by the radiance probe was detected with a silicon photodiode in an integrating sphere

(United Detector Technologies). Source light at 630 nm from a dye laser (Coherent, 599s) pumped by an argon-ion laser (Spectra Physics, Beamlok 2080) was coupled into a 400 μm source fibre distally terminated with a Gradient Index (GRIN) lens. The fibre was used to circularly illuminate the side of a plastic container that held the tissue phantom. The dimensions of the tissue phantom container were 34.5 cm x 34.0 cm x 33.6 cm, to give an approximate volume of 5 L. The container was painted black, except for the illuminated area, in order to minimize boundary scattering effects. A black mask with a 3.5 cm diameter circular opening was placed on the illuminated face of the plastic container. The 3.5 cm diameter opening was illuminated using a 5 cm circular projection from the GRIN lens. The illumination of the opening using a larger diameter circle ensured the elimination of any edge effects and a uniform light intensity across the face of the opening with a variation of ±2%. The experimental arrangement for plane-wave measurements is illustrated in Figure 2.2.

Light fluence measurements were also taken by replacing the radiance probe with a 3 mm diameter spherical isoprobe (QLT Phototherapeutics). Measurements were taken at increments of 1 mm from the illuminated boundary. The measurements to compare the predictions of the Grosjean Approximation were effected using the same container and phantom. However, 630 nm light from the dye laser was coupled into a spherical isoprobe, which was introduced directly into the tissue phantom. Measurements were taken by altering the distance between the source isoprobe and the detecting isoprobe. Three Intralipid phantoms were prepared to evaluate a wide range of optical parameters but the results for two representative phantoms are illustrated here. Phantom 1 consisted of 3% Intralipid, 0.1% methylene blue (dissolved 1 mg/mL), and 96.9% distilled water. The theoretical optical parameters for phantom 1 are: $\sigma_a = 0.04\ \text{mm}^{-1}$, $\sigma_s = 10.65\ \text{mm}^{-1}$ and $g = 0.74$. Phantom 2 was composed of 5% Intralipid, 0.1% methylene blue (dissolved 1 mg/mL), and 94.9%

Figure 2.2: Equipment arrangement for acquiring radiance measurements.

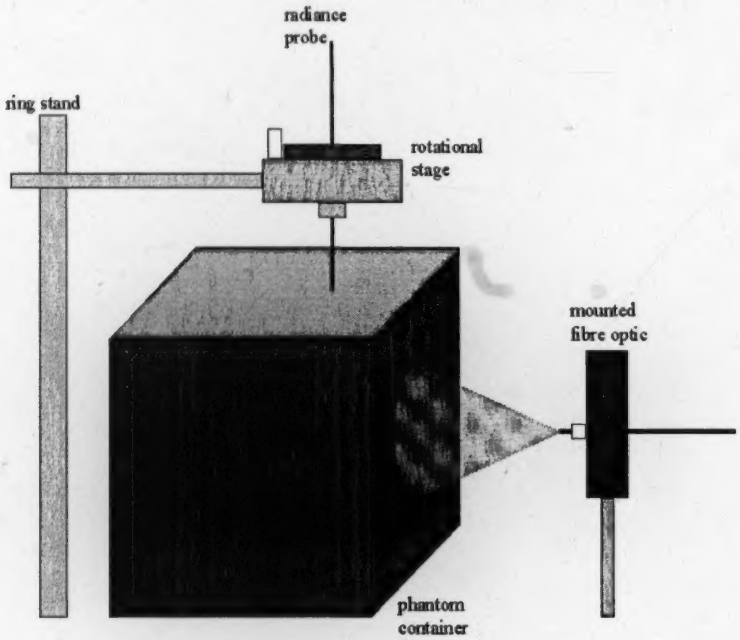

Figure 2.3: Fibre arrangement for acquiring fluence measurements. The detector probe may be replaced with a radiance probe for measurements from an isotropic source.

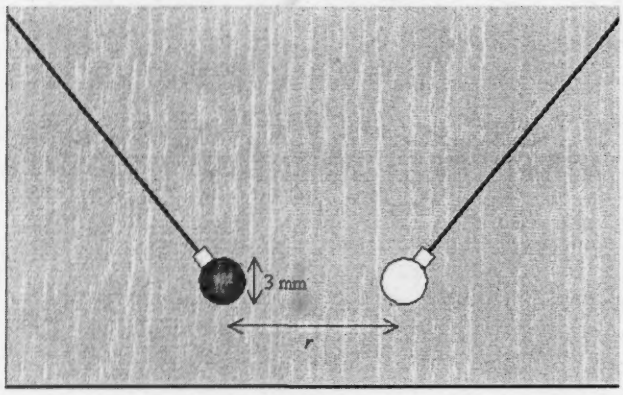

distilled water. The theoretical optical parameters for phantom 1 are: σ_a = 0.044 mm^{-1}, σ_s = 10.08 mm^{-1} and g = 0.69.

Determination of uncertainty in these experiments was difficult because of unpredictable systematic errors. There are many potential sources of error: power meter fluctuation, pump laser drift, laser power fluctuation, technical variation, positioning tolerances, support apparatus flexion, progressive staining of radiance probes/isoprobes, and/or machining tolerances have, at one time or another, affected the accuracy of radiance and fluence measurements. Most of these issues were fortunately surpassable. Experimentally, the largest source of random error was in radial positioning of sources and detectors. The translational stage had a manufacturers tolerance of ±0.02 mm. Since measurements were taken at 1 mm increments, a 2% margin of uncertainty per measurement is implied. Lamentably, a rigorous differential error analysis to the P3 Approximation was not done. Without an accurate determination of the error in laser power, it is not possible to determine absolute error in radiance measurements. Therefore, error is based upon the reproducibility of radiance or fluence measurements. By using a different detector, the 13 PDC 1 (Melles Griot), the real-time variation in the measured light could be determined for this experimental arrangement, which was found to vary by a maximum of 5% of the absolute power measurement. Therefore, an general experimental error of ±5% was assumed for most experiments in this thesis (and the ineffability of possible human error).

2.1.1.1 Results

The optical parameters of the medium are determined by fitting the P3 Approximation to experimental measurements using σ_s, σ_a, and g as variables.[11] The best-fit

[11] In Transport Theory, these parameters are assumed to be independent.

coefficients are the medium's optical parameter. The results obtained by the P3 Approximation varied by less than 5% to theoretical optical parameters of the phantoms. The results from Phantom 1 are illustrated in Figure 2.4 and the results of Phantom 2 illustrated in Figure 2.5. When the optical parameters were introduced into the Grosjean Theory, an accepted model for light propagation, the theoretical fluence calculations correlated favorably with experimental measurements, shown in Figure 2.6.

With confidence that the P3 Approximation can accurately estimate tissue optical parameters in a simple geometry, we may proceed to develop and test the P3 Approximation in the clinically relevant spherical geometry.

2.1.2 Spherical Geometry

A technique similar to that used in the plane wave geometry was used to validate the accuracy of the P3 Approximation with an isotropic point source. Light was produced by an argon-ion pumped Ti:Sapphire laser (both Spectra Physics, Beamlok 2080 and 3900s) operating at λ = 690 nm. This light was coupled into a fibre terminating in a isotropic spherical radiator (QLT Phototherapeutics). Using the same black container, an arrangement similar to that shown in Figure 2.3 was used, replacing the detecting isoprobe with a radiance probe. Radiance and fluence were measured in several tissue phantoms. In this geometry, the predictions of the P3 Approximation may be directly compared to that of Grosjean Theory.

The tissue phantoms were prepared with the same methodology as the phantoms for the plane wave geometry, except that the methylene blue was prepared to be 2 mg/mL. This is because the extinction coefficient for 690 nm light is roughly half that at 630 nm (E = 18448 L mol^{-1} cm^{-1} at 690 nm). Phantom 3 was composed of 6% Intralipid, 0.1% methylene blue (dissolved 2 mg/mL), and 93.9% distilled

Figure 2.4: Comparing the P3 Approximation radiance and fluence against experimental measurements in Phantom 1.

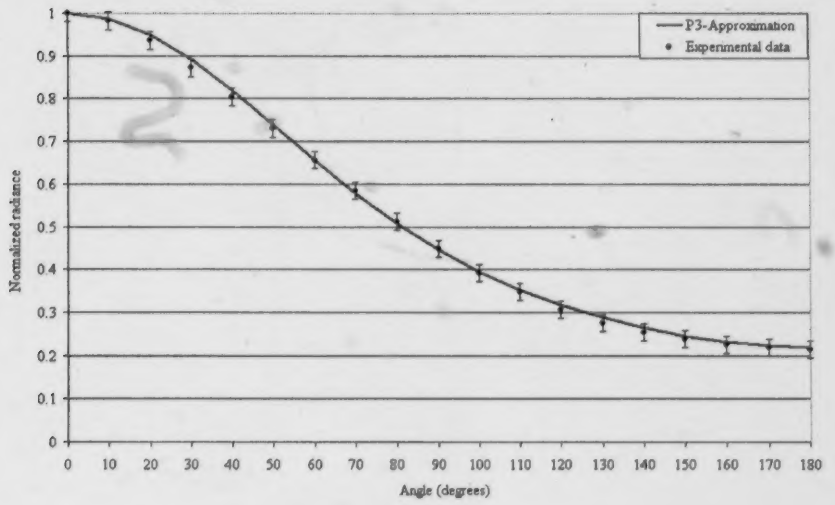

(a) Radiance measurements at 10 mm from the source compared to P3 Approximation in Phantom 1 predicting optical parameters of $\sigma_s = 10.7 \pm 0.1$ mm^{-1}, $\sigma_a = 0.04 \pm 0.005$ mm^{-1}, and $g = 0.76 \pm 0.02$

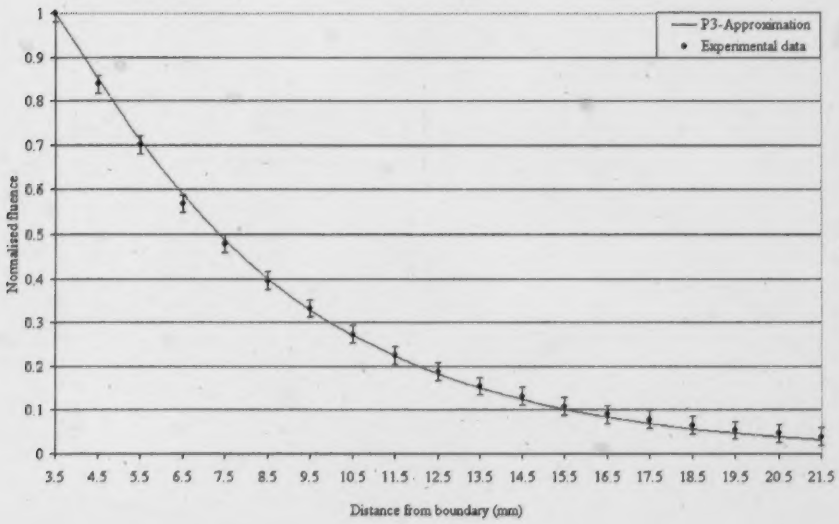

(b) P3 Approximation fluence measurements using the optical parameters supplied in (a).

Figure 2.5: Comparing the P3 Approximation radiance and fluence against experimental measurements in Phantom 2.

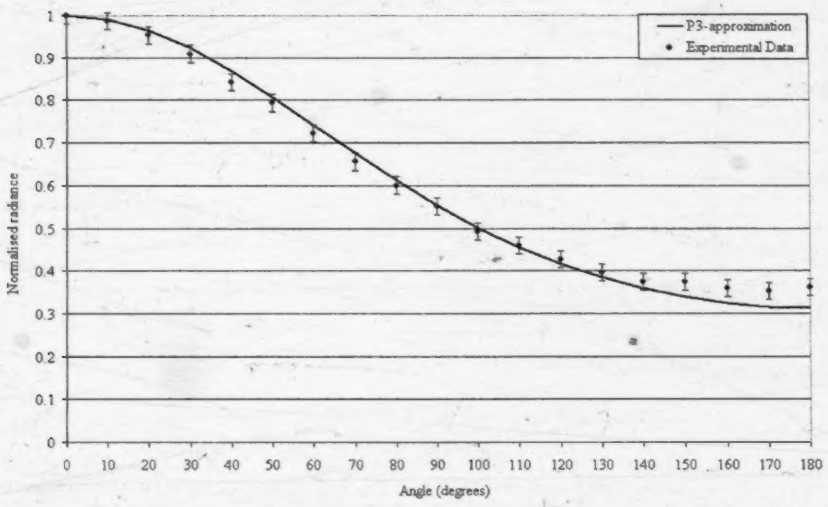

(a) Radiance measurements at 10 mm from the source compared to P3 Approximation in Phantom 2 predicting optical parameters of $\sigma_s = 28.7 \pm 1.0$ mm^{-1}, $\sigma_a = 0.04 \pm 0.005$ mm^{-1}, and $g = 0.77 \pm 0.01$

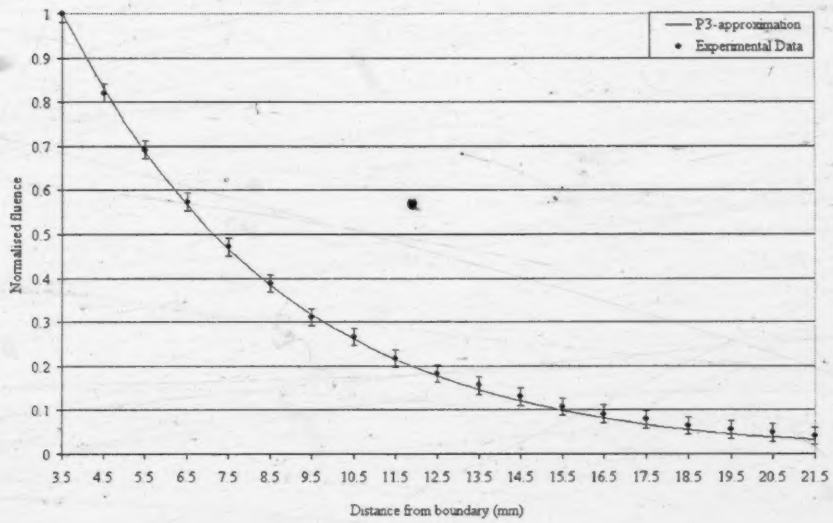

(b) P3 Approximation fluence measurements using the optical parameters supplied in (a)

Figure 2.6: Comparison of the Grosjean Theory (using P3 Approximation generated optical parameters) to experimental fluence measurements.

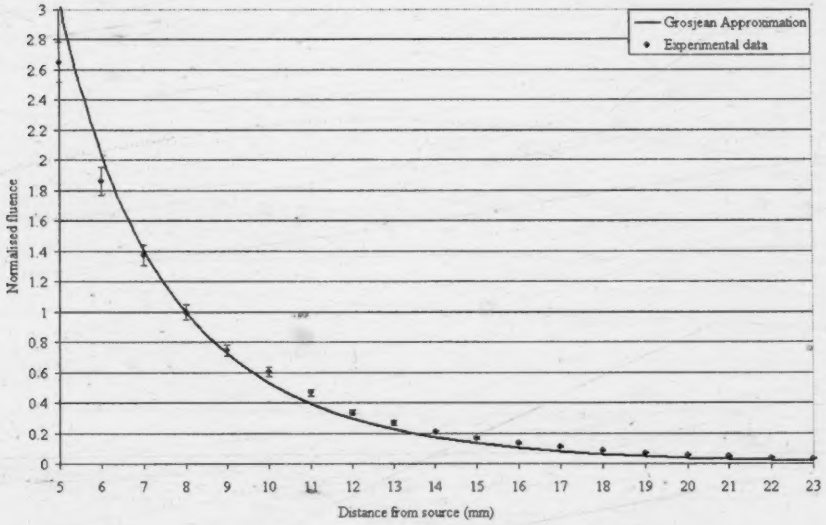

(a) Grosjean Approximation in Phantom 1 using parameters predicted by the P3 Approximation

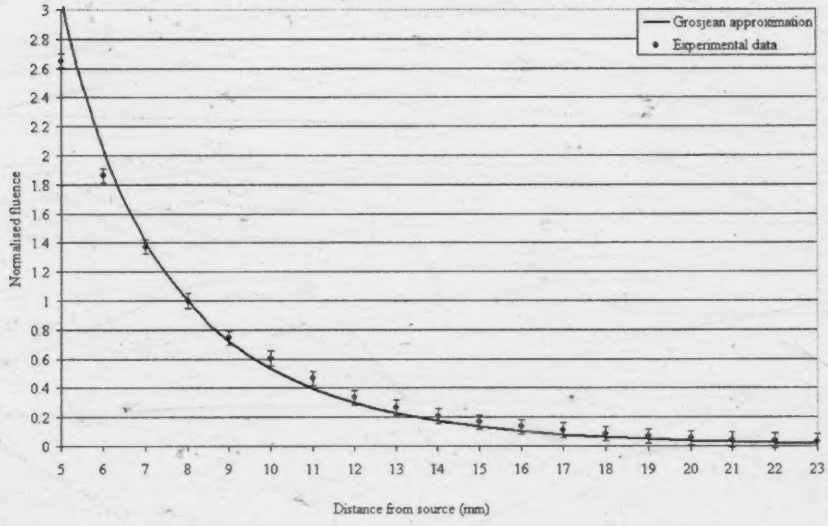

(b) Grosjean Approximation in Phantom 2 using parameters predicted by the P3 Approximation

water, with calculated optical coefficients of σ_s = 22.1 mm^{-1}, σ_a = 0.063 mm^{-1} and g = 0.82. Phantom 4 was composed of 4% Intralipid, 0.1% methylene blue (dissolved 2 mg/mL), and 95.9% distilled water, with calculated optical coefficients of σ_s = 12.1 mm^{-1}, σ_a = 0.063 mm^{-1} and g = 0.82. The optical coefficients were calculated by using Eq(2.18) and Eq(2.19).

2.1.2.1 Results

Radiance and fluence measurements were taken in several optical phantoms with a wide range of optical parameters, but once again, only the results of 2 representative phantoms are given. Figure 2.7a shows the radiance measurements made in an Phantom 3. These measurement were fitted to the P3 Approximation giving the optical parameters $\sigma_s = 22.0 \pm 1.0$ mm^{-1}, $\sigma_a = 0.07 \pm 0.005$ mm^{-1} and $g = 0.88 \pm 0.01$. The characteristics of this phantom, are very close to those calculated: σ_s = 22.1 mm^{-1}, σ_a = 0.063 mm^{-1} and g = 0.82. Figure 2.7b shows the fluence, measured in this Intralipid solution, compared with predictions made using both the P3 Approximation and Grosjean Theory.

The P3 Approximation measured optical parameters of the phantoms were calculated to be theoretical predictions of phantom shown in Figure 2.8a were made using$\sigma_s = 12 \pm 1.0$ mm^{-1}, $\sigma_a = 0.07 \pm 0.005$ mm^{-1} and $g = 0.86 \pm 0.01$, which were once again close to the calculated parameters of σ_s = 12.1 mm^{-1}, σ_a = 0.063 mm^{-1} and g = 0.86.

2.2 Implications

Radiance measured at a single point in tissue illuminated by an optical point source was compared with radiance predicted by the P3 Approximation in order to esti-

Figure 2.7: Experimental radiance and fluence measurements from an isotropic source compared to the predictions of the P3 Approximation in Phantom 3.

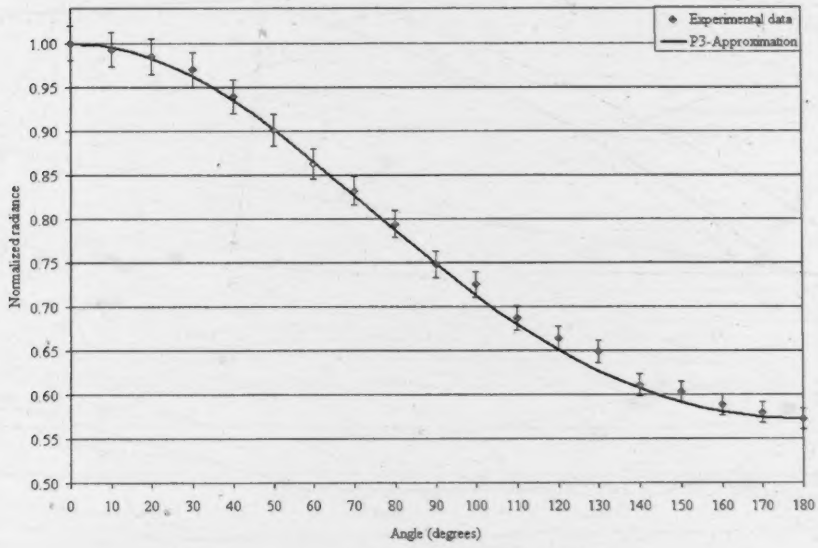

(a) The P3 Approximation fit to experimental radiance measurements to estimate phantom optical parameters: $\sigma_a = 0.07 \pm 0.005$ mm^{-1}, $\sigma_s = 22.0 \pm 1.0$ mm^{-1} and $g = 0.88 \pm 0.01$.

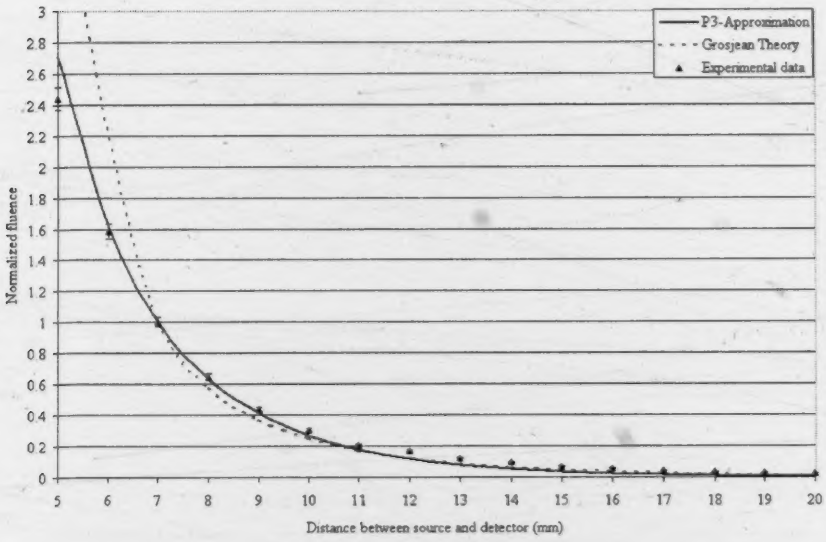

(b) Using optical parameters predicted in (a), experimental fluence measurements are compared to the predictions of the P3 Approximation and Grosjean Theory.

Figure 2.8: Experimental radiance and fluence measurements from an isotropic source compared to the predictions of the P3 Approximation in a tissue Phantom 4.

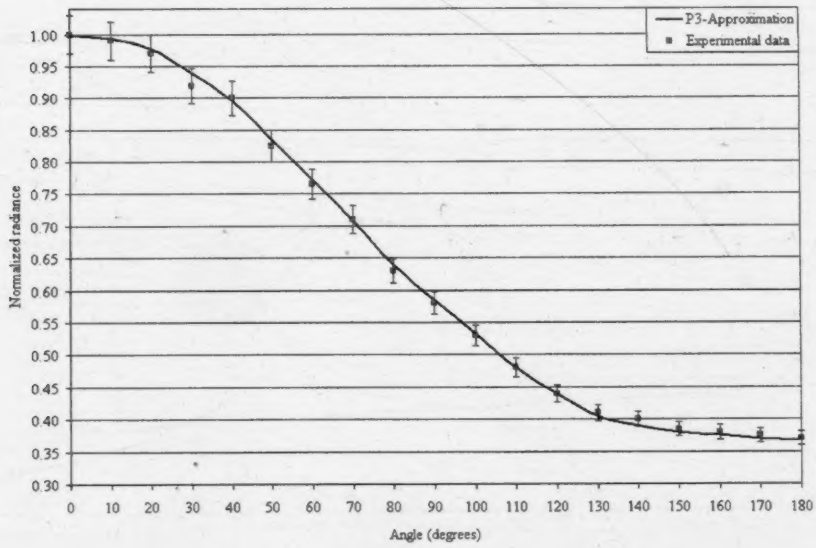

(a) The P3 Approximation fit to experimental radiance measurements predicting phantom optical parameters: $\sigma_a = 0.07 \pm 0.005$ mm^{-1}, $\sigma_s = 12.0 \pm 1.0$ mm^{-1} and $g = 0.86 \pm 0.01$.

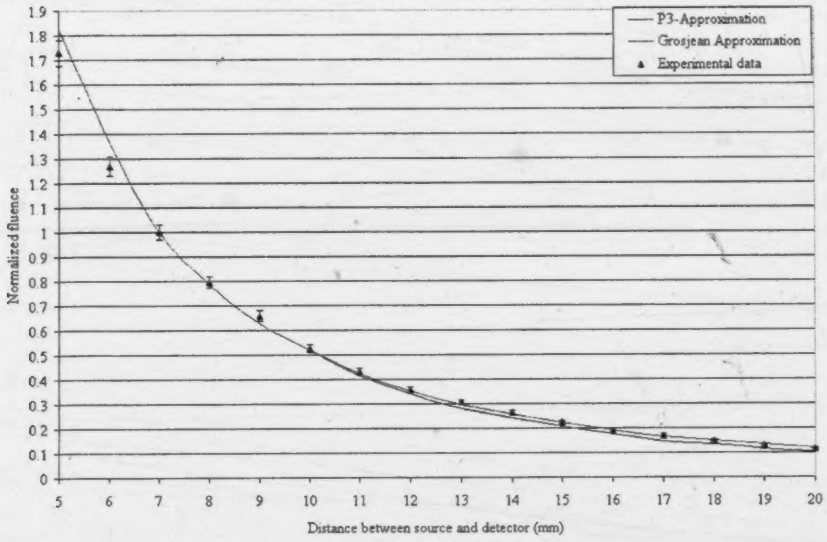

(b) Using optical parameters predicted above, measured fluence is compared against the predictions of the P3 Approximation and the Grosjean Theory

mate the optical parameters of tissue between the monitoring point and the source. The optical parameters generated by the P3 Approximation were extremely close to the known optical characteristics for Intralipid phantoms. Experimental fluence measurements compared favorably against those calculated using the P3 Approximation and the Grosjean Theory. Grosjean Theory was derived independently from the P3 Approximation, yet the optical parameters predicted by the P3 Approximation furnish accurate results when inserted into the Grosjean Approximation. This correlation between the two theories provides additional confidence in the accuracy and reproducibility of the P3 Approximation.

These experiments show that the P3 Approximation has the potential to be an indispensable tool for interstitial PDT: The P3 Approximation is minimally invasive, single point reference for all necessary data; calculations are performed quickly; and, it is accurate. Armed with the optical parameters for the target, it is now possible to deliver a predictable amount of light to the target volume, and minimize potential damage to surrounding tissues. At the very least, the penetration depth, Eq(2.2), in tissue can be calculated, and we can begin to consider the therapeutic potential of PDT.

Chapter 3

Predicting Fluence from Cylindrical Diffusing Fibreoptics: Huygens-Diffusion Theory

Older photosensitizers, such as Photofrin®, have strong absorption peaks near 630 nm where transmissivity in human tissue (including human prostate) is relatively poor [Boyle and Dolphin, 1996]. Even though the human prostate is only 35 to 60 cc in volume, adequate light coverage with 630 nm radiation would require multiple fibre implants. Newer and more potent photosensitizers such as BPD-MA have absorption peaks at longer wavelengths (690 nm) [Richter et al., 1991]. At these longer wavelengths, tissue transmissivity is greater, but with the δ = 8 mm at 690 nm in prostate tissue, multiple implanted sources are still necessary for uniform irradiation of the gland. With increased tissue transmissivity, one must exercise additional care that peripheral organs do not receive a phototoxic light dose. PCa is a multifocal disease, necessitating uniform light distribution for the entire organ. Most PCa (80%) occurs on the posterior lateral margin of the gland; therefore, our

particular therapeutic goal is to target this area, which is juxtaposed against the anterior side of the rectum. Collateral damage to the rectum is therefore a potential serious complication in effectively treating PCa. Other adjacent tissues, such as the urethral sphincter, neurovascular bundle to the penis and bladder neck, are also at risk.

The modeling of tissue light dosimetry therefore requires a detailed knowledge of the optical parameters of the tissue treatment volume. Available methods for estimating tissue optical parameters have, in the past, had very limited clinical utility either because they were too time consuming or too invasive, but the clinically promising combination of tissue radiance measurements and the P3 Approximation can be used to determine tissue optical parameters [Dickey et al., 2001]. Currently there are no accurate models to predict tissue light fluence from an interstitial cylindrical source, especially near the source. A model to predict light fluence from one cylindrical source should readily extend to predict that light from an array of sources simply by summing the fields from the individual sources. This chapter describes a unique, analytical model that accurately predicts light fields from cylindrical diffusing sources—the most common fibreoptic source used to deliver light for PDT.

3.0.1 Light Dosimetry for Interstitial PDT Using Diffusion Theory

Diffusion theory is an accepted and tested method of predicting light fluence in PDT. Diffusion theory does have one key limitation—it is only accurate as long as the scattering dominates absorption, i.e. $\frac{\sigma_s}{\sigma_t} > 0.99$, or in other words, the medium is assumed to scatter isotropically. If the albedo requirements for the target are met, Diffusion theory is preferable to using the P3 Approximation. Most human tissues,

including prostate are fortunately part of this regime. The biggest advantage of Diffusion Theory is that analytical solutions are available in a number of simple geometries; although, several approximations have been traditionally imposed to simplify calculations. With a modest amount of computer power (e.g. PentiumII™ class processor or greater), a complete analytical solution can quickly and accurately be calculated. In this chapter, a Diffusion model to predict the fluence from a cylindrical source is explained. This model is capable of calculating the fluence near the boundaries, where most derivations using Diffusion Theory are inaccurate due to assumptions made to simplify calculations.

3.0.1.1 The Huygens Radiator and Formulation of the Fluence for Huygens-Diffusion Theory

Mathematical modeling of light emitted by a cylindrical source in tissue has, to date, not met with much success. A diffuse cylindrical light source is somewhat difficult to characterize in cylindrical coordinates because the emission of the light is not exclusively normal to the face of the source, making a solution in a cylindrical geometry difficult to obtain. Christiaan Huygens was the first to propose that a wave front from a finite source (such as a single slit) may be decomposed into an array of idealized infinitesimally small point sources [Hecht, 1990]. He demonstrated that the emission from this array could be determined at any point in space by integrating the effects of these point sources. In principle, if an accurate mathematical representation can be given to the fluence distribution of an ideal point source—a Huygens radiator—Huygens' theory can be implemented in conjunction with Diffusion theory to predict the light field from any linearly continuous source.

Using Grosjean Theory as a light propagation model, early investigators decomposed a cylindrical diffuse light source into an array of finite point sources, but this

method met with limited success [Arnfield et al., 1989]. Grosjean Theory tends to not accurately predict fluence near the sources, with approximately a 15% discrepancy between theory and experimental measurements at distances closer than 5mm to the diffuser. Using Diffusion Theory in a cylindrical geometry, Star modeled the cylindrical source as an finite array of infinitesimal point sources, but in the cylindrical geometry he proposed, an analytical solution required a number of approximations in addition to those approximations already established by Diffusion Theory [Star, 1997]. Unfortunately, Star's derivation was never compared with experimental data. It should be noted that Star's work was pivotal in the forthcoming derivation and readers are referred to his work for a comprehensive description of Diffusion Theory in various simple geometries [Star, 1997].

Since a Huygens' radiator is an array of infinitesimal point sources, one begins with the examination of the diffusion of a point source. The fluence from a cylindrical source is predicted by integrating the fluence from each elemental source, in spherical coordinates, over the space occupied by the cylindrical diffuser. Assuming an isotropic point source (with azimuthal and polar symmetry), the diffusion equations have only radial dependence: a complete, analytical solution is possible in this geometry. Figure 3.1 shows the geometry of the isotropic point source with appropriate boundaries.

The Diffusion Equations pertinent to this geometry are:

$$\frac{1}{r^2}\frac{\partial}{\partial r}r^2[F_{r+}(r) - F_{r-}(r)] = -2\sigma_a[F_{r+}(r) + F_{r-}(r)] + \sigma_s S(r) \qquad (3.1)$$

and

$$\frac{\partial}{\partial r}[F_{r+}(r) + F_{r-}(r)] = -\frac{3}{2}\sigma_{tr}[F_{r+}(r) - F_{r-}(r)] + \frac{3}{2}g\sigma_s S(r), \qquad (3.2)$$

Figure 3.1: Geometry of an isotropic point source. The physical size source is modeled with ρ, with the point source theoretically located at the origin, i.e.$r = \rho = 0$.

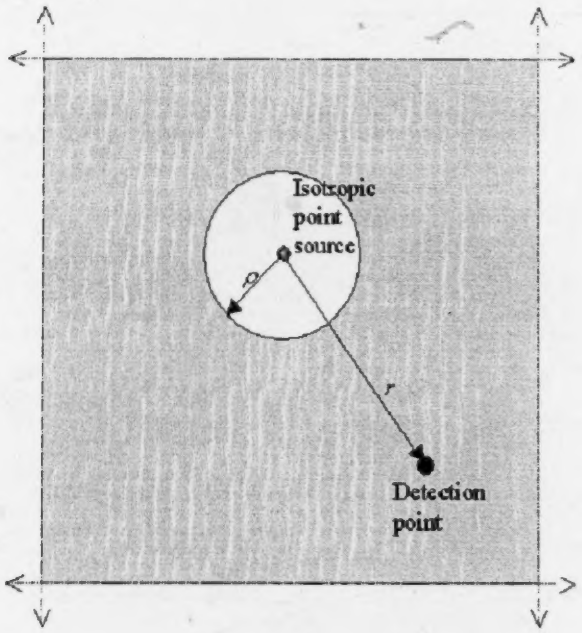

where

$$S(r) = \frac{P_0}{4\pi r^2} e^{-\sigma_t(r-\rho)}. \tag{3.3}$$

$F_{r+}(r)$ and $F_{r-}(r)$ – the forward and backward flux vectors, respectively [Welch and van Gemert, 1995];[1]

$S(r)$ – the source function representing the non-scattered, unabsorbed fluence; and

P_0 – the initial power of the source.

Ultimately, we wish to find the fluence, which is related back to the flux vectors by

$$\phi(r) = 2[F_{r+}(r) + F_{r-}(r)] + S(r) \tag{3.4}$$

To solve Eq(2.16) and Eq(3.2), one multiplies both diffusion equations by r^2 and then substitutes the isolated $[F_{r+}(r) - F_{r-}(r)]$ from Eq(3.2) into Eq(2.16). By using the identity,

$$\frac{\partial}{\partial r}[r^2 \frac{\partial}{\partial r} f(r)] = r \frac{\partial^2}{\partial r^2} r f(r),$$

one obtains the differential equation,

$$\frac{\partial^2}{\partial r^2}\{r[F_{r+}(r) + F_{r-}(r)]\} - \sigma_{eff}^2 r[F_{r+}(r) + F_{r-}(r)] = W\frac{e^{-\sigma_t(r-\rho)}}{r}, \tag{3.5}$$

where σ_{eff} is the effective transport coefficient, related to the previously defined optical coefficients by $\sigma_{eff} = \sqrt{3\sigma_a\sigma_{tr}}$, and W is a combination of constants, defined by

$$W = -\frac{3}{8\pi}\sigma_s P_0[g\sigma_t + \sigma_{tr}]. \tag{3.6}$$

This differential equation (like all differential equations) has a homogeneous solu-

[1] In an isotropic medium, an assumption for the validation of Diffusion Theory, $F_{r+}(r)$=$F_{r-}(r)$. That is to say, the outward flux at point in space will equal the inward flux.

tion and a particular solution such that

$$[F_{r+}(r) + F_{r-}(r)]_{total} = [F_{r+}(r) + F_{r-}(r)]_{homogeneous} + [F_{r+}(r) + F_{r-}(r)]_{particular}. \quad (3.7)$$

Since $F_{r+}(r)$ and $F_{r-}(r)$ are functions dependent only upon the radius, Eq(3.5) decomposes into a second order ordinary differential equation. To obtain the particular solution, in Eq(3.5) $Q(r)$ is substituted for $r[F_{r+}(r) + F_{r-}(r)]$ and Eq(3.5) is rewritten as

$$\frac{d^2}{dr^2}Q(r) - \sigma_{eff}^2 Q(r) = W\frac{e^{-\sigma_t(r-\rho)}}{r}. \quad (3.8)$$

The solution to Eq(3.8) can be found using Mathematica™;

$$[F_{r+}(r) + F_{r-}(r)]_{particular} = [\frac{W}{2\pi r}\int_r^{r_0}(e^{\sigma r}e^{-\sigma_{eff}x} - e^{-\sigma_{eff}r}e^{\sigma_{eff}x})\frac{e^{-\sigma_t(x-\rho)}}{x}dx].$$

Similarly, the homogeneous differential equation is

$$\frac{d^2}{dr^2}Q(r) - \sigma_{eff}^2 Q(r) = 0 \quad (3.9)$$

This elementary differential equation is easily soluble by finding the characteristic roots of the indicial equation, giving the the solution

$$[F_{r+}(r) + F_{r-}(r)]_{homogeneous} = A_1\frac{1}{r}e^{-\sigma_{eff}(r-\rho)} + A_2\frac{1}{r}e^{\sigma_{eff}(r-\rho)}$$

Substituting the homogeneous and particular solutions of Eq(3.5) into Eq(3.7) , one obtains the solution for the fluxes in the following form:

$$\begin{aligned}[F_{r+}(r) + F_{r-}(r)]_{total} &= [A_1\tfrac{1}{r}e^{-\sigma_{eff}(r-\rho)} + A_2\tfrac{1}{r}e^{\sigma_{eff}(r-\rho)}] \\ &+[\tfrac{W}{2\pi r}\textstyle\int_r^{r_0}(e^{\sigma r}e^{-\sigma_{eff}x} - e^{-\sigma_{eff}r}e^{\sigma_{eff}x})\tfrac{e^{-\sigma_t(x-\rho)}}{x}dx],\end{aligned} \quad (3.10)$$

where the first term on the right hand side of Eq(3.10) is the homogeneous solution, and the second term is the particular solution. A_1 and A_2 are integration constants to be determined from the boundary conditions. The integration constant, r_0, is set to ∞, since our solution is valid for all $r > \rho$. Eq(3.10) becomes:

$$[F_{r+}(r) + F_{r-}(r)]_{total} = [A_1 \tfrac{1}{r} e^{-\sigma_{eff}(r-\rho)} + A_2 \tfrac{1}{r} e^{\sigma_{eff}(r-\rho)}] +$$
$$[\tfrac{W}{2\pi r}(e^{\sigma_{eff} r} E_1[(\sigma_{eff} + \sigma_t)r] - e^{-\sigma_{eff} r} E_1[(\sigma_t - \sigma_{eff})r])$$

$E_1[(\sigma_{eff}+\sigma_t)r]$ is the exponential integral—a commonly used mathematical tool occurring commonly in problems involving gases with a Maxwell-Boltzmann energy distribution. It is simply defined by

$$E_1(x) = \int_x^\infty \frac{e^{-t}}{t} dt.$$

Recent mathematical programs (including v3.2 GNU C) have the exponential integral as a built-in function.

Using Eq(3.4), the solution for the fluence therefore becomes

$$\begin{aligned} \phi(r) &= 2[A_1 \frac{1}{r} e^{-\sigma_{eff}(r-\rho)} + A_2 \frac{1}{r} e^{\sigma_{eff}(r-\rho)}] + \\ &\quad [\frac{W}{\pi r}(e^{\sigma_{eff} r} E_1[(\sigma_{eff} + \sigma_t)r] - e^{-\sigma_{eff} r} E_1[(\sigma_t - \sigma_{eff})r]) + \\ &\quad \frac{P_0}{4\pi r^2} e^{-\sigma_t(r-\rho)}. \end{aligned} \tag{3.11}$$

The final step is to determine the constants A_1 and A_2. For this step, the following boundary conditions are evoked:

$$\phi(\infty) = 0; \tag{3.12}$$

$$F_{r+}(\rho) = F_{r-}(\rho). \tag{3.13}$$

Figure 3.2: Cylindrical source, modeled with an array of infinitesimal point sources aligned on the middle of the diffuser

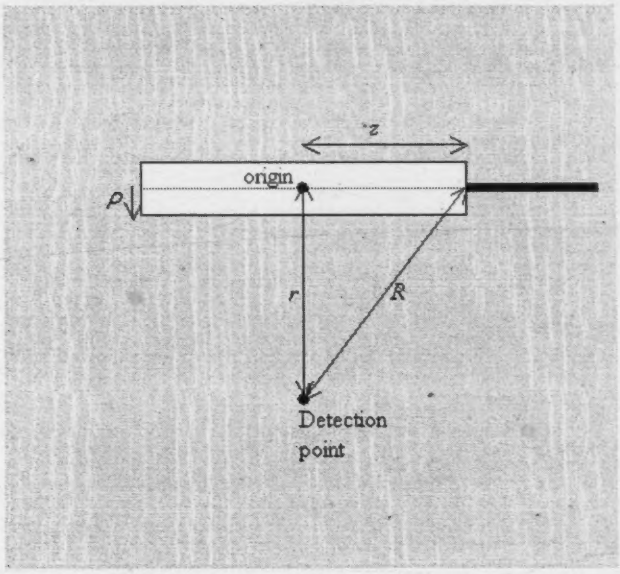

Imposing Eq(3.12) for a bounded solution forces $A_2 = 0$. Using the implications of Eq(3.13) in Eq(3.2), one can readily calculate the integration constant A_1.

The solution for A_1 is substituted back into Eq(3.11) to obtain the final expression for the fluence of a point source:

$$\begin{aligned}\phi(r) &= 2\left(\frac{\sqrt{3}P_0(g\sigma_a+\sigma_t)e^{\sigma_t\rho}}{8\pi\sqrt{\sigma_a(\sigma_t-g\sigma_s)}}\right)\frac{1}{r}e^{-\sigma_{eff}r}+\\ &\frac{We^{-\sigma_t\rho}}{\pi r}[E_1[(\sigma_{eff}+\sigma_t)r]-e^{-\sigma_{eff}r}E_1[(\sigma_t-\sigma_{eff})r] \qquad (3.14)\\ &+\frac{P_0}{4\pi r^2}e^{-\sigma_t(r-\rho)}.\end{aligned}$$

To obtain an expression for the fluence for a Huygens' Source, the final solution, Eq(3.14), is integrated over the length of the cylindrical diffusing tip to give the fluence at any point in space.

Using the information given in Figure 3.2, the fluence at the detection point is given

by the following integral:

$$\phi_{cyl}(r) = 2\int_{r}^{R} \phi_{pntsrc}(t)dt = 2\int_{0}^{z} \phi_{pntsrc}(\sqrt{r^2 + t^2})dt. \qquad (3.15)$$

The solution represented by Eq(3.15) represents a solution where the detector bisects the cylindrical diffuser; however, solutions exist for any placement of the detector with respect to the cylindrical diffuser, only the limits of integration need to be adjusted.[2] The final solution is obtained by numerically integrating Eq(3.15) over the length of the diffuser. The contribution of light from various Huygens' sources should sum linearly. Thus, the fluence at an arbitrary point from an array of cylindrical sources should be a simple summation of individual sources.

$$\phi_{array}(r_i) = 2[\int_{r_1}^{R_1} \phi_{pntsrc1}(x_1)dx_1 + \int_{r_2}^{R_2} \phi_{pntsrc2}(x_2)dx_2 + ...]. \qquad (3.16)$$

The Mathematica™ formulation of the derivation of Huygens-Diffusion Theory is detailed in Appendix 2.

3.1 Validation of Huygens-Diffusion Formulation

Experimental phantoms used were identical to those used to confirm the accuracy of the P3 Approximation, created by mixing Intralipid-10%™ (Kabi-Pharmacia) for scattering effects, methylene blue for absorbing effects (dissolved in distilled water, 2mg/mL) and distilled water. The optical parameters for the Intralipid media determined using the P3 Approximation were confirmed using Eq(2.18) to calculate σ_s and Eq(2.19) to calculate σ_a [van Stavaren et al., 1991]. At 690 nm, an extinction coefficient of $E = 1.84 \times 10^4$ L mol^{-1} cm^{-1} was used. The P3 Approximation estimates varied by 2.8% from the theoretically calculated values of σ_s and σ_a. An

[2]This is illustrated experimentally in §3.1, Figure 3.3.

anisotropy factor of $g = 0.88$, as predicted by the P3 Approximation, was used in our theoretical calculations.

Fluence was measured using an isoprobe. Light collected by the isoprobe was collected by a silicon photodiode in an integrating sphere (Melles Griot - 13 ISP 003), and quantified by a general purpose light detector (Melles Griot, 13 PDC 001). Source light from an argon-ion pumped Ti:Sapphire laser (both Spectra Physics, Beamlok 3600, 2900s, respectively), operating at 690 nm, was coupled into a 400 μm source fibre terminated by a 1.5 cm long cylindrical diffusing tip with a diameter of 1.5 mm (QLT Phototherapeutics). Values of of $z = 7.5$ mm and $\rho = 0.75$ mm were therefore used to calculate the fluence from this source. However, for the results in Figure 3.3, the value of z was variable, and r remained constant. The emission along the length of the cylindrical diffusing tip varied less than 5%. This was measured by running a flat-cleaved fibreoptic perpendicular to the face of the diffuser. All cylindrical sources used match these specifications.

Experiments were performed in several phantoms to simulate a wide range of optical parameters ($6\ \text{mm}^{-1} < \sigma_s < 26\ \text{mm}^{-1}$ and $0.01\ \text{mm}^{-1} < \sigma_a < 0.09\ \text{mm}^{-1}$), maintaining a ratio of $\frac{\sigma_a}{\sigma_t} > 0.99$ in order to ensure the validity of the Diffusion approximation. The results shown are based on the same tissue phantom used in the validation of the P3 Approximation in spherical coordinates: 6% Intralipid, 0.1% methylene blue and 93.9% distilled water solution, with optical parameters of $\sigma_s = 22\ \text{mm}^{-1}$, $\sigma_a = 0.07\ \text{mm}^{-1}$ and $g = 0.88$. This phantom was chosen because it is a good representation of the optical parameters for tissues such as prostate, breast and cartilage [Welch and van Gemert, 1995]. Measurement were taken at 1 mm intervals, with the direction depending upon the geometry of the experiment. Some change in the relative positioning of the source and the isoprobe was observed with the addition of Intralipid to the 5L container, but exercising care and slowly adding the phantom to the container minimized displacement. An error of ±5% is assumed for

all the fluence measurements. The optical parameters of the medium found using the P3 Approximation are within ±2.5% of the theoretical optical parameters of the phantom calculated using Eq(2.18) and Eq(2.19). Excellent agreement between experimental and theoretical data was observed in every experiment.

As illustrated in Figure 3.3a, fluence is measured parallel to the length of the diffuser, at a distance of 10mm from the source. The measured fluence is compared with Huygens-Diffusion theory.

Illustrated in Figure 3.4, fluence from a single cylindrical source was measured in three different media with unique transport qualities: dry field dilution (no absorption and no scattering), a phantom displaying primarily scattering characteristics (composed of 6% Intralipid and 94% water), and a phantom with both scattering and absorbing characteristics (6% Intralipid, 0.1% methylene blue (dissolved 2mg/mL) and 93.9% distilled water). Dry field dilution measurements are first recorded with the cylindrical diffuser placed in the center of a 5L container and measurements at 1 mm increments were taken along the measurement path, as shown in Figure 3.4a. The scattering media was then added to the phantom without changing the position of the source within the container or the power of the light emitted, and the measurements were repeated. The scattering media was removed and then replaced with the scattering/absorbing media before the final set of measurements were recorded.

Fluence from arrays of three 1.5 cm cylindrical sources was also measured. Figure (3.5) and Figure (3.6) each show a different set of experimental fluence data from three sources compared to the Huygens fluence model. In both sets of data, the positions of the cylindrical sources are maintained in an equilateral triangle, with the length of the diffusers going into the plane of the page. The detecting isoprobe bisects the diffusers, as illustrated in Figure 3.4a.

A comparison of experimental fluence measurements and theoretical predictions for

Figure 3.3: Comparing the lateral diffusion measurements to those predicted by Huygens-Diffusion Theory radiator.

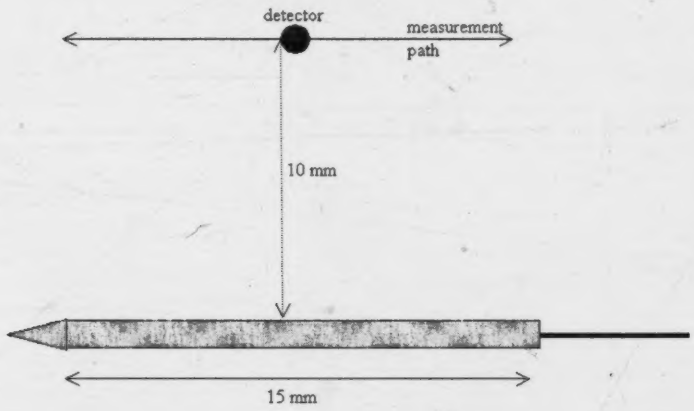

(a) The experimental geometry of the source and detector for the data in (b).

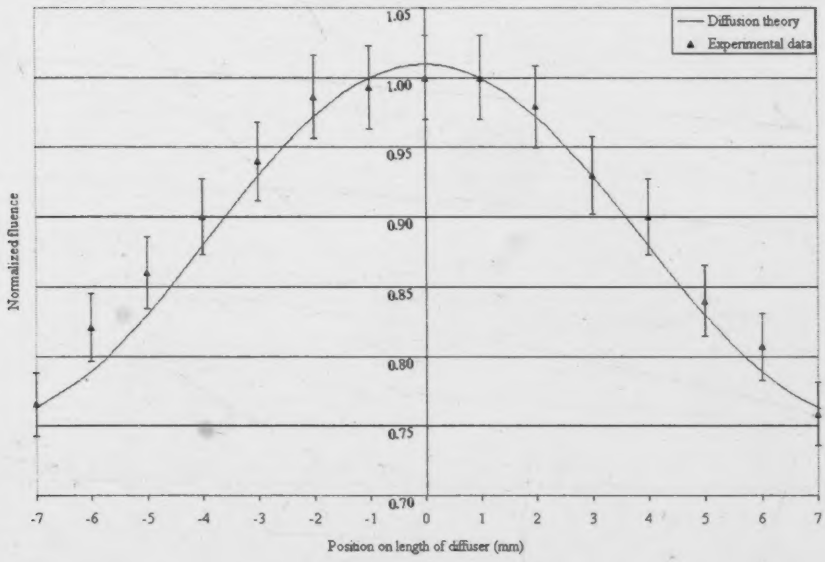

(b) The predictions of Diffusion Theory compared to experimental measurements.

Figure 3.4: Fluence measurements in various phantom media as compared with the theoretical values predicted by the Huygens-Diffusion fluence model. The dry field measurements were made in air. The low absorption phantom had optical parameters of σ_s = 22 mm^{-1}, σ_a = 0.001 mm^{-1} and g = 0.81while the absorbing/scattering phantom had optical parameters of σ_s = 22 mm^{-1}, σ_a = 0.07 mm^{-1} and g = 0.81.

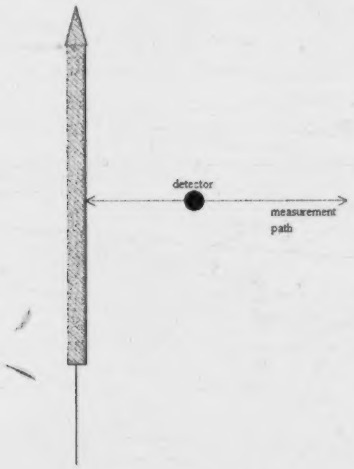

(a) Experimental arrangement for data shown in (b)

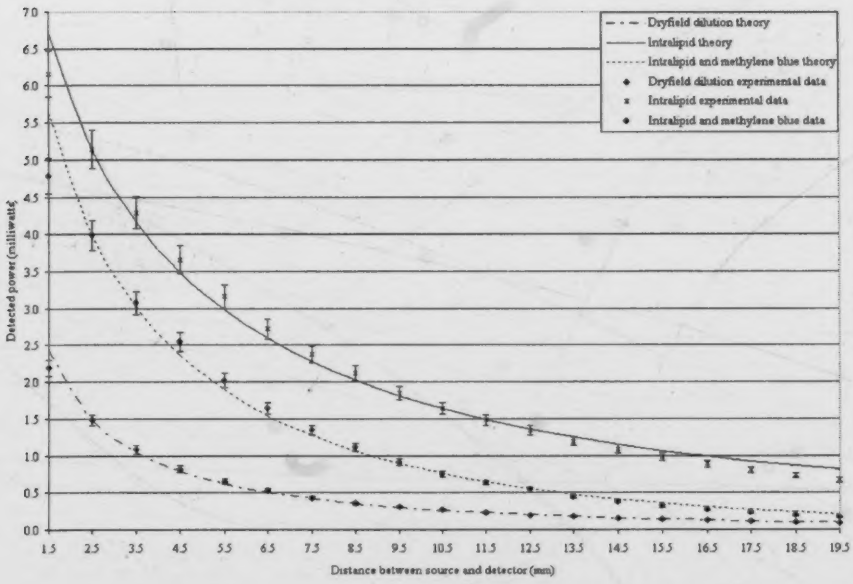

(b) Experimental fluence measurements compared to theory

the three fibre array, including the fibre arrangement, is shown in Figure 3.5. All source outputs were measured)to be $75 \pm 5 \frac{W}{cm}$ mW/cm (i.e. $P_0 = P_A = P_B = P_c = 0.075 \frac{W}{cm}$) using an integrating sphere and universal power detector (Melles Griot, 13 ISP 003 and 13 PDC 001, respectively).

In the configuration illustrated in Figure 3.6, fluence measurements for the three source fibres were compared to the the predictions of Diffusion Theory. The output of the sources were measured to be $P_A = 75 \pm 10 \frac{mW}{cm}$ ($P_0 = 75 \pm 10 \frac{mW}{cm}$), $P_B = P_C = 102 \pm 15 \frac{mW}{cm}$ ($P_0 = 102 \pm 15 \frac{mW}{cm}$). Sources were set to different powers to examine the ability of this derivation to predict the effects of differing input conditions. The high uncertainty in the laser power is caused from the splitting the light from the Ti:Sapphire laser into 3 beams, and coupling it into the cylindrical diffusers using objective lenses. In order to have equal fibre output powers, the coupling of the split beam was adjusted. When the fibre was moved, the slight coupling inefficiency caused fluctuations in the output power. When secured, the fluctuations were minimized. Therefore, the largest source of error was, ironically, attempting to measure the power.

3.2 Implications

Figure 3.4 illustrates and quantifies how increased scattering in the media increases localized fluence. Due to approximations made to simplify Diffusion Theory calculations or due to the arbitrary units used to quantify photon energy, most fluence measurements and calculations are normalized. The measured and theoretical fluence values from a cylindrical source shown in Figure 3.4 are not normalized. This fluence model will not only accurately predict the fluence distribution but will also predict the absolute fluence and the changes associated with changes to the scattering and absorbing properties of the medium.

Figure 3.5: Experimental fluence produced by an array of cylindrical diffusers compared to the predictions of Huygens-Diffusion Theory.

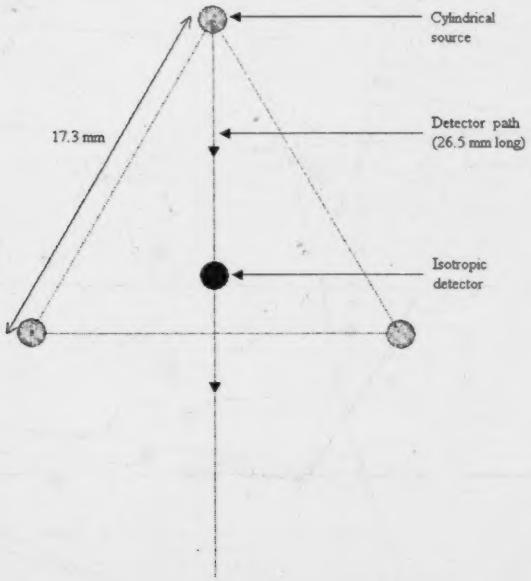

(a) Geometry of diffusers used for data shown in (b)

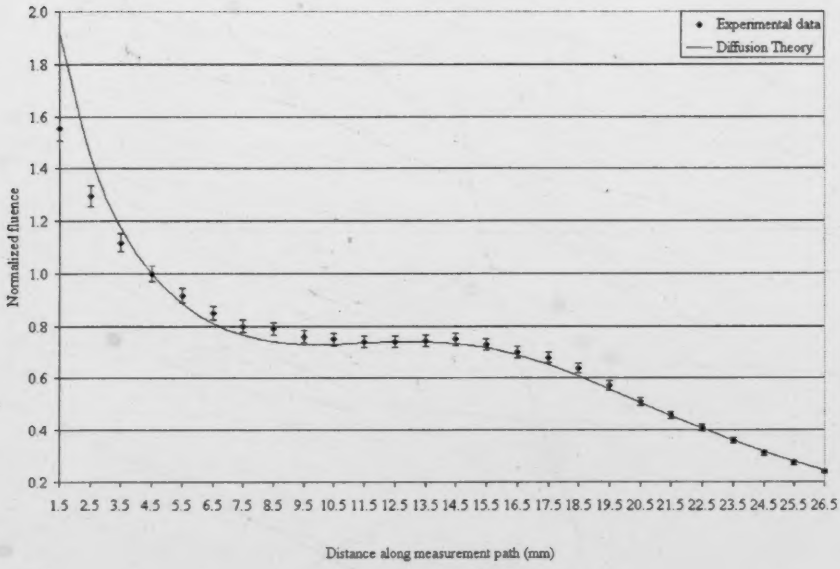

(b) Comparison of experimental measurments to the predictions of Diffusion Theory.

Figure 3.6: Fluence predictions from an array of 3 cylindrical diffusers compared to Huygens-Diffusion Theory .

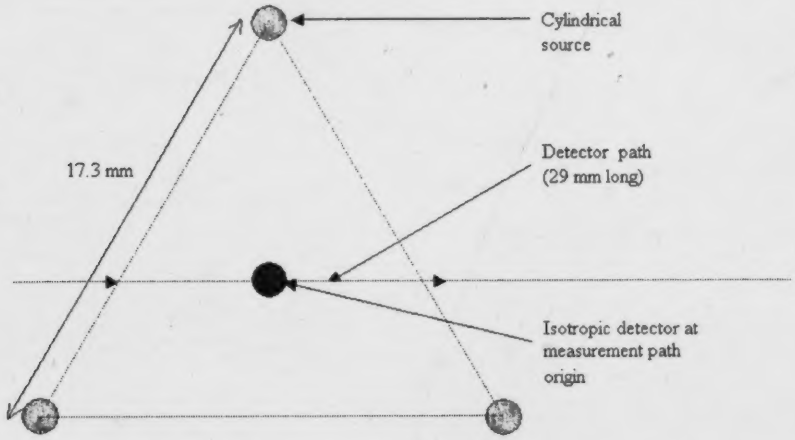

(a) Geometry of diffusers used for data shown in (b)

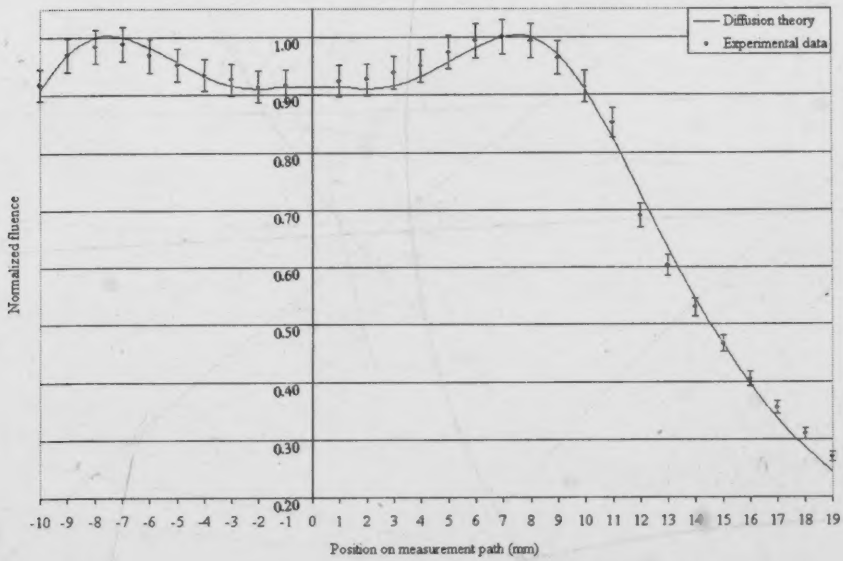

(b) Comparison of experimental measurments to the predictions of Diffusion Theory.

The combination of the P3 Approximation and a Huygens' Radiator provide a complete model to predictably deliver light to an interstitial tumour mass. The method is general and the array of three cylindrical interstitial sources could be replaced with other sources of arbitrary shape and size, as long as the shape could be defined for purpose of integration (or spatially defined for numerical integration). Fluence measurements are typically within ±1.5% of theoretical values predicted using the Huygens-Diffusion Theory model. Note that the fluence is predicted reasonably well near the boundaries, but the largest discrepancies between theory and experiment still occurred near the source. A disagreement larger than 5% is observed in the first few data points illustrated in Figure 3.5b. This error is most likely induced by the physical diameter of the detecting isoprobe. Measurements closer than 1.5 mm were not possible because of the physical diameter of the detector fibre. In fact, 1.5 mm is the technologically limited zero mark. With measurements at a radius of 1.5 mm, the detector physically contacted the source fibre previous to the addition of the phantom. Source non-uniformities or the physical size of the detection isoprobe most likely caused these errors. Other investigators have observed non-uniformities in cylindrical diffusers, but it should be noted that these non-uniformities disappeared when the diffuser was submersed into a high scattering medium, such as Intralipid or prostatic tissue [Feather et al., 1989, Murrer et al., 1996]. Newer cylindrical diffusers, such as those manufactured by Medlite (Switzerland), provide high quality, uniform light fields without the presence of a scattering medium. Interstitial PDT will require multiple light sources so it is important to be able to predict the light fields from such an array of sources. Depending on the patient's tissue optical parameters, the size and shape of the gland, the wavelength of light delivered, PDT of prostatic carcinoma may require as many as 18 cylindrical sources.[3]

[3] 18 sources would be required for a prostate 50 mm in diameter, spaced 1 cm apart in an icosohedral array using 630 nm light.

Chapter 4

Analysis of Prostatic Optical Properties

The optical properties of the prostate have been studied using a variety of methods, most using an approximation of Diffusion Theory to estimate the optical parameters of the gland. Because of this, the prostatic optical parameters are classically listed in terms of the effective transport coefficient, σ_{eff}, and the absorption coefficient, σ_a. At 630 nm, the wavelength used to excite Photofrin®, published values of the effective transport coefficient vary from 0.22±0.07 mm^{-1} to 0.44±0.07 mm^{-1} for *in vivo* samples [Lee et al., 1999]. It was determined that each prostate, however, had similar reproducible optical properties but it is still possible that the variation is a product of experimental artefact. *In vivo* samples have been reported to have similar transport coefficients as *ex vivo* samples [Whitehurst et al., 1994]. According to Lee et al. [1995], prostatic tissue, whether it is benign, malignant, hyperplastic or healthy, is optically similar within each gland, but there is optical variation between individual glands at 630 nm. Save for the analysis done by Lee et al. [1995] at 665 nm, the optical parameters of the prostate at wavelengths other than 630 nm remains virtually unexplored. With the aspiration to use photosensitizers which

absorb at longer (more penetrating wavelengths) and given the uncertainty in the optical parameters at 630 nm, each patient's prostate must still be characterized before treatment. At the very least, a comprehensive study of *in vivo* prostatic optical parameters at the clinically chosen wavelength should be performed.

4.1 Employing the P3 Approximation to Examine Prostatic Optical Properties

Six *postmortem* prostates were obtained as anatomical gifts. Samples that were older than 48 hours were already subject to putrefication, and autodestruction of the tissues was obvious. The optical properties of three *postmortem* human prostate samples obtained no later than 36 hours *postmortem* were studied. Once excised, the samples were stored in a saline solution at 4 degrees C until used. Samples older than 36 hours *postmortem* visibly showed constant physical degradation due to putrefication and autolytic decomposition of the gland, which accordingly affected the tissue optical parameters. There were no measureable changes in the photophysical properties of the tissue for samples obtained 36 hours *postmortem*. The prostate sample was exposed to air for less than 4 hours, and were constantly irrigated with saline to avoid changes in optical parameters due to desiccation. Light at 690nm from an argon-ion pumped Ti:Sapphire laser (both Spectra Physics, Beamlok 2080 and 3900s, respectively) was coupled into a fibreoptic terminated with a spherical diffuser with a diameter of 750 μm. This wavelength was chosen because BPD-MA and AlPc, which were our 2 candidate photosensitizers for interstitial PDT, exhibit strong absorption near this wavelength. Detector and source fibres were introduced into the sample via brachytherapy afterloading needles (Best Medical Technologies). The afterloading needles were position using an acrylic template with holes

spaced at 5 mm increments. The 25 mm thick template was machined with a tolerance of 0.01 mm, providing an accurate method of determining source to detector distance. Radiance measurements were taken throughout the bulk of the prostate to obtain a representative data for the range of optical parameters characterizing each prostate. Figure 4.1 shows the arrangement of the measurement points used in each prostate.

Using the nomenclature "$A \rightarrow B$" to represent "source at point A, detector at B", the arrangement of measurement points and the order in which they were sampled were: $A \rightarrow B$, $B \rightarrow A$, $B \rightarrow C$, $E \rightarrow D$, $D \rightarrow E$, $E \rightarrow F$. The spacing between measurement points was maintained at 10 mm. The variation in the lateral spacing of the measurement points (the distance between points B and E) varied in order to position the source and detector in the middle of the prostatic lobe, avoiding the urethra and the periphery. The optical parameters for each of the 3 prostate samples were determined by fitting the P3 Approximation to the experimental radiance measurements using σ_a, σ_s and g as variables. A set of 3 fluence curves were plotted using the highest, lowest and the average measured optical parameters of a single prostate. The theoretical fluence measurements were calculated using the Grosjean Approximation. The Grosjean Approximation for a point source is not as accurate as the fluence for a point source using Diffusion Theory (shown in §3.0.1.1) but Grosjean Theory's simple representation accurately represents the fluence far away from the source [Dickey et al., 2001].

The optical characteristics of the three *postmortem* prostates were calculated using the P3-approximation at 6 points around the gland. Figure 4.2 shows a typical experimental radiance measurements at one of the points and appropriate best-fit curve supplied by the P3 Approximation.

The absorption coefficient and the anisotropy factor did not vary between prostate

samples, remaining constant at $\sigma_a = 0.08 \pm 0.01$ and $g = 0.94 \pm 0.01$. Only the scattering coefficient varied, albeit with only minor inconsistencies. In one sample, the σ_s varied by no more than 5 mm^{-1} and less than 3 mm^{-1} of variation was observed in the other 2 samples.

Using Prostate 1 from Table 4.1, we find a maximum scattering parameter of $\sigma_s = 34\,mm^{-1}$, a minimum scattering parameter of $\sigma_s = 29\,mm^{-1}$ and an average of $\sigma_s = 33\,mm^{-1}$. Figure 4.3 shows the range of fluence predicted by the Grosjean approximation.

4.1.1 Discussion

The single point measurements allowed for a robust spatial characterization of the prostate to be executed. The necessity to change the source-to-detector distance with Diffusion Theory does not allow the same comprehensive spatial examination. The consistency in the optical properties of the samples tested is intuitively reassuring since all the prostates had a similar fibrous density and were distinguished by the same milky white hue. Each prostate had different morphology, with slightly different fibrous arrangement, suggesting that each prostate would transport light differently. The scattering coefficients in Table 4.1, however, indicate that the morphology has little implication on the optics of the tissue as the samples were surprisingly optically homogeneous and similar. The spread in optical parameters observed in Prostate 1 (shown in Table 4.1) resulted in the estimated spread of fluence distribution shown in Figure 4.3. From this data, the variation in σ_s would be nearly insignificant in dose planning for interstitial PDT because the variation in σ_s accounts for very little change in the delivered fluence. This also implies that tissue characterization may not be a necessary prelude to clinical optical dose planning. This, however, cannot yet be confirmed as the *ex vivo* samples are not subject to

Table 4.1: Spatial examination of prostatic scattering parameters (see Figure 4.1). σ_a and g remained constant at 0.07 mm^{-1} and 0.96, respectively.

Measurement Point	Prostate 1 - σ_s [mm^{-1}]	Prostate 2 - σ_s [mm^{-1}]	Prostate 3 - σ_s [mm^{-1}]
$A \rightarrow B$	33	32	34
$B \rightarrow A$	33	33	34
$B \rightarrow C$	34	32	35
$E \rightarrow D$	32	31	36
$D \rightarrow E$	33	32	34
$E \rightarrow F$	29	32	33

effects like swelling and bleeding that would occur *in vivo* which have an effect on tissue optical parameters at 690 nm. Tissue characterization should therefore still precede clinical application of PDT.

4.2 Examination of Boundary Effects

Boundary effects were studied by first inserting a whole prostate gland into a black painted dish. The prostate was suspended on toothpicks from the bottom of the bowl to avoid any boundary effects that the bowl/prostate interface might cause. The radiance probe was directly (and very carefully) inserted into the afterloading needle approximately 1 mm from the outside edge of the prostate. The isotropic source described in §4.1 was inserted into an afterloading needle 10 mm from the radiance probe. Radiance measurements were taken with the prostate sample suspended above the bowl. After completion of the radiance measurements, a 6% Intralipid solution was carefully added, completely immersing the prostate, without removing the source or the radiance probe from the previous measurements. Radiance measurements were repeated to compare the radiance for a prostate/air boundary to the radiance for a prostate/Intralipid boundary. The experimental arrangement is shown in Figure 4.4, and the radiance data is shown in Figure 4.5.

Figure 4.1: Measurement points used to optically characterize post-mortem prostate.

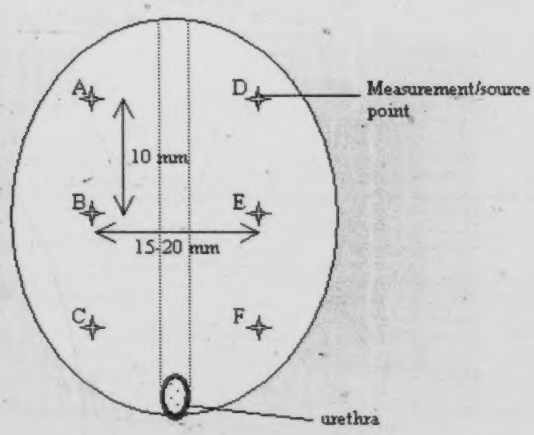

Figure 4.2: Typical radiance measurements used predict prostatic optical parameters.

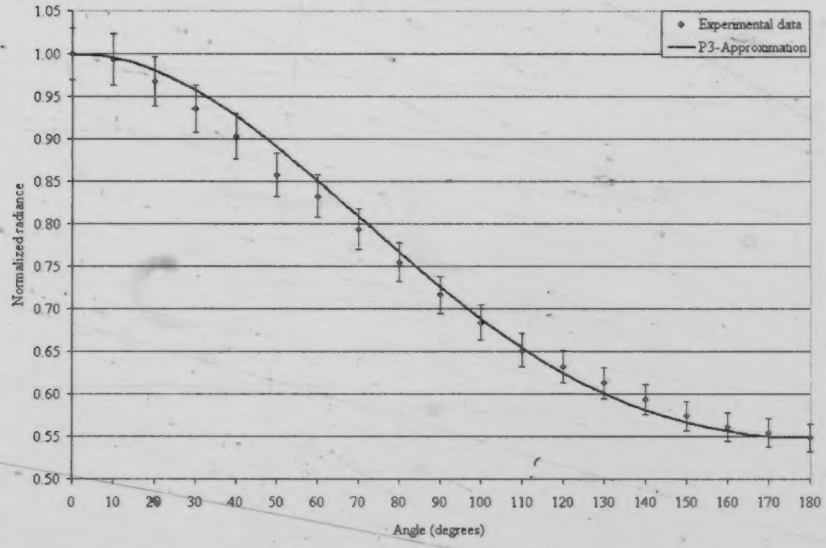

Figure 4.3: Theoretical examination of the effects of changing prostatic scattering properties on the fluence.

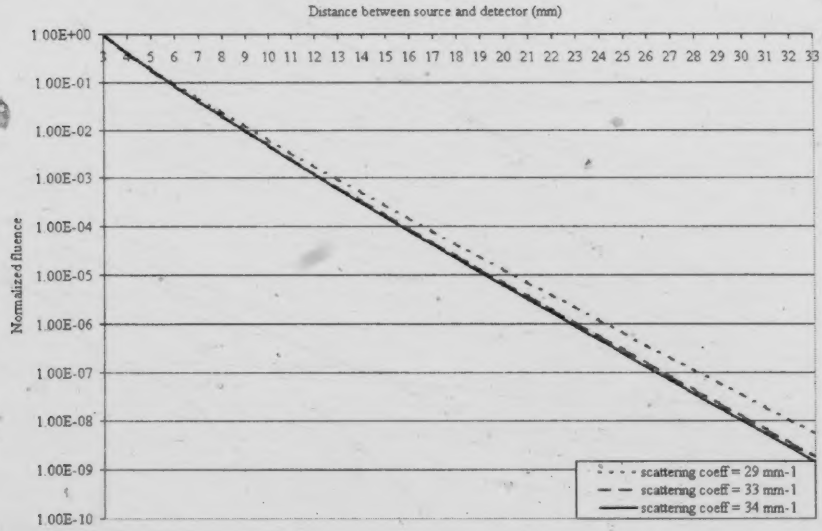

Figure 4.4: Arrangement to examine boundary effects of the boundary conditions at the prostatic capsule on radiance measurements.

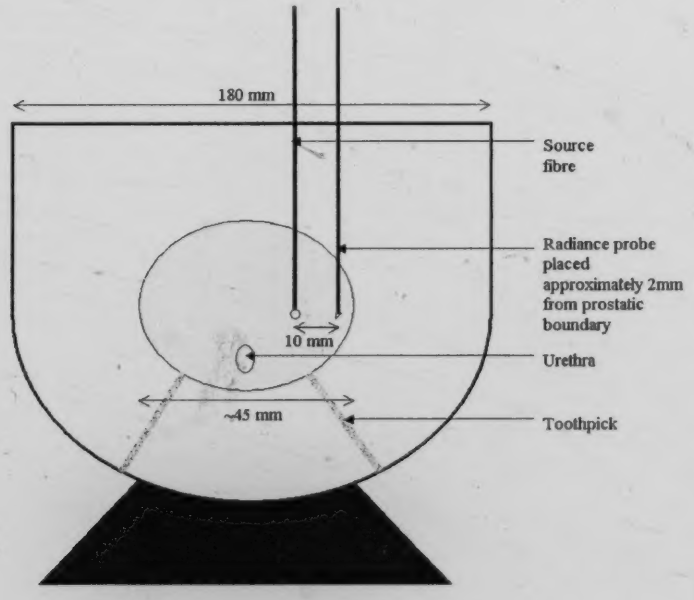

Figure 4.5: Examination of the change in radiance near the prostatic boundary after the addition of Intralipid

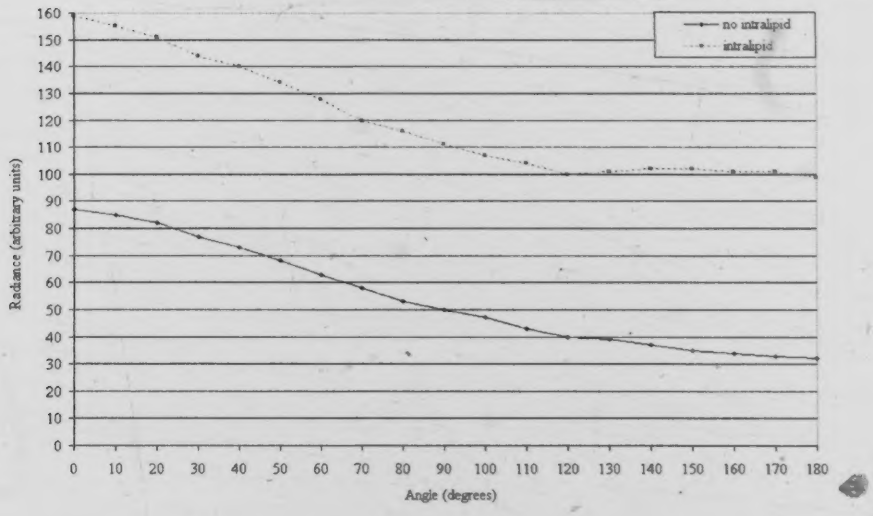

(a) Raw data showing the radiance before and after the addition of an intralipid solution

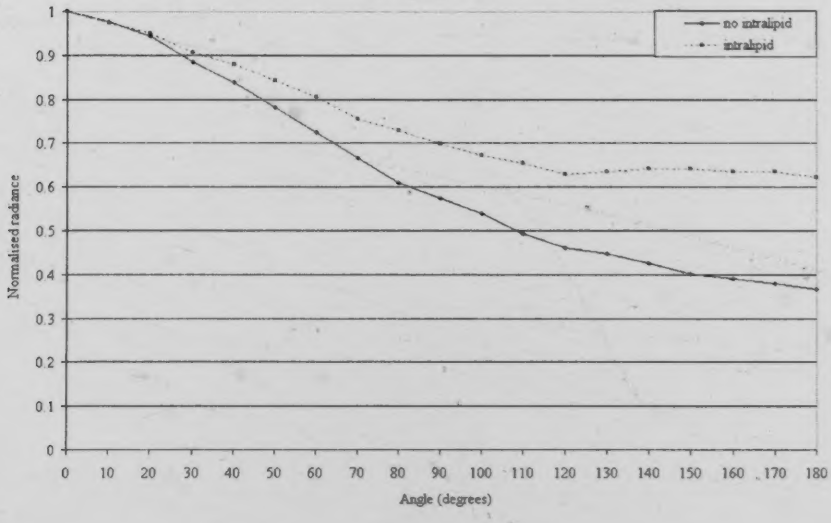

(b) Normalized data of (a)

4.2.1 Implications

These measurements show that accurate light dosimetry at the periphery of the prostate will not only require characterization of the target tissue but also the surrounding tissues. After the addition of Intralipid to the suspended prostate, the measured light level nearly doubled and with a different radiance distribution. The optical properties of Intralipid emulate the optical properties of typical adipose tissues surrounding the prostate [Flock et al., 1992]. The increase in light levels and the plateau of the radiance curve indicate that Intralipid light is scattering back into the prostate from the Intralipid. These results show that the effects of light scattered from the rectal wall, the urinary bladder, the muscles, and the fat deposits surrounding the prostate should be considered in the light dosimetry of prostate, since the P3 Approximation would determine different optical parameters for each of the radiance curves shown in Figure 4.5. The radiance data in Figure 4.2 closely resembles the radiance data in Figure 4.5b before the addition of Intralipid. The P3 Approximation fit to the radiance data in Figure 4.5b before the addition of Intralipid produced results of $\sigma_a = 0.08 \pm 0.01$ mm^{-1}, $\sigma_s = 30 \pm 4$ mm^{-1} and $g = 0.96 \pm 0.01$, which is fairly consistent with previous results. A radiance curve could not be fit with any statistical confidence to the data after the addition of Intralipid. As well, unpredictable results were noticed when the detector was proximate to the urethra. Other researchers have tried transurethral characterization of the prostate [Levy et al., 1996], finding spatial dependent results in the optical parameters of prostate tissue. This is contradictory to the results illustrated here and to those reported by Lee et al. [1995]. The membrous, muscular urethra has a very different tissue organization than the glandular tissue and one would expect that it would affect the outcome of tissue characterization.

A truly comprehensive method of predicting the light dose delivered to the prostate

will require both optical characterization of surrounding tissues and a robust light dosimetry model to deal with both architectural and optical inhomogeneity. Because of the averaging effect of the high scattering properties of prostatic tissue, small inhomogeneities will not significantly affect radiance measurements. Clinical radiance calculations will be done by a computer, which can easily ignore a few spurious data points and still be able to reliably calculate the optical parameters. The prostatic capsule-air boundary in Figure 4.5b still produced the expected prostatic optical properties, albeit with much greater fluctuation than in the bulk of the gland, but Figure 4.3 shows us that the uncertainty may not be of great concern. The P3 Approximation requires 180 degrees of data starting from the source, so every measurement point has 2 sets of radiance data. Even a larger inhomogeneity localized in half of the radiance data could be ignored if it does not significantly affect light propagation on the other half of the rotation. If all radiance data at a particular measurement point is completely inconclusive, the physician only needs to move to a different position in the gland—determination of tissue optics using radiance measurements is not spatially limited in the same way as fluence calculations.[1]

It is important to consider the effects of inhomogeneities and boundary effects but most research indicates the prostate to be homogeneous so it should still possible to characterize the tissue and deliver a predictable amount of light throughout the bulk of the gland, which would be accurate within a couple of millimetres of the prostatic capsule. Future derivations of the P3 Approximation and Huygens'-Diffusion Theory could employ more complicated geometries (and, therefore, more boundary conditions) to accommodate for light transport across the prostatic capsule. However, this would require that the surrounding tissue first be optically characterized before light transmission across the boundary could be confidently determined.

[1]Clinical radiance is discussed further in §5.2.2 .

Chapter 5

Photodosimetry System for PDT

5.1 Introduction

Prior to 1980, therapeutic light was delivered to the target using high energy arc lamps and a series of filters and lenses. In 1980, with the commercialization and availability of fibreoptic and laser technology, there was a resurgence in examining PDT as a clinically viable oncological treatment modality. Many research and clinical PDT systems have since been constructed. The construction of early PDT systems was focused on the readily available hematoporphyrin-based photosensitizers. To generate the 630 nm light necessary for PDT, most research and clinical systems used noisy, labor-intensive argon ion pumped tuneable dye lasers. Early in PDT research, it was noted that any massive tumour required multiple fibre implants in order to achieve a uniform irradiation pattern [Bolin et al., 1987]. To treat solid internal malignancies, most PDT delivery systems emulate the one described by Arnfield [1989], in which light generated by a dye laser is split into several fibre optics terminating in cylindrical diffusing tips that can be introduced into the tumour via brachytherapy afterloading needles. Lee et al. [1996] used this technique

to successfully treat the Dunning R3327-AT6 flank tumour in a rat. Lee then used a similar delivery protocol to treat canine prostate [Lee et al., 1997]. The canine model has been shown to closely emulate the optics of human prostate tissue [Lee et al., 1997].[1] Using Photofrin®, Lee reported a radius of tissue necrosis due to PDT of ~5 mm surrounding each of the 7 fibres implanted during PDT. This is approximately equivalent to 2δ at 630 nm. Lee et al. [1999] then extended delivery hardware based on the arrangements used to treat canine prostate and the flank tumours to describe a system and protocol to treat human prostate. Using Transrectal Ultrasound (TRUS) to image and guide the insertion of 2 Morgenstern stabilization needles (E-Z-EM Ltd, UK), the prostate was fixated. Also under TRUS, afterloading needles were inserted via the perineum into the gland under the guidance of a template. PDT was then administered using Photofrin®. Using the second generation photosensitizer motexafin lutetium (Lu-Tex), which preferentially absorbs 732 nm light, Hsi et al. [2001] also successfully treated canine prostate. Hsi concurrently investigated the possibility of delivering light via the urethra, but found that this induced obvious trauma producing the unacceptable side-effect of urinary incontinence. The dogs treated with interstitial sources suffered no urinary side effects. From interstitial irradiation, Hsi reported a radius of necrosis from PDT to be approximately 12 mm—much greater than the radius of necrosis of 5mm reported by Lee. Unfortunately, neither Lee nor Hsi explicitly characterized the prostate before PDT. The 732 nm light should penetrate deeper than 630 nm, but it is difficult to determine how the radius of necrosis relates to the penetration depth of the 732 nm light without tissue characterization preceding treatment. The increased radius of necrosis could depend on the photosensitizer, as second generation photosensitizers (like Lu-Tex) tend to be more potent at much lower concentrations than the

[1] Canine prostate has been shown to absorb 30% more light than human prostate.

photosensitizers that are presently clinically available,[2]

All the aforementioned light delivery systems garnered some success in showing how PDT could be used treat prostatic tissue without damaging surrounding tissues. However, their conservative approaches left much of the prostate untreated even though the consensus in the literature is that the entire prostate must be destroyed to confidently eradicate the disease. In order to treat the entire prostate with the technologies available, a robust treatment planning model and/or method of monitoring PDT progress is required. Treatment-planning models for PDT exist, but have not been integrated into the existing delivery systems, lacking the mathematical and technological sophistication necessary for accurate light dosimetry [Jankun et al., 2000]. The aforementioned delivery systems also lack the capability to monitor the progress of PDT.

Ideally, to comprehensively monitor the progress of PDT, the fluence rate, photosensitizer concentration and oxygen availability should be measured. All 3 quantities are known to be dynamic throughout the course of PDT: light fluence drops due to changing tissue parameters [Chen et al., 1997], photosensitizer may be consumed by a process called photobleaching [Boyle and Dolphin, 1996] and the oxygen is consumed during the photodynamic reaction. To date, only one PDT system, developed by Johansson et al. [2002], has been reported to monitor the progress of a PDT session: it is capable of detecting changes in tissue transmissivity; it uses fluorescence to determine the presence (but not the concentration) of the photosensitizer. There is unfortunately no mention of monitoring oxygen availability other than suggesting quantitative oxygen (and photosensitizer) detection should be included in future iterations of their delivery system. But this system still appears to lack crucial characterization methods. Without the robust knowledge of the tissue

[2]The radius of necrosis also depends upon the local concentration of the photosensitizer. Detail on the role of the photosensitizer on dosimetry is addressed further in §5.2.5 and §6.1

optics, it is difficult to determine how light energy truly corresponds to the efficacy of the delivered treatment.

5.1.1 Comprehensive Light Delivery System.

In this chapter, we describe a comprehensive switched light delivery system for interstitial PDT capable of real-time monitoring of light fields. The system is built using existing fibreoptic and computer technology. The system determines tissue optical parameters using radiance measurements and is capable of simultaneously delivering and detecting tissue fluence levels. Switching fractionates light delivery, permitting tissues to go through a dark period, thereby allowing tissue oxygen levels to replenish, increasing the efficacy of PDT [Muller et al., 1998]. The control software for the delivery system (LabVIEW and C/C++) analyzes and displays the light fields, controls the hardware and archives the data attained during PDT. To illustrate the operation of the system, preliminary results treating the Dunning R3327-AT6 and -H tumour cell lines and canine prostate are given.

5.2 Light Delivery System

This flexible computer controlled photodynamic therapy system is constructed from commercially available laser, optoelectronic and fibreoptic technologies. The system facilitates both tissue characterization and therapeutic light delivery. The system is capable of concurrently delivering therapeutic light and monitoring changes in the tissue optical transmissivity to ensure the that a lethal light dose is being delivered only to the target volume.

The therapeutic fibreoptic delivery system is comprised of 5 main components: a fibre optic switch, diode lasers, PDT fibreoptics, optical detector, and control

computer. However, before PDT is administered, the target optical parameters are calculated by the P3 Approximation based on *in vivo* radiance measurements. The optical parameters are calculated using the same laser sources and control computer as the therapeutic system. Using these optical parameters, the control computer calculates the optimum irradiation parameters for PDT. A schematic of the radiance motor and close-up of the radiance probe are shown in Figure 5.1. A schematic of the system operating in both delivery and detection mode is shown in Figure 5.2. A photograph of the delivery system is shown in Figure 5.4.

5.2.1 Laser Sources

There are 2 individually controlled laser diode modules (Optical Fiber Systems, Inc.). They are complete turn-key laser systems including driver electronics and a thermoelectric cooler, and a fibre pigtailed laser diode capable of producing up to 500 mW of 690 nm light. The choice of wavelength was largely dictated by the chosen photosensitizer. To test this delivery system, the photosensitizer QLT-0074 (BPD-DEA, QLT Phototherapeutics) was used. This photosensitizer, which is related to BPD-MA, shows strong absorption and photodynamic effect at 690 nm. This wavelength of light offers approximately twice the penetration depth than 630 nm in most tissues.

5.2.2 Tissue Characterization

Experimental radiance measurements are taken using a radiance probe, which is constructed in-house by mounting a right angle prism on a flat-cleaved 400 μm fibre optic. The prism is protected by a thin glass sheath. The outer diameter of the radiance probe is 1.4 mm.

The radiance probe is secured into a bare fibre chuck. The chuck is secured with set screws into the rotary stage. The rotation of the stage (National Aperture Inc., Micromini Motor) is controlled by a stepper motor system (National Aperture Inc., Micromini Controller) that is computer controlled via RS-232 communication protocol. Data are acquired by rotating counter clockwise 180 degrees, taking measurements every 15 degrees, and then rotating clockwise a full 360 degrees, taking data every 15 degrees. Radiance data is recorded from several locations around the prostate. The data are then processed by the control software to determine the optical parameters of the target. Optical parameters are determined by analyzing the experimental data using the P3 Approximation [Dickey et al., 2001]. If there are in consistencies with the results furnished by the P3 Approximation, measurements may be repeated. Because the prostate has been shown to be fairly homogeneous around the volume of the gland, the tissue coefficients may be averaged. The tissue coefficients are then used to determine the optimum irradiation parameters for treatment.

5.2.3 Fibreoptic Switch

The implementation of a fibreoptic switching system offers advantages over classical methods of delivering light wherein the laser light is split evenly into cylindrical diffusers which are introduced into the treatment area. First, switching allows for two concurrent actions to be executed, namely delivery and detection (or potentially, another diagnostic tool). As mentioned in §5.2, it has been shown that fractionating the light delivery augments the efficacy of photodynamic therapy by allowing areas of the target to go through a dark period to permit reoxygenation [Muller et al., 1998].[3] The therapeutic light is delivered using a custom fibreoptic bidirectional

[3]The topic of oxygen influence on PDT dosimetry is addressed further in §6.2 .

optical switch (LIGHTech Fiberoptics, Inc), connectorized with SMA905 connectors. This switch integrates two 1x2 and two 1x9 switching modules. Connecting the input of one of the 1x2 switches with the input of a 1x9 switch, one effectively creates two multiplexed 2x9 switches. The switch is interfaced with the computer using GPIB communication protocol. The diode lasers each connect to an open port of the 1x2 modules. The laser light travels through the 1x2 switch to the 1x9 switch. Fibreoptics terminating in cylindrical diffusing tips are connected to the 1x9 switch. Light is delivered to the tumour by sequentially switching the laser sources.

The configuration of the system is such that when one of the 1x9 switches is used as a source, the other may be used as a detector. Each laser source is connected to one of the 1x2 switches and the other input is connected to the power detector. The output from each 1x2 switch is then input to one of the 1x9 switches. This combination of switches allows for a real-time method of monitoring the relative changes in tissue transmissivity over a PDT session.

The optical power levels in tissue are measured in the neighboring cylindrical diffusers to the source fibre. However, absolute measurements are not possible. In order to convert the light measured by the power meter into a fluence, the detecting characteristics of the diffusers would have to be characterized to determine how the light collected correlates to the light in the tissue. Furthermore, one would have to fastidiously account for the losses accrued through the connections. The accuracy of the Huygens-Diffusion model is relied upon to predict localized fluence based on the output power of the diffuser. The primary purpose of measuring the optical power is to monitor the changes in power levels. For this, only relative light power measurements are required.

The light collected from the tissue is transmitted through the switch to a 152 mm integrating sphere (Melles Griot - 13 ISP 003). An integrating sphere is used to mea-

sure the relative intensity of a wide-angle or an inhomogeneous beam. Integrating spheres average light by multiple diffuse reflections in order to obtain meaningful intensity measurements, even in low light conditions. The light collected by the integrating sphere is quantified with a universal power meter (Melles Griot, 13 PDC 001). High detector sensitivity is necessary since there is often very little light to collect at low power PDT, due to tissue absorption and losses accrued through the various connections with the fibre optics and optical switch.

An example of a treatment cycle would have the first 1x2 module switched to laser source #1 and the desired output fibre of the related 1x9 switch delivering light to the tissue. Meanwhile, the other 2x1 switch is selected for detection, and the fibres near the source scanned, taking an optical power measurement at each location. The power at each location is then communicated to the computer, thus allowing for real-time dose monitoring. This continues until each fibre in the array has been used as a source, and the corresponding light levels in nearby fibreoptics measured. Note that the switching speed for the optical switch is approximately 150 ms, which is negligible when compared to the total treatment time. The switching cycle repeats until the prescribed dose has been reached.

5.2.4 Delivery Fibreoptics

The fibreoptics terminated with 15 mm cylindrical diffusing tips were used (Polymicro Technologies). In the Dunning tumours, the penetration depth of 630 nm light is about $\delta = 8$ mm. Since the tumours have an average diameter 25 mm, seven fibre optic implants spaced at 10 mm apart in ain icosohedral array are necessary for uniform irradiation.

The fibre optics are introduced into the tumour via translucent plastic afterloading needles identical to those used in brachytherapy (Best Medical Industries). The fi-

bres alternate between fibreoptic switches such that detector and source fibres are equally distributed. For uniform irradiation, an icosahedral arrangement of fibres is used, wherein the distance between neighboring fibres is always equal, as illustrated in Figure 5.5. However, the fibre arrangement could be adjusted to suit the morphology of the target.

5.2.5 Control System Software

There are 3 components to the delivery system software - diagnostic component, delivery component and a unifying control program.

The diagnostic component is responsible for the calculation of the optical parameters. Written in C, this program fits the P3 Approximation to experimental radiance data using DUD curve fitting protocol to determine σ_s, σ_a, and g [Talston and Jennrich, 1978].[4] These components are then passed to the delivery component.

The delivery component's primary task is to ensure that a safe tumouricidal light dose is delivered only to the target volume. Written in C++, it calculates the optimum irradiation parameters based on the optical parameters determined by the diagnostic component. There are 2 possible modes for the delivery program.

In Mode 1, the user defines the total light energy to be delivered and the input diffuser power; the computer returns the treatment time and displays the isodose fields for review, as shown in Figure 5.6. The results are passed to the third component to await the operator to begin treatment. Mode 1 was used in the experiments explained in §5.2.6 (treatment of rat flank tumours) and §5.5 (treatment of canine prostate).

In Mode 2, the user enters the placement of the needles and the desired radius

[4]The DUD protocol is a widely accepted derivative-free curve fitting procedure.

of necrosis then the treatment time is calculated and diffuser power is calculated based on the desired radius of necrosis (r_{nec}) using the known photodynamic kill effect ($r_{i_{nec}}$) at a given irradiance (ϕ_i). The radius of necrosis is expressed by

$$r_{nec} = r_{i_{nec}} + \delta \ln[\frac{\phi}{\phi_i}] \tag{5.1}$$

[Jacques, 1992].

Knowing the target optical parameters, Huygens-Diffusion Theory can calculate the necessary power of the cylindrical diffusers to achieve the desired necrotic region [Dickey et al., 2004]. A graphical image of the isodose is returned. If the user is content with the results, the appropriate information is passed to the third component. After the laser power is set appropriately, the user may initiate the third component. For an intravenous Photofrin® dose of 2 mg/kg intravenous, diffuser power of 150 mW/cm and total dose of 450 J, the radius of necrosis was experimentally determined to be approximately 2.5δ in canine prostate tissue [Lee et al., 1997]. The radius of necrosis is affected by the concentration of the photosensitizer, but it is not clear how changing the systemically administered dose of photosensitizer affects the accumulation in the target volume. Mode 2 can be employed only with a detailed understanding of the phototoxicity of the photosensitizer and light.

The 3rd component is responsible for the timing and sequencing of the switching hardware and light detection. Once initiated, this component, developed with LabVIEW (National Instruments Inc), runs until the prescribed dose or necrotic region is achieved. It also records and displays the changes in tissue transmissivity

5.2.6 Treatment of Dunning R3327-AT and -H Tumour

It is the goal of this experiment to determine the ideal dwell time on each fibre for a particular drug dose, and to compare the efficacy of time fractionated delivery to continuous light delivery. To achieve this, we will use the light dosimetry system to treat the Dunning R3327-AT and -H prostate tumours, which are known to be good representation of PCa. The Dunning R3327-AT and -H rat prostate tumours have been propogated in the Moore lab for many years. The tumour is maintained by serial and parallel passage in Fisher-Copenhagen F1 male hybrids, which are bred in the vivarium at the Cross Cancer Institute. Male rats greater that 10 weeks of age are implanted subcutaneously in the flank with 2 mm cubes of tumour. Tumour size is monitored weekly by caliper measurement ($\frac{\pi L_1 L_2 L_3}{6}$) until the tumours reach a volume of 2 cm^3 is reached. This (latency) takes approximately 40 days for the -AT tumour and 200 days for the -H tumour. For this experiment animals were photosensitized with photosensitizer QLT-0074 at 1.5mg/kg. Following 3 hrs for biodistribution, the animals were anaesthetized (Ketamine 75 mg/kg, Xylazine 7.5 mg/kg, intraperitoneal) and underwent pretreatment perfusion imaging with Gadolinium small-parts MRI. Following imaging, tumours were treated with 900 J using the multi-fibre delivery system, with a dwell time of 100 s on each fibre. We experimentally determined the most effective dwell time to be greater than 30 seconds for the -H tumour.The temperature was monitored via an interstitial thermocouple (Omega Inc), implanted alongside the cylindrical diffuser. The temperature of the tissue never varied during PDT, remaining constant at 31° C. The animals were permitted to recover and at 24 hours post-PDT the rats were reimaged with Gadolinium perfusion MRI. The animals were followed for tumour growth and cures. Perfusion effects and dosimetry will be compared to treatment outcome. The controls underwent implantation, imaging, and light without photosensitization.

5.3 Results

Some results demonstrating the capabilities of the delivery system are shown here. The ideal switching time, drug dose, and light dose for the tumour models are still being determined; however, preliminary results appear quite favorable.

Figure 5.7 shows Gadolinium perfusion MR images of a rat implanted with the Dunning R3327-H tumour, 1 hour before PDT, 1 hour after PDT and 24 hours after PDT. In Figure 5.7a, 1 hour before PDT, the tumour shows good perfusion. One hour after PDT, Figure 5.7b clearly shows that PDT has effectively shut-down the vasculature of the tumour mass. Occlusion of the vasculature and the resulting hypoxia is a primary effect of PDT [Fingar and Henderson, 1987]. Tumour death is partially related to the PDT induced hypoxia, so the continued vasculature shut-down illustrated in Figure 5.7c is indicative of potentially successful PDT.

The rat imaged in Figure 5.7 is shown in Figure 5.8. In Figure 5.8a, 1 day after PDT, the tumour mass is clearly visible. In Figure 5.8b, one week after PDT, the tumour area is clearly necrotic. By 3 weeks, the tumour mass has disappeared.

A key advantage of the light delivery system is in its ability to detect changes in tissue transmissivity. Using the fibre arrangement illustrated in Figure 5.9a, Figure 5.9b shows the changes in the tissue transmissivity during 3 separate PDT sessions: treatment of a Dunning R3327-H tumour with QLT-0074, treatment a Dunning R3327-AT tumour with QLT-0074 and treatment Dunning R3327-H tumour with light only.

5.4 Discussion

This delivery system and protocol combines dose planning with the ability to monitor optical changes in the treatment volume thereby allowing safe light delivery to the patient throughout the course of the treatment session. Figure 5.9 shows that tissue transmissivity falls throughout the course of a PDT session. This reduces the possibility of damaging proximate sensitive organs, but could limit all parts of the target volume from receiving a lethal dose. It would seem likely that one could fit a simple exponential function to each of curves to the data shown in Figure 5.9b to determine the changes in tissue absorption. The computer could then extend the treatment time to ensure all regions receive sufficient light.

The decrease shown in tissue transillumination has been reported by other investigators [Chen et al., 1997]. Some investigators have reported that pooling of blood around the fibreoptic will reduce the detected light. Virtually no change was observed in the transmissivity in the control animal, implying that observed optical change was caused by altered photobiology due to the PDT reaction. Fundamental to the PDT reaction is the presence of oxygen. As oxygen is consumed, oxyhemoglobin (HbO_2) is converted to deoxyhemoglobin (Hb). Hb is much more strongly absorbing than HbO_2 at visible wavelengths. The PDT reaction causes a shutdown in the vasculature, thereby preventing blood flow through the target. Without being able to transfer oxygenated blood into the target, all the oxygenated blood will be consumed, leaving the highly absorbing Hb. Greater relative changes in the optical transmissivity are observed in the -H tumour than the -AT tumour. The slower growing -H tumour is better vascularized than the -AT, facilitating greater blood volume and potential change from HbO_2 to Hb [Arnfield et al., 1993]. Chen et al. [1997] reported greater than 50% drop in fluence over the course of the treatment. We observed a much smaller change. However, using 630 nm light, there is

a considerable difference between the absorption of HbO_2 to Hb, compared to the difference in absorption at 690 nm. $E_{690}^{HbO_2}$ = 276 L mol^{-1} cm^{-1}, E_{690}^{Hb} = 2051L mol^{-1} cm^{-1}, $E_{630}^{HbO_2}$ = 610 L mol^{-1} cm^{-1}, E_{630}^{Hb} = 5148 L mol^{-1} cm^{-1}.

As well, the blood volume in the prostate is likely greater than the flank tumours, and the higher concentration of Hb will likely increase absorption of the target.

One would therefore expect a greater change in the tissue transmissivity at 630 nm than at 690 nm. The change in optical parameters may be linked to the oxygen concentration. As all the oxygen is consumed, and the vasculature is blocked due to PDT reaction, it may be possible to predict an effective end point to a PDT session by monitoring changes in tissue transmissivity; i.e., when tissue transmissivity no longer changes, all the oxygen has been consumed.

5.5 Treatment of Canine Prostate

As only 2 dogs were treated, results of treating canine prostate are presently inconclusive. The results of the experiments are still detailed here as they do support the utility of the switched system. However, this treatment was used in conjunction with a novel drug delivery technique, intra-arterial administration. In this technique the drug is delivered directly to the prostate. Details of the intra-arterial administration of photosensitizer is in Appendix 3.

5.5.1 Method

Two male dogs were treated using an automated light delivery system - 1 large male mongrel dog and 1 purpose-bred male beagle. The dogs were anesthetized, place on their backs, then sterilely prepped and draped. Using a unilateral femoral

puncture, a tracking angiographic catheter was inserted into the vesico-prostatic artery bilaterally under fluoroscopic control. QLT-0074 (1.5 mg/kg) was injected via intra-arterial catheter. Multifibre interstitial PDT was performed using a computer controlled light delivery system. The prostate was approached via a midline incision. Acetyl afterloading was implanted in a hexagonal array, into which light delivery and detection fibres may be inserted. PDT commenced 20 minutes after drug injection. At completion, the afterloading needles were removed, the incision closed and the dogs permitted to recover. The dogs were monitored, including urinary control for 3 months. Following the observation period, the dogs were sacrificed and necroscopy of the pelvic organs carried out.[5]

5.5.2 Results

The monitoring of the tissue transmissivity during PDT was effected for both dogs. The results for the large male mongrel dog are shown in Figure 5.11. The changes in tissue transmissivity for the smaller purpose-bred beagle are shown in Figure 5.12.

5.5.3 Discussion

The treatment of the canine prostates was met with mixed success. The mongrel dog spontaneously voided after treatment, and appeared healthy. Unfortunately, the dog died of unknown complications after PDT, with the most likely cause of death being uncontrolled internal bleeding. But the prostate was destroyed and both the prostatic capsule and urethra were unharmed. The goal to destroy the prostate without damaging proximate organs was achieved, but with the unacceptable consequence of the dog's death. Furthermore, the dynamics of the photosensitizer concentrations

[5] At the time this thesis was written, one dog was still under observation.

via intra-arterial administration are not clearly understood. The photosensitizer in arterial blood will clear rapidly, increasing tissue transmissivity as the concentration decreases but the PDT reaction should cause the tissue optical parameters to decrease. Monitoring the changes in tissue transmissivity shows little correlation to treatment outcome.

The second dog recovered well, but is yet to be sacrificed for follow-up examination of the pelvic organs. Figure 5.12 shows minimal change in the transmissivity of the prostate during treatment. There were difficulties cathertizing the artery for intra-arterial delivery of the photosensitizer to the prostate. It is possible that this animal did not receive sufficient drug dose to the gland. The curves in Figure 5.12 are similar to the monitoring of the control animal in Figure 5.9b: there was a slight increase in transmissivity over the course of treatment. This also indicates that there was insufficient drug for a photodynamic reaction. These uncertainties will likely be addressed by necroscopy of the pelvic organs.

5.6 Conclusions

A tumouricidal photodynamic dose depends upon the concentration of photosensitizer. Knowledge of the photosensitizer concentration before treatment would provide valuable information in determining the potential photodynamic effect. Unfortunately, drug detection has not yet been integrated into this delivery system. Using fluorescence to detect photosensitizer concentration is a possible solution that would integrate easily into the present system configuration. Unfortunately, an optical system for drug detection will be complicated by the changes in tissue transmissivity, especially since fluorescence will involve 2 wavelengths of light. However, some quantification would be greatly helpful, like the initial concentration or even just confirming its presence.

Technically, the system performed reliably, but improvements are still possible. LabVIEW provides a clear and accurate environment to run this system, but the higher level language is computationally burdensome. As well, LabVIEW is not efficient at parallel processing; therefore, programming improvements for the full software will have to come from the implementation of more efficient C/C++ code. The universal power detector provides high sensitivity quantification of light, but is slow to capture accurate results, preventing accurate light detection for switching cycles shorter than 5 seconds. This is not a critical issue since the ideal fractionation times seem longer than 30 seconds, but it would be insightful to monitor tissue absorption changes at shorter cycle times.

An immediate, commercially available improvement to the utility of our delivery system would be the addition of computer controlled laser diodes. This would allow the output of the fibre to be optimized for its position in the target and to account for changing optical parameters. With the equal output to all fibres, their positions must be spatially optimized for uniform photodynamic effect, which is difficult for targets with irregular morphology. With the ability to vary the output power, fibres near sensitive structures could be assigned lower powers to reduce the risk of collateral damage. The extent of tissue necrosis is dependent upon the fluence, but fluence drops during treatment. Using the switching system, the therapeutic effect can be adjusted by increasing the dwell time on each fibre, which should have the same effect as increasing the fluence. If increasing the dwell time does have the same effect as increasing the laser power, the latter would be clinically preferred in order to decrease treatment time. The delivery software has always included the ability to account for each implanted fibre having its own unique output power.

Figure 5.1: Schematics of the radiance probe.

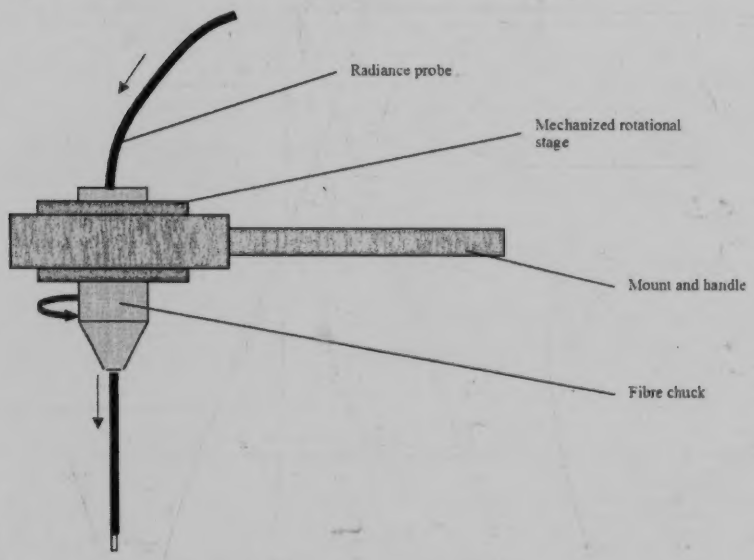

(a) Mechanized radiance probe

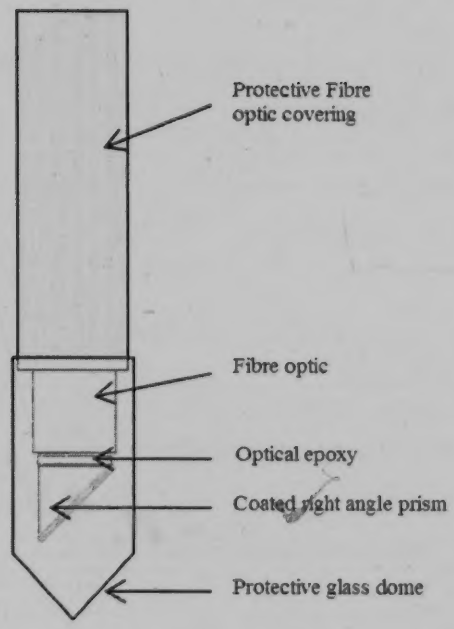

(b) close-up of radiance probe

Figure 5.2: Schematic of the light delivery system in delivery mode

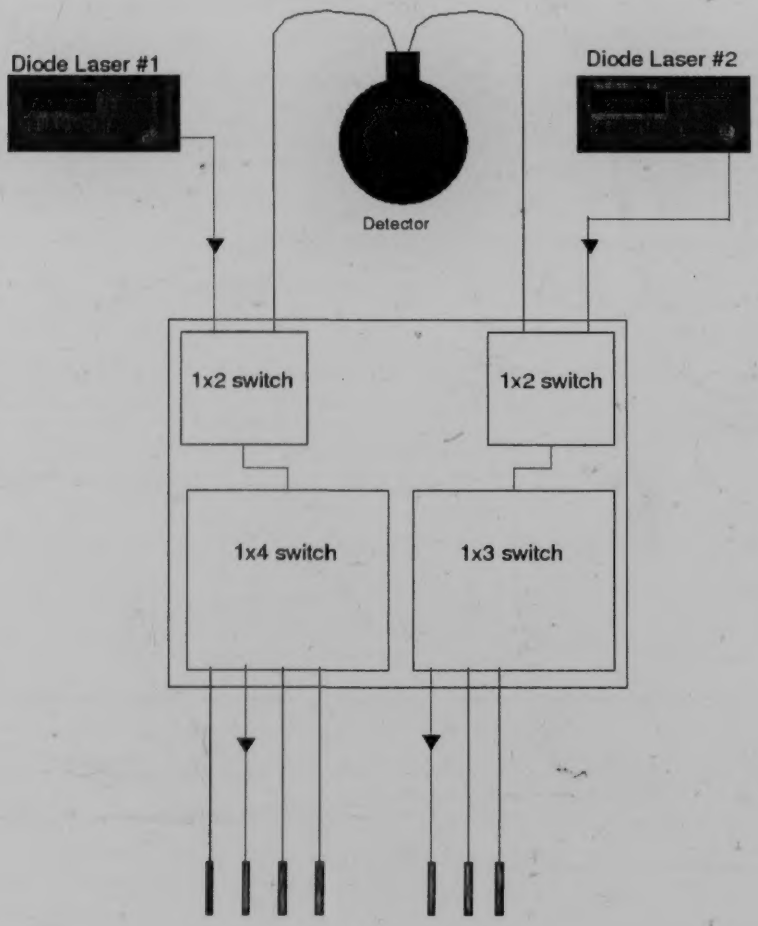

(a) In delivery mode

Figure 5.3: Schematic of light delivery system in detection mode

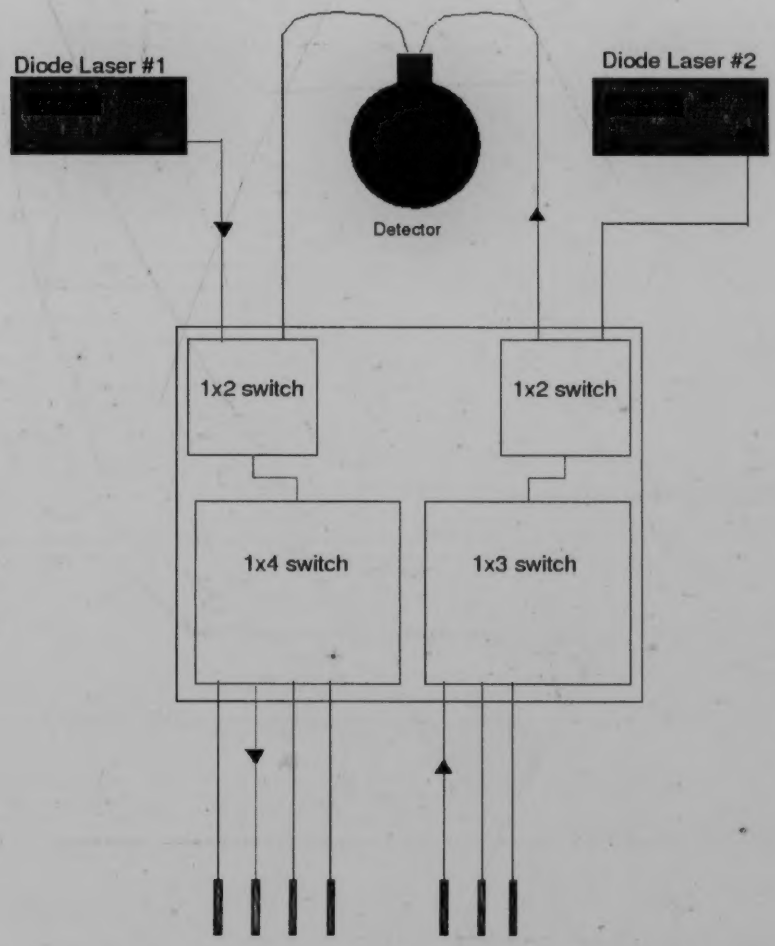

(a) in detection mode

Figure 5.4: Photograph of light delivery system. The control computer is shown in the background.

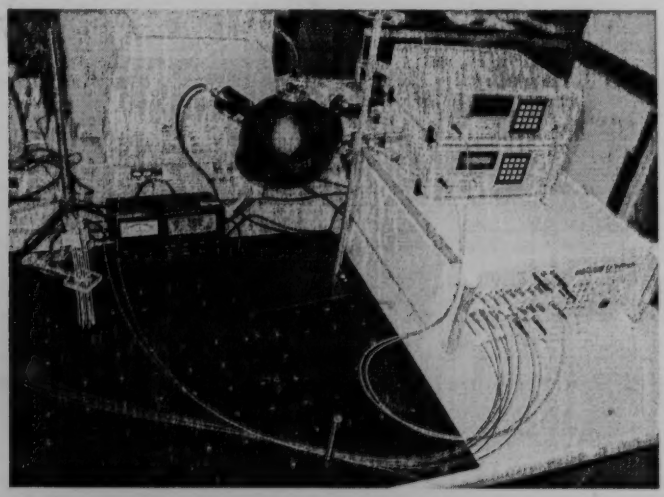

Figure 5.5: Icosahedral arrangement of fibre optics. The cylindrical diffuser's long axes run into the plane of the page.

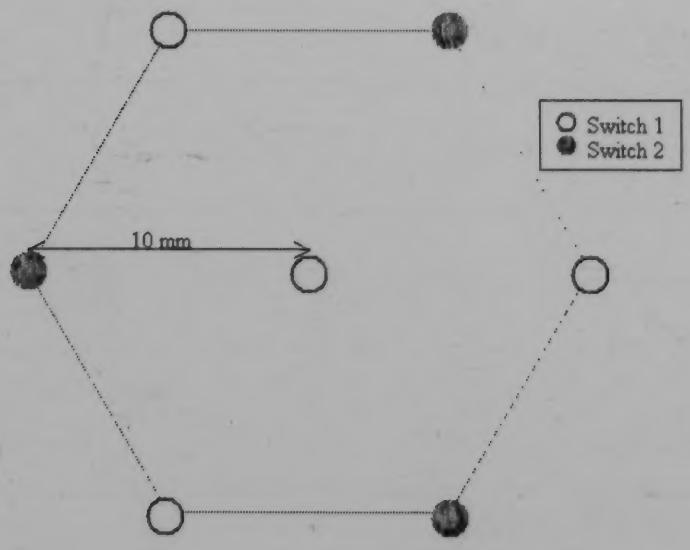

Figure 5.6: Isodose plots for seven cylindrical fibre optic. Grey indicates the area occupied by the diffuser. Red indicates a high dose; violet indicates the penetration depth.

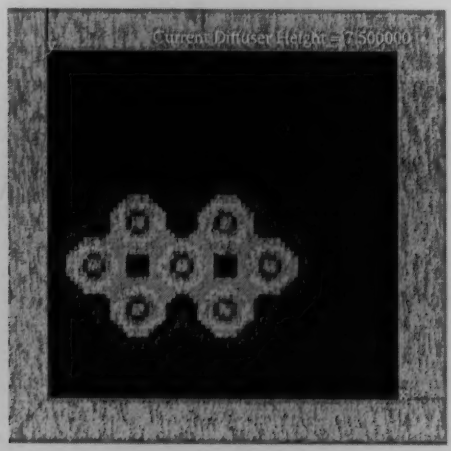

Figure 5.7: Gadolinium perfusion MRI of rat implanted with Dunning R3327-H flank tumour.

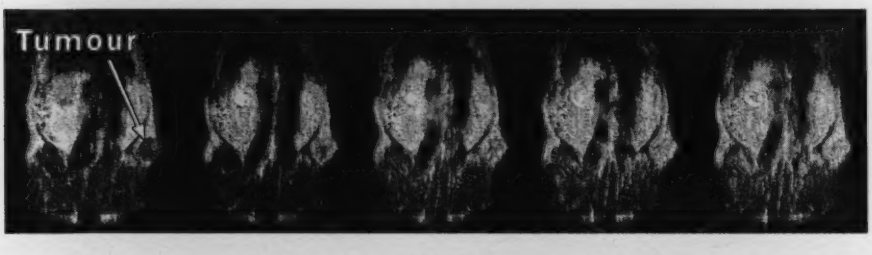

(a) MR image acquired 1 hour prior to PDT. The tumour is showing good perfusion.

(b) MR image acquired 1 hour post PDT. The tumour is dark compared to (a), indicating little perfusion. The occlusion in the vasculature is partially indicative of successful PDT.

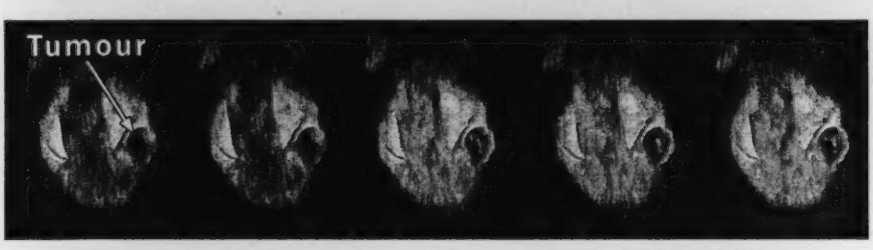

(c) MR image acquired 24 hours post PDT. The continued occlusion of the vasculature will cause hypoxia, leading to the tumour's death..

Figure 5.8: Rat with Dunning R3327-H tumour treated with the switched light delivery system

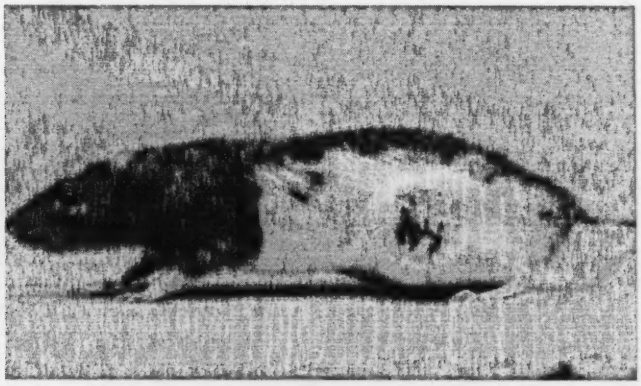

(a) 1 day post PDT

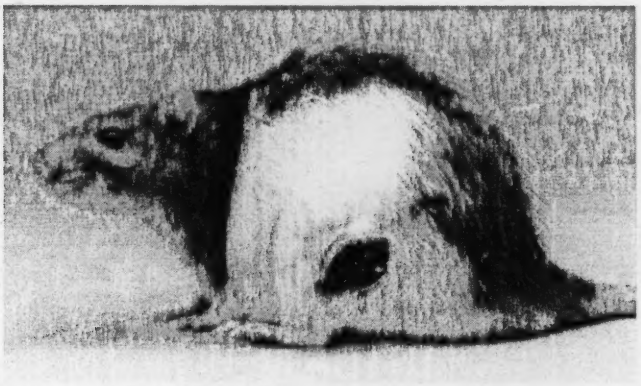

(b) 14 days post PDT

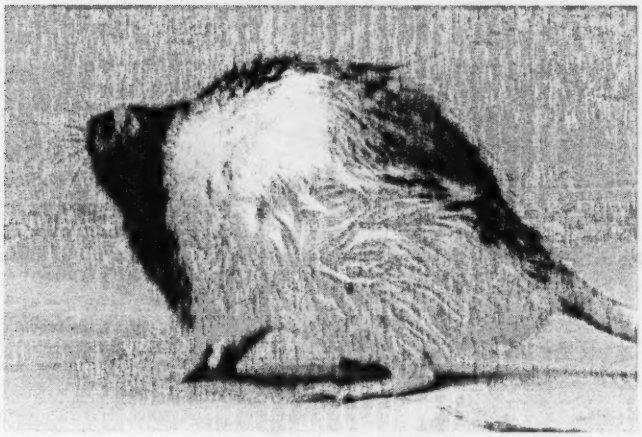

(c) 24 days post PDT

Figure 5.9: Changes in tissue transmissivity during PDT in Dunning R3327-AT and -H tumours.

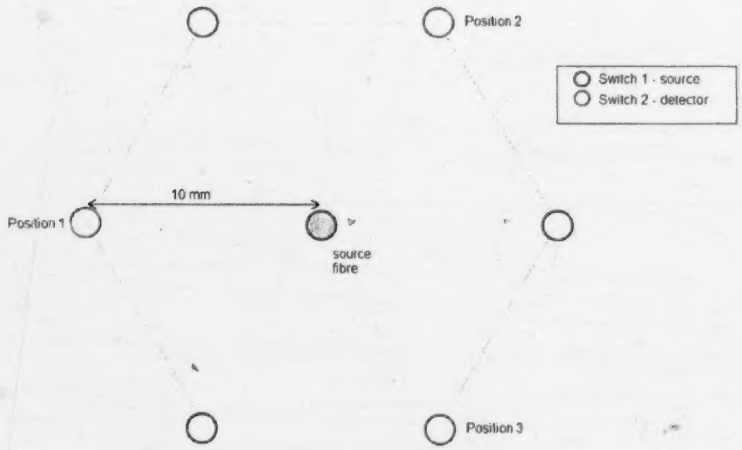

(a) Positions of fibres compared to central source fibre.

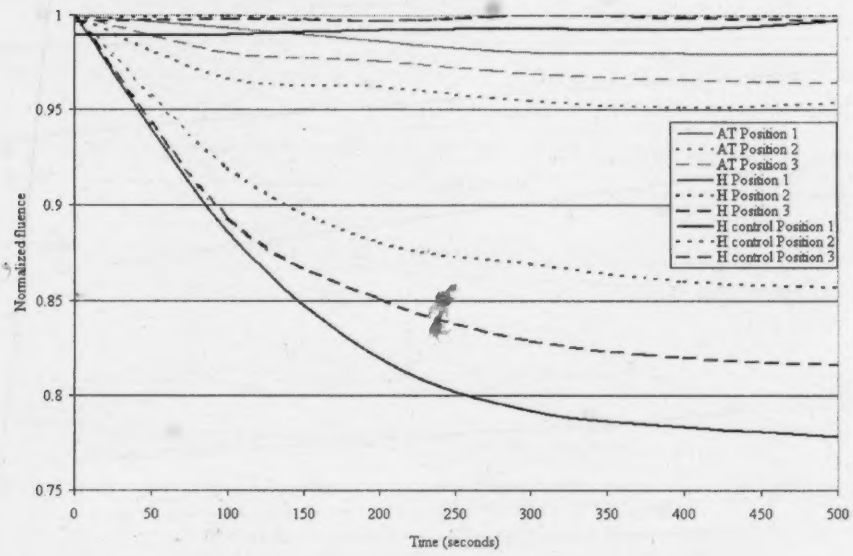

(b) Changes in transmissitivity during PDT in a Dunning R3327-H and R3327-AT tumour using QLT-0074. A control is also shown, where light was administered without photosensitization.

Figure 5.10: Hemoglobin absorption from 600 to 770 nm

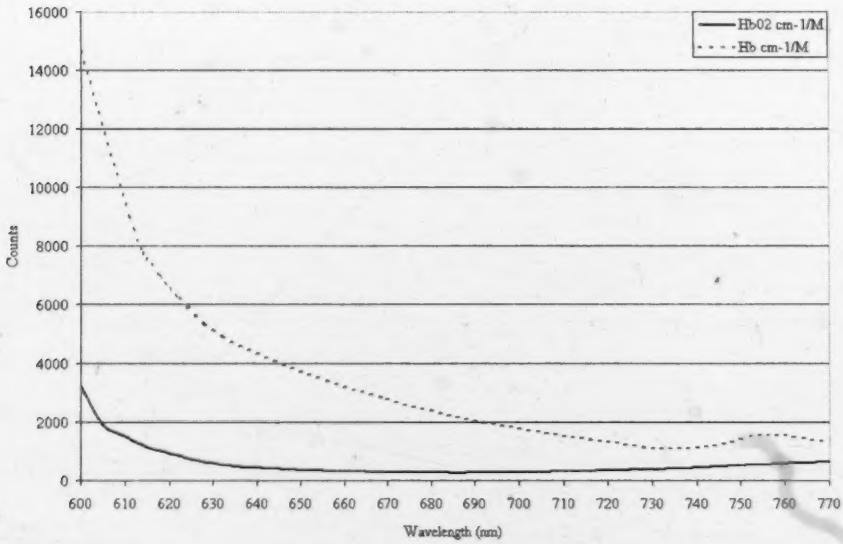

Figure 5.11: Monitoring the tissue optical parameters of the large male mongrel dog

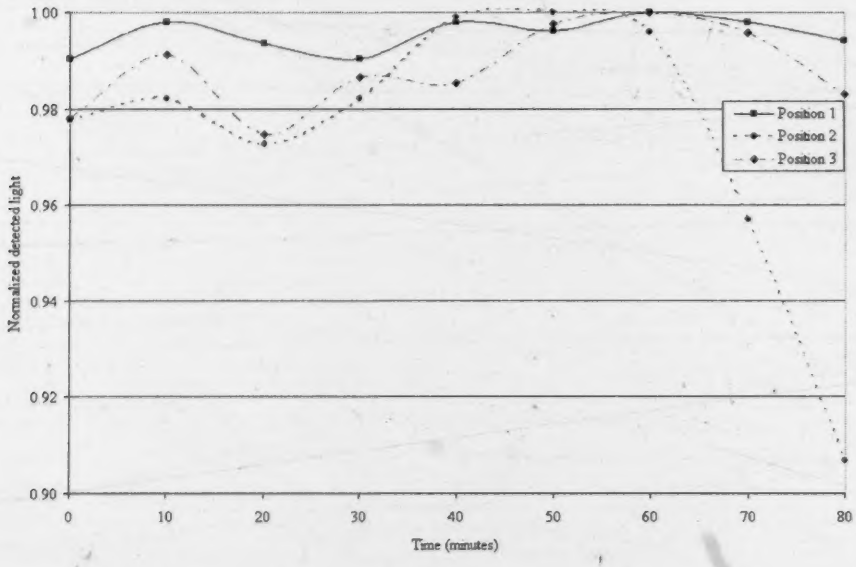

Figure 5.12: Changes in tissue transmissivity during treatment of purpose-bred beagle.

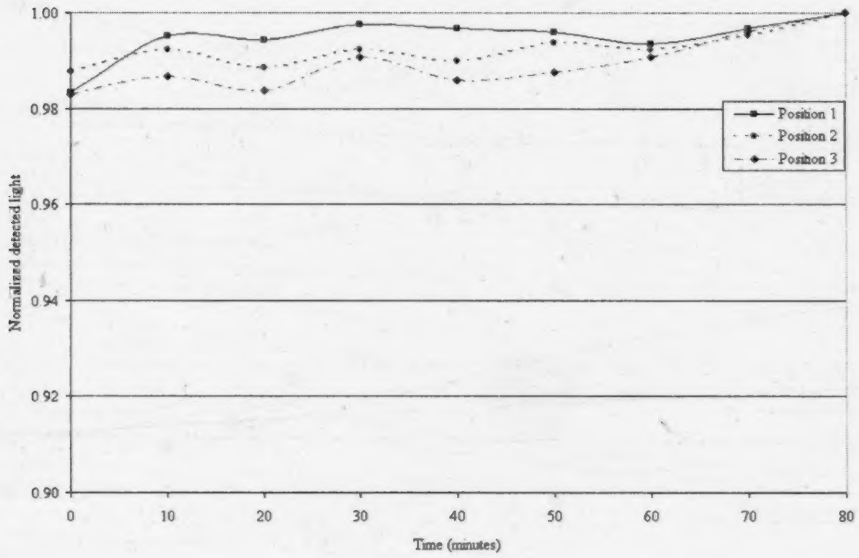

Chapter 6

PDT Dose: Quantifying Drug and Oxygen

The emphasis thus far has been to determine the photophysical light dose delivered to tissue. Most light delivery protocols are based on a 3 step process: administer photosensitizer, wait a drug-light interval to allow maximum accumulation of the photosensitizer, and then deliver prescribed dose [Wilson et al., 1997]. However, the photodynamic reaction is subject to many other variables that will affect treatment outcome. To predict the therapeutic effect being delivered to the target, the PDT dose must be considered. The PDT dose is a measure of the energy absorbed by the photosensitizer in a volume of tissue [MacDonald and Dougherty, 2001]. The future of photodynamic dosimetry rests in understanding the mechanisms by which the photodynamic dose is delivered to tissue. There are 2 basic photochemical reactions that produce a photodynamic kill effect—Type I and Type II reactions. In a Type I reaction, the photosensitizer accepts a photon, raising it to an excited state. The excited photosensitizer then reacts with its environment. In the Type II reaction, the photosensitizer accepts a photon, raising it to an excited state. There are now 2 possible reactions that the excited photosensitizer can undergo: it is re-

duced by oxygen, creating a reactive superoxide ion ($^1O_2$), or more predominantly, reacts with molecular oxygen to create highly reactive singlet oxygen ($^1O_2$). The short-lived singlet oxygen state has a lifetime of 10 ns and can diffuse about 0.1 μm. This produces a highly localized cell kill. Of the two possible reactions, Type II is observed to be the dominant PDT kill mechanism [Moan, 1986]. Type I reactions may dominate in a hypoxic environment and when the photosensitizer concentration is extremely high.

In either type of PDT reaction, the concentration of the photosensitizer will affect the reaction, and since Type II is considered dominant, the presence of oxygen will also affect the reaction. It was observed that the molecular oxygen concentration can rapidly plummet in the first few moments of PDT [Pogue et al., 2001]. Additionally, the PDT reaction may induce an occlusion of the microvasculature, limiting the transport of fresh oxygen into the environment. PDT reaction efficacy slows as the oxygen concentration falls [Chen et al., 2002]. In order to truly quantify the therapeutic effect delivered to the target, the light energy, oxygen dynamics and photosensitizer concentration must be known. This chapter considers the possible approaches to measuring the concentrations of photosensitizer and oxygen in order to quantify the PDT dose to tissue

6.1 The Photosensitizer

In the ideal photodynamic therapy session, the patient would be administered a photosensitizer which would be rapidly and exclusively accrued by malignant cells and following treatment, the photosensitizer would be rapidly eliminated, minimizing the photosensitive period for the patient. When the photosensitizer is activated by light, a lethal localized photochemical reaction would exclusively kill target malignant tissues. The theory and protocol of light delivery is relatively independent of

the photosensitizer; however, the choice of photosensitizer is a crucial constituent of PDT. Different photosensitizers have different optical properties and biodistributions and therefore different clinical applications. Different photosensitizers preferentially absorb light at different wavelengths and each has its unique tissue toxicities [Boyle and Dolphin, 1996].

Photosensitizers fall into 2 broad categories referred to as first and second generation photosensitizers. First generation photosensitizers include Hematoporphyrin derivative (HpD), Photofrin® and 5-aminolaevulinic acid (ALA, Levulan®). These photosensitizers are activated with 630 nm light, which penetrates poorly into most human tissues, with $\delta = 3 - 4$ mm. Second generation photosensitizers include Benzoporphyrin derivative monoacid ring A (BPD-MA, Visudyne®, Verteporfin®), meta-tetrahydroxyphenylchlorin (mTHPC, Foscan®), and Aluminum Phthalocyanine (AlPc). These photosensitizers are activated at longer wavelengths (690 nm for BPD-MA, 652 nm for mTHPC, and 685 nm for AlPc) andgenerally have higher yields of singlet oxygen, thus rendering a more potent photodynamic effect.

Assuming naively for the moment that tissue oxygen levels remain constant over the course of PDT, the radius of necrosis has been expressed by Jacques [1992] as

$$r_{nec} = \delta \ln[\frac{b\Phi\sigma_{a_{dye}}\phi t k}{P_{th}}], \tag{6.1}$$

where

δ – penetration depth [mm];

Φ – the quantum efficiency, a ratio to produce a toxic product rather than heat or fluorescence;

$\sigma_{a_{dye}}$ – absorption coefficient of photosensitizer in tissue, which depends on the concentration of the photosensitizer [mm^{-1}], determined by using Eq(2.18);

ϕ – the irradiance (fluence rate) [W mm^{-2}];

t – time [s];

k – accumulation constant such that $k = 3 + 5.1e^{-8\sigma_a\delta}$;

P_{th} – threshold toxic product [photons mm^{-3}]; and

b – constant converting [J mm^{-3}] to [mol mm^{-3}], such that $b = 1/N_A hc$, where N_A is Avagadro's number, h is Planks constant, and c represents the speed of light.

Equation 6.1 requires many parameters to be known in order to provide the radius of necrosis; however, using a cylindrical diffusing fibre or an isotropic point source, most of these parameters may be determined specifically for a particular photosensitizer and tissue or can be calculated using the P3 Approximation or Diffusion Theory. Essentially, only $\sigma_{a_{dye}}$ remains unknown, which depends on the photosensitizer concentration in the target. Since the absorption is suspected to rise over the course of treatment, the fluence will fall. The concentration of the photosensitizer will drop over the course of treatment, due to photobleaching and/or clearance from tissues. Therefore, Eq(6.1) represents the maximum kill radius. However, it provides a good first order approximation of the relationships between quantitative photodosimetry elements, time and tissue necrosis.

Accumulation of the photosensitizer over the body is not uniform, with some organs accruing much higher levels of photosensitizer than others [Boyle and Dolphin, 1996]. However, determination of photosensitizer concentrations *in vivo* is an unresolved topic in PDT [Lee et al., 2001]. Presently, methods of quantifying photosensitizer concentrations in PDT include chemical extraction and fluorescence. Photosensitizer concentrations are rarely quantified clinically because obtaining biopsies for chemical extraction are labor intensive, invasive, and occasionally impossible in practice [Cheung et al., 2003]. Since almost all photosensitizers exhibit some degree of fluorescent activity, fluorescence is a feasible method of non-invasive indirect drug quantification [Panjehpour et al., 1993]. Fluorescence potentially offers the following advantages: it provides rapid, direct and accurate measurements; it

can sample the same site repeatedly and non-destructively; and fibreoptic measurement facilitates endoscopic access to internal organs [Lee et al., 2001]. However, integrating fluorescence as a clinical monitoring tool is not immediately possible. One must study the physical and biological properties of the excitation/emission laser light on the target tissue, and the response of the fluorimeter to a large number of data points under different temporal and pharmacokinetic situations [Cheung et al., 2003]. Because photodynamic therapy is a dynamic process that changes the photochemistry of the medium, the detected fluorescence will be affected by the changing absorption of the medium and by the variation of the photosensitizer concentration during treatment. Thus, the fluorimeter must be calibrated specifically to detect the expected photosensitizer concentration in the target tissue in order to generate accurate results. The results reported by Lee et al. [2001] reassuringly indicate that *in situ* fluorescence measurements can accurately recover a photosensitizer's concentration, but only after appropriate calibration.

To determine the feasibility of integrating optical drug detection into the delivery system, a fibreoptic spectrometer was examined. The photosensitizer must be detectable at biologically pertinent concentrations. Two photosensitizer were studied—BPD-MA (dissolved in methanol) and QLT-0074 (BPD-DEA – liposomal formulation). Both are benzoporphyrin derivatives, and have similar fluorescence properties. The dosage of either drug for treatment of the R3327-H and -AT tumours is 1.5 mg/kg. Since the average male rat weighs 500 g, 0.75 mg of BPD-MA was dissolved 2mg/mL in distilled water, assuming total body distribution of the photosensitizer. The photosensitizer was then diluted to 10 mL in distilled water. A 500 mL tissue phantom consisting of 6% Intralipid (Kabi-Pharmicia) and 94% distilled water was prepared. This phantom has optical properties close to that of prostate tissue, with approximately the same relative drug to mass distribution in the Intralipid solution as an adult male rat.

A diode laser built from OEM components, operating at 532nm, was coupled to the flat-cleaved delivery fibre.[1] The output power of the delivery fibre was determined to be 7 mW. The delivery fibre was attached to the detection fibre, which was connected to an Ocean Optics S2000 spectrometer. The fluorescence was quantified via Ocean Optics software (OOIBase32) using arbitrary units, at an emission wavelength of 698 nm. The phantom was placed on a mixing machine and the paired fibre optics were introduced directly into the phantom. The source and detector fibres were taped together to ensure that a maximum signal was returned. Photosensitizer was added in 1 mL increments and the resultant fluorescence was recorded after each addition.

6.1.1 Results

The fluorescence emission of the photosensitizer was easily detected at the concentrations used. At the concentrations examined, the fluorescence seems linearly dependent upon the concentration, as shown in Figure 6.1. However, there is admittedly significant error in the measurements, most likely caused by fluctuations in the diode laser. It was necessary to mix the solution between measurements, and some fluctuation could therefore be attributed to physical displacement of the fibres. Regardless, Figure 6.1 shows that fluorescence drug detection is plausible. For purposes of quantification, a different light source would certainly be required because the present light source was unstable and a higher fluorescent signal could be achieved using a shorter wavelength.

[1]Diode lasers operating at 532 nm are widely and inexpensively available. A diode laser is preferred because it easily integrates into the light delivery system.

Figure 6.1: Examination of fluorescence as a function of concentration.

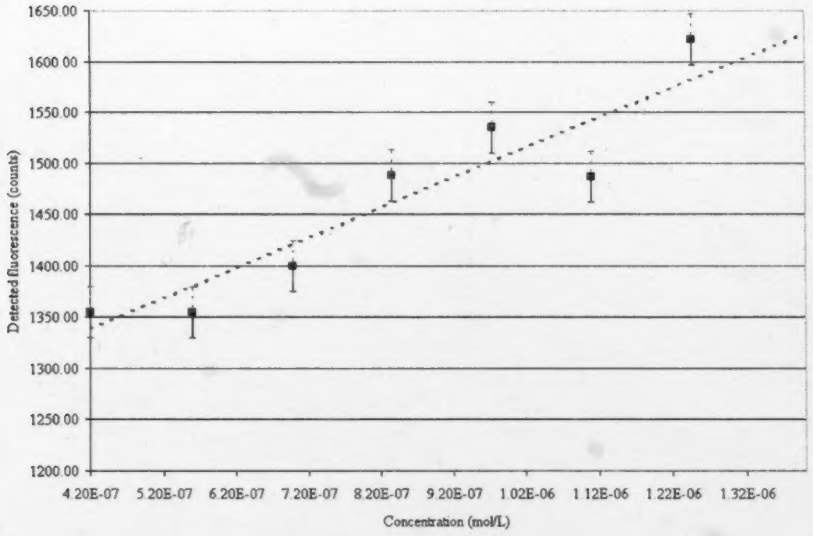

(a) fluorescence from QLT-0074 (liposomal formulation) measured at 690nm. Error bars indicate observed fluctuation in fluorescence

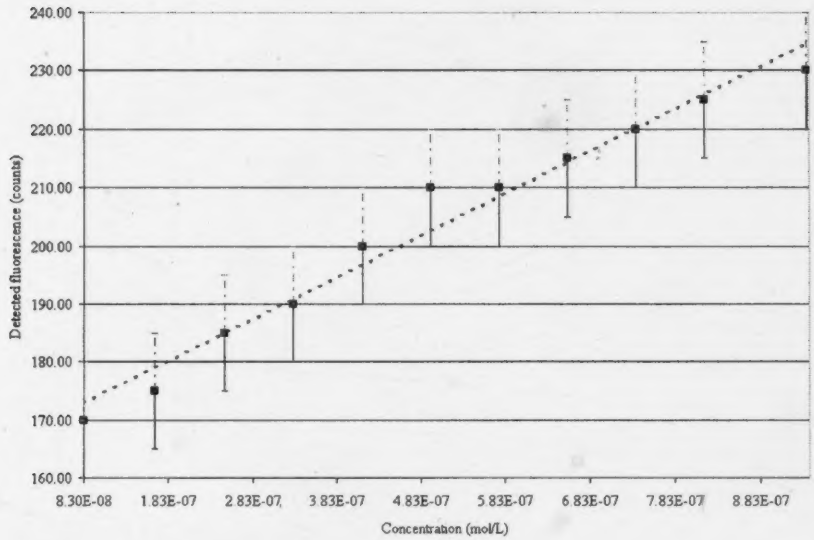

(b) Fluorescence from BPD-MA (dissolved in methanol) measured at 690 nm. Error bars indicate observed fluctuation in fluorescence.

6.1.2 Implications

There is apparently a linear relationship between the concentration and measured fluorescence. The fact that there is a discernible trend does lend some confidence in using fluorescence to quantify drug concentration. Potentially, through monitoring drug availability and its distribution around the gland, one could gain insight into the progress of the PDT reaction. With the knowledge of how photosensitizer is distributed around the target, one could adjust the light dose to ensure that all portions receive a lethal drug/light combination.

In vivo fluorescence measurements are complicated by absorption increases during PDT, making it difficult to implement a standard curve to detect photosensitizer concentration. Although the curves in Figure 6.1 appear linear, fluorescence is not linear for all concentrations of photosensitizer [Lee et al., 2001]. However, there is still merit examining the fluorescence, if only to detect the presence of the photosensitizer — such a tool would have been of great utility to determine the availability of photosensitizer in treating the purpose-bred beagle. In future studies, the fluorescence measurements (and their changes over the course of PDT) should be compared to the efficacy of the PDT session as another method of quantifying the photodynamic dose delivered to tissue.

Fluorescence seems to provide a feasible approach to indirectly determining tissue drug concentration but it may also present some downfalls. ALA provides an efficient fluorescent return but is a relatively poor photosensitizer. Compared to ALA, BPD-MA is a very potent photosensitizer but exhibits poor fluorescent properties. However, at drug concentrations used to treat rat flank tumours, BPD-MA should be detectable. Most photosensitizers have different absorption profiles, so the laser system used for one photosensitizer may not work for a different drug.

Drug detection would be an integral aspect of PDT. An optical method of deter-

mining drug tissue concentration could be easily integrated into the delivery system detailed in §5. An example of this system is shown in Figure 6.2.

Figure 6.2: Schematic of delivery system with fluorescence drug detection.

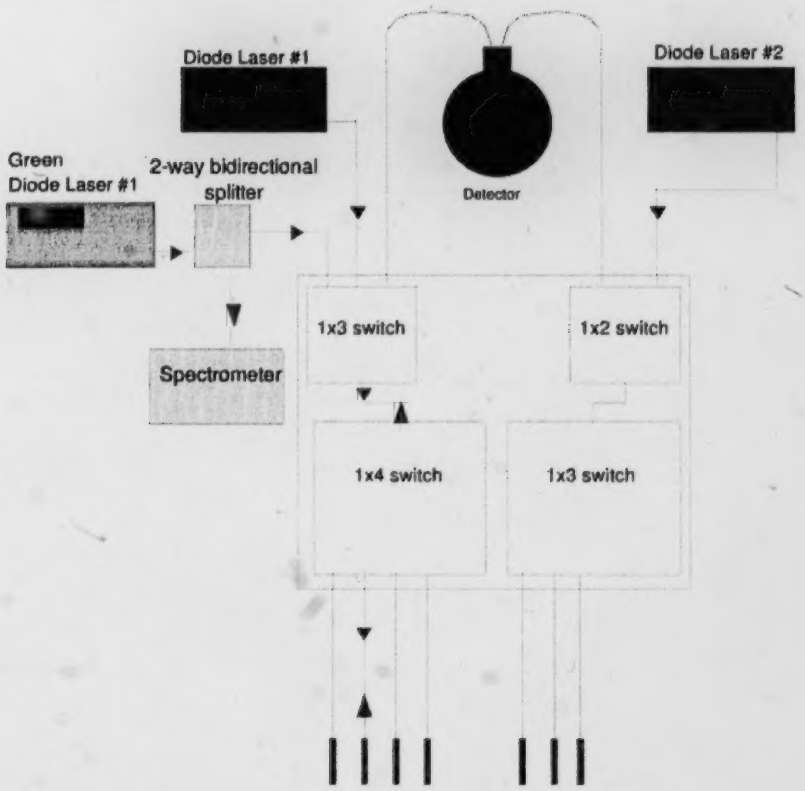

It is problematic that the excitation source and detecting fibre must share a channel due to the losses in a 50/50 splitter. Shorter wavelengths are strongly attenuated ($\delta_{532nm} \approx 1$ mm) by tissue. Thus, there would be very little observed fluorescence with the typical interfibre spacing of 8-10 mm. The spectrometer is capable of filtering out the unwanted excitation wavelengths. An external method using non-integrated hardware for fluorescence drug detection could be used. It would be used in a manner similar to radiance, preceding treatment. This would only al-

low the initial concentration to be determined. Photosensitizer concentration will drop during PDT; therefore, knowledge of the photosensitizer concentration would permit a margin of safety to be accurately established.

6.2 Oxygen and the Photodynamic Dose.

In the photodynamic reaction, cellular oxygen is converted to highly reactive singlet oxygen. Without a measurable level of oxygen, there is no observed photodynamic effect [Henderson and Dougherty, 1992].

Eq(6.1) does not account for the consumption of oxygen during PDT. As PDT consumes oxygen, the photodynamic reaction slows.

Monitoring tissue oxygen during PDT has thus far proven difficult. Monitoring tissue oxygen for PDT has been achieved by using oxygen sensitive electrodes [Pogue et al., 2001], fluorescent quenching-based optical probes Young et al. [1996], hypoxia markers [Moore et al., 1993] or non-invasive real-time imaging techniques. Pogue et al. [2001] showed that oxygen levels fell during PDT but partially recovered if permitted a dark time. Fractionating the light delivery, thereby allowing the target (or areas of a large target) to go through a dark cycle, permitted tissue oxygen to replenish, greatly increasing the efficacy of PDT [Muller et al., 1998]. It is unfortunately recognized that fractionating light delivery only facilitates oxygen transfer to perfused areas such that areas of the tumour that were hypoxic previous to PDT will not gain therapeutic benefit from light fractionation. Chen et al. [2002] described the treatment of a murine model under hyperbaric oxygen during PDT. The hyperbaric oxygen facilitates increased photodynamic effect to hypoxic/anoxic than under normabaric oxygen. Unfortunately, the administration of hyperbaric oxygen to a human patient in a clinical environment is difficult, while turning the

light source off and on is technologically simple. Even under hyperbaric conditions, oxygen was still depleted during PDT. Therefore, a combination of hyperbaric oxygen and light fractionation is likely to provide the ultimate therapeutic benefit.

There is a strong indication that the change in the optical parameters in the medium is partially due to the conversion of oxyhemoglobin to deoxyhemoglobin. Monitoring the relative concentration of HbO_2 and Hb is achievable using pulse oximetry. Pulse oximetry monitors the absorption of hemoglobin species and 650 nm and 805 nm. The optical pulse oximetry system can potentially be integrated into the light delivery system. A potential configuration is shown in Figure 6.3.

Figure 6.3: Integration of a pulse oximetry based system into the computer controlled light delivery system.

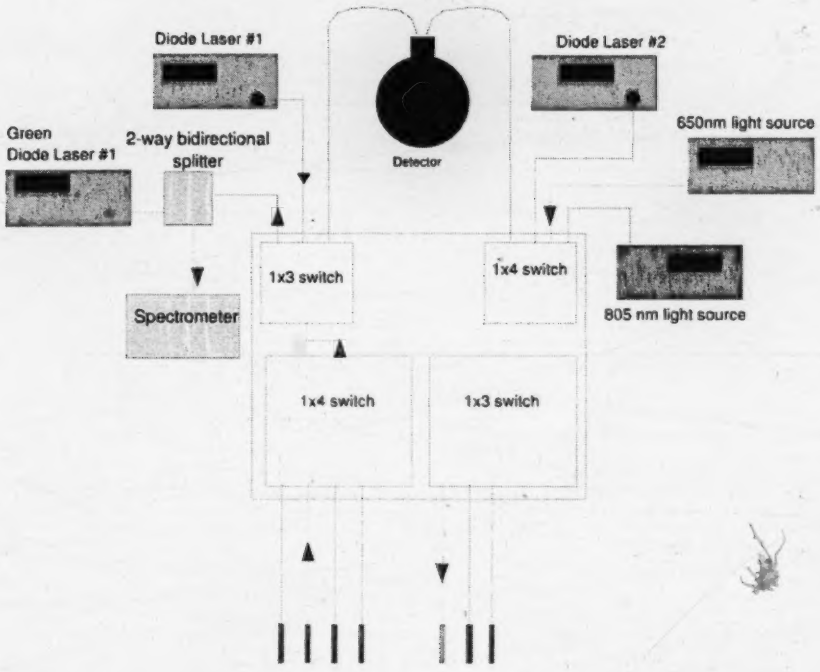

At this point, using pulse oximetry in PDT is speculative. The clinical application of pulse oximetry is used for measuring the relative ratio of Hb to HbO_2 in arterial

blood. It is uncertain that quantifying the the ratio of Hb to HbO_2 accurately indicate the availability of oxygen for the photodynamic reaction. As well, one would have to consider the absorption effects of the photosensitizer at 650 nm and 805 nm compared to those of HbO_2 and Hb. But with so many factors indicating that the HbO_2 and Hb being integral in determining tissue optics, it is worth investigating. As well, integration of pulse oximetry into the delivery system in Chapter 5 is likely inexpensively possible since the hardware for pulse oximetry is readily available.

Some simplistic mathematical models exist to determine the tissue oxygen concentration. A simple model was proposed by MacDonald and Dougherty [2001], such that

$$\frac{d[^1O_2]}{dt} = -\frac{EC\phi}{E_\Phi}\Phi = k[^3O_2], \tag{6.2}$$

where

E_Φ – energy per unit volume that must be absorbed to create oxygen;

E – molar extinction coefficient of $^1O_2$;

C – concentration of photosensitizer;

ϕ – fluence [W mm^{-2}]; and

Φ – quantum efficiency of converting photosensitizer to singlet oxygen (unitless).

k – rate constant for the conversion of $^3O_2$ to $^1O_2$

Notice that Φ occurs in both Eq(6.2) and Eq(6.1). Using Eq(2.18) in Eq(6.1) and then rearranging for Φ, one obtains

$$\Phi = \frac{P_{th}}{b\phi t k E_{dye} C_{dye} \ln 10} e^{r_{nec}/\delta},$$

Figure 6.4: A plot of Eq(6.5) ($\alpha = 0.1$), illustrating the temporal change in oxygen concentration.

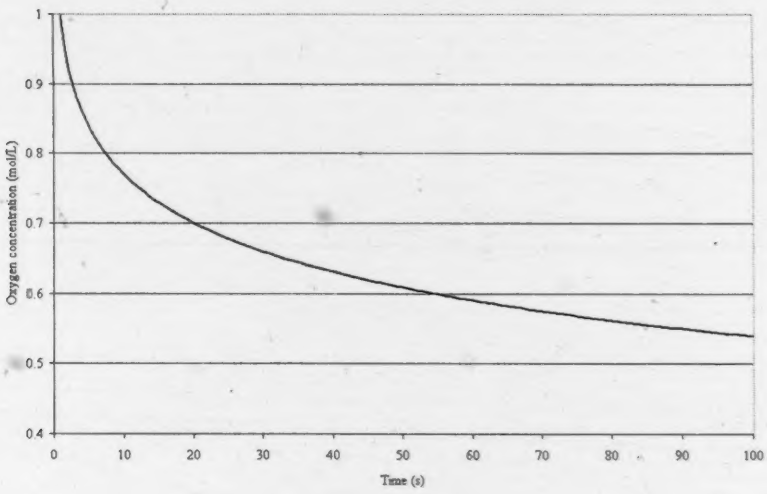

which can be inserted into Eq(6.2) to obtain

$$\frac{d[^1O_2]}{dt} = -\frac{E_{O_2}}{E_{dye}}\frac{P_{th}}{E_\Phi}\frac{e^{r_{nec}/\delta}}{bk\ln 10}t^{-1}. \tag{6.3}$$

Eq(6.3) is easily soluble, to finally give

$$[^1O_2] = [^1O_2]_{t=0} - \frac{E_{O_2}}{E_{dye}}\frac{P_{th}}{E_\Phi}\frac{e^{r_{nec}/\delta}}{bk\ln 10}\ln t, \tag{6.4}$$

where $[O_2]_{t=0}$ is the initial concentration of oxygen. To examine the behavior of the Eq(6.4), let us assume that $[^1O_2]_{t=0} = 1$ and $\frac{E_{O_2}}{E_{dye}}\frac{P_{th}}{E_\Phi}\frac{e^{r_{nec}/\delta}}{bk\ln 10} = \alpha$; therefore,

$$[^1O_2] = 1 - \alpha\ln t. \tag{6.5}$$

Eq.(6.5) is a simple equation, especially considering that α is comprised mostly of constants. The plot of Eq(6.5) is shown in Figure 6.4.

Using $\alpha = 0.052$, the time dependent plot of Eq(6.5) is compared against the relative

Figure 6.5: Comparison of Eq(6.5) (α = 0.052) with the relative changes in light transmissivity in an -H tumour.

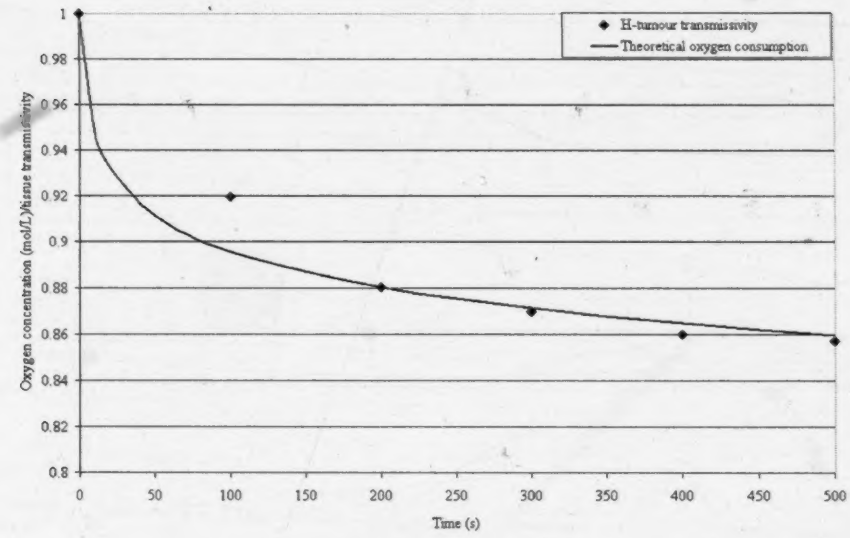

changes in tissue transmissivity of -H tumour, position 2 in Figure 5.9 to produce Figure 6.5.

The assumptions made to obtain Eq(6.5) over-simplifies the physics of this problem, but there is still an undeniable correlation between the simplified oxygen consumption and the decrease in transmissivity caused from the PDT of the -H tumour. By simply changing α, Eq(6.5) can be fit to all the curves in Figure 5.9. This simplistic mathematical representation holds some insight to the depletion of oxygen. The changes in tissue optical parameters have been correlated to the conversion of HbO_2 to Hb. The agreement in Figure 6.5 indicate that this is probably true. It is understood, however, that both Eq(6.1) and Eq(6.4) are oversimplified, with α (or rather the factors in α) being a function of time.

Regardless, the integration of a method to monitor the relative concentrations of HbO_2 and Hb, at the very least for research purposes, would confirm whether or not the changes in optical parameters are caused by the hemoglobin conversions.

Knowledge of the oxygen concentration would also potentially indicate the end point to the efficacy of PDT session. Perhaps, when the tissue transmissivity no longer changes, the oxygen has been consumed (or the photosensitizer has been depleted) and there is no longer any therapeutic effect being delivered by PDT. More research on this matter is required.

Chapter 7

Conclusion

PDT's potential has been somewhat limited because its implementation into a clinical environment requires the unified knowledge of many disciplines in order to successfully apply its benefits. Early stage PCa is treatable with conventional modalities, but late stage PCa tends to be resistant to the conventionally applied hormone and radiation therapy. Surgical resection of the prostate is an effective treatment but this invasive procedure is discouraged in elderly patients. However, the probability of acquiring PCa increases with age; therefore, an aggressive, minimally invasive procedure would be welcome for such instances of PCa.

Our research indicates that PDT can cure very large tumour masses with negligible trauma compared to surgery. Relatively speaking, lasers, fibre optics, photosensitizer, fluorimeters and computers are new technology, and in many cases, newer than PDT itself (especially in regards to laser and computer availability). With the increasing availability of previously expensive and specialized technology, the stage has been set for the emergence of PDT into a clinical environment for the interstitial treatment of PCa. The novel concepts of the P3 Approximation for tissue characterization and the Huygens-Diffusion model for light delivery explained in this thesis

provide a solid basis for reliably administering light for PDT. Using these mathematical theories and the now commercially available high-powered laser diodes and fibreoptic switching systems, the described prototype delivery system is capable of delivering a lethal amount of light to prostatic tumours. The photodosimetry detailed in this thesis is sophisticated and elegant but is, regrettably, still not fully comprehensive. The tissues surrounding the prostate will have an effect on light transmission. The prostate itself, however, has been determined to be fairly homogeneous, with any inhomogeneities in the bulk of the tissue being virtually insignificant for determining fluence delivered. Despite these inhomogeneities, a lethal dose of light can still be delivered to gland, and and the distribution tailored within a couple of millimeters of the prostatic periphery. Further accuracy will be attainable by simply characterizing the surrounding tissues.

The future of PDT dosimetry should be focussed around determination of the PDT dose which would incorporate the 3 photodynamic elements (light, photosensitizer and oxygen) to the cell kill effect. The quantification of photosensitizer and oxygen concentrations are two unresolved topics in PDT dosimetry. A real-time method of monitoring these two photodynamic elements is necessary to quantify the efficacy of a photodynamic reaction. It would be ideal to have all-optical methods to quantify photosensitizer and oxygen concentrations since optical methods could be readily integrated into the light delivery system described in Chapter 5. Fluorescence is a promising option for determining photosensitizer concentration. However, a generalized approach is not possible since fluorescence-photosensitizer concentration relationships must be created for each tissue at the relevant localized concentrations. Careful and diligent experimentation should make this possible. Optical detection of molecular oxygen is difficult. There are, however, some indications that simply monitoring the changes in tissue transmissivity would indicate the change in oxygen availability, perhaps due to the PDT-induced change of oxyhemoglobin to

deoxyhemoglobin. Monitoring these quantities could give insight into both changes in tissue transmissivity and oxygen availability. The relative concentrations of oxyhemoglobin and deoxyhemoglobin are clinically determined using pulse oximetry. It is possible that this optical method could be exploited and integrated into the light delivery system.

The application of PDT has classically been limited by the expensive, specialized technology needed to safely and reproducibly deliver the treatment. However, since 2001, compact, high powered laser diodes have been commercially available at a variety of wavelengths. With new facilities to detect and deliver light, PDT is poised to become a clinical application for a variety of illnesses, both benign and malignant. The concepts detailed in this thesis should aid in overcoming many of the limitations that have limited clinical implementation of PDT. The P3 Approximation and the Huygens-Diffusion Model are generalized, analytical models with potential to many applications of PDT. In its present form, the P3 Approximation can be used to characterize large tissue volumes. The Huygens-Diffusion Model may be applied to any linearly continuous source, even those of irregular shape, such as the flexible diffusers used to treat lung cancer.

The light delivery system described in this thesis was designed to treat prostatic carcinoma with a second generation photosensitizer. By changing the lasers and delivery fibres (or adding any number of optical devices for other uses such as determining photosensitizer concentration), the system may be used for virtually any treatment geometry, with any photosensitizer. In particular, this PDT system has the potential to treat massive inoperable tumours—late stage prostate cancer being a primary example. Furthermore, fibreoptics, and therefore PDT, can access disease close to anatomical critical strucures, such as head and neck cancers, unsafe for radiation therapy and surgery. Present treatment modalities offer a reasonable amount of success in treating cancer; however, the incidence of cancer continues to

rise and so does the need to find alternative treatments. PDT has the potential to be a viable treatment alternative for this merciless disease.

Bibliography

M R Arnfield. *Optical dosimetry of prostate tumours*. PhD thesis, University of Alberta, 1989.

M R Arnfield, J D Chapman, J Tulip, and M C Fenning. Optical properties of experimental prostate tumours in-vivo. *Photochem. And Photobiol.*, 57:306–11, 1993.

M R Arnfield, R P Mathew, J Tulip, and M S McPhee. Optical dosimetry for interstitial photodynamic therapy. *Med Phys.*, 12:602–8, 1989.

M R Arnfield, R P Mathew, J Tulip, and M S McPhee. Analysis of tissue optical coefficients using an approximation equation valid for comparable absorption and scattering. *Phys Med Biol*, 37:1219–30, 1992.

F W Attix. *Introduction to Radiological Physics and Radiation Dosimetry*. John Wiley Sons, New York, New York, 1986.

A M Ballangrud, P J Wilson, K M Brown, G G Miller, RB Moore, M S McPhee, and J Tulip. Anisotropy of radiance in tissue phantoms and Dunning r3327 rat tumors: Radiance measurements with flat cleaved fibre probes. *Lasers Surg. Med*, 19:471–7, 1996.

F P Bolin, L E Preuss, and R C Taylor. Optimization of photodynamic therapy light dose distribution and treatment volume by multi-fibre insertions. *Photochem. Photobiol.*, 46(5):609–617, 1987.

R W Boyle and D Dolphin. Structure and biodistribution relationships of photodynamic photosensitizers. *Photochem. Photobiol*, 64(3):469–485, 1996.

J A S Carruth. Photodynamic therapy: The state of the art. *Las. Surg. Med*, 6: 404–407, 1986.

S Chandrasekhar. *Radiative Transfer*. Dover, New York, 1960.

Q Chen and F W Hetzell. Laser dosimetry studies in prostate. *Journal of Clinical Laser Medicine and Surgery*, 16:9–12, 1998.

Q Chen, Z Huang, H Chen, H Shapiro, J Beckers, and F W Hetzel. Improvement of tumour response by manipulation of tumour oxygenation during photodynamic therapy. *Photochem. Photobiol.*, 76(2):197–203, 2002.

Q Chen, B C Wilson, S D Shetty, M S Patterson, J C Cerny, and F W Hetzel. Changes in in-vivo optical properties and light distributions in normal canine prostate during photodynamic therapy. *Rad. Res.*, 147:86–91, 1997.

R Cheung, M Solonenko, T M Busch, and F Del Piero. Correlation of in vivo photosensitizer fluorescence and photodynamic-therapy induced depth of necrosis in a murine tumour. *J. Biomed. Opt.*, 8(2):248–252, April 2003.

B Davison. *Neutron Transport Theory*. Clarendon, Oxford, 1957.

D J Dickey, O Barajas, K M Brown, J Tulip, and RB Moore. Radiance modeling using the p3 approximation. *Phys. Med. Biol*, 43:3559–3570, 1998.

D J Dickey, K J Partridge, R B Moore, and J Tulip. Light dosimetry for multiple cylindrical diffusing sources for use in photodynamic therapy. *Phys Med Biol*, IN PRINT:IN PRINT, 2004.

D J Dickey, D C Rayner, R B Moore, and J Tulip. Light dosimetry using the p3-approximation. *Phys. Med. Biol*, 46(9):2359–2370, 2001.

D R Doiron, L O Svaasand, and A E Profio. Wavelength and dosimetry considerations in photoradiation therapy. *SPIE Lasers in Surgery and Medicine*, 357: 63–85, 1982.

T J Dougherty. Activated dyes as antitumour agents. *J. Nat. Cancer. Inst.*, 52: 1333–1336, 1974.

T J Dougherty, G B Grindey, R Fiel, K R Weishaupt, and D G Boyle. Photoradiation therapy. ii. cure of animal tumours with hematoporphyrin and light. *J. Nat. Canc. Inst*, 55(55):115 – 121, 1975.

J W Feather, P R King, I Driver, and J B Lawson. A method for the construction of disposable cylindrical diffusing fibre optics for use in photodynamic therapy. *Laser Med. Sci*, 4(229):229–235, 1989.

V H Fingar and B W Henderson. Drug and light dose dependence of photodynamic therapy: a study of tumour and normal tissue response. *Photochem. Photobiol.*, 46(5):837–841, 1987.

S T Flock, S L Jacques, B C Wilson, W M Star, and M J C van Gemert. Optical properties of intralipid: a phantom medium for light propogation studies. *Lasers Surg. Med*, 12(12):510–519, 1992.

S T Flock, B C Wilson, and M S Patterson. Total attenuation coefficients and scattering phase functions of tissues and phantom materials at 633 namometers. *Med. Phys.*, 14(5):835–41, 1986.

CC Grosjean. A high accuracy approximation for multiple scattering in infinite homogeneous media. *Nuovo Cimento*, 3:1263 –75, 1956.

Eugene Hecht. *Optics*. Addison Wesley, Don Mills Ontario, second edition, 1990.

B W Henderson and T J Dougherty. How does photodynamic therapy work? *Photochem. Photobiol.*, 55(1):145–157, 1992.

A Hsi, A Kapatkin, J Strandberg, T Zhu, T Vulcan, M Solonenko, C Rodriguez, J Chang, M Saunders, N Mason, and S Hahn. Photodynamic therapy in the canine prostate using motexafin lutetium. *Clinical Cancer Research*, 7:651–660, 2001.

A Ishimaru. *Wave propagation and scattering in random media, vol. I: single scattering and transport theory*. Academic, NewYork, 1978.

S L Jacques. Laser-tissue interaction: Photochemical, photothermal, and photomechanical. *Surgical Clinics North America*, 72(3):531–58, 1992.

J Jankun, A Zaim, M Jankun-Kelly, R W Keck, and S H Selman. Computer model for photodynamic therapy of the prostate. In R R Anderson, editor, *Lasers in Surgery: Advanced Characterization, Therapeutics and Systems X*, volume 3907, pages 222–226. SPIE, 2000.

A Jesionek and V H Tappeienner. Zur behandlung der hautcarcinome mit fluorescencenden stoffen. *Muench Med Wochschr*, 47:2042–2044, 1903.

T Johansson, M Thompson, M Stenberg, C Klinteberg, S Andersson-Engels, S Svanberg, and K Svanberg. Feasibiliy study of a system for combined light dosimetry and interstitial photodynamic treatment of massive tumours. *Ap. Opt.*, 41(7):1462–1468, 2002.

M Keijzer, W M Star, and P R M Storchi. Optical diffusion in layered media. *Appl. Optics*, 27:1820–1824, 1988.

C C Lee, B W Pouge, R R Strawbridge, K L Moodie, L R Bartholomew, G C Burke, and P J Hoopes. Comparison of photosensitizer (alpcs2) quantification techniques: In situe fluorescence microsampling versus tissue chemical extraction,. *Photochem. Photobiol.*, 74(3):453–460, 2001.

L K Lee, C Whitehurst, Q Chen, M L Pantelides, F W Hetzel, and J V Moore. Interstitial photodynamic therapy in the canine prostate. *Brit J. Urol*, 80:898–902, 1997.

L K Lee, C Whitehurst, M L Pantelides, and J V Moore. In situ comparison of 665 nm and 633 nm wavelength light penetration in the human prostate gland. *Photochem. Photobiol.*, 62(5):882–886, 1995.

L K Lee, C Whitehurst, M L Pantelides, and J V Moore. An interstitial light assembly for photodynamic therapy in prostatic carcinoma. *BJU International*, 84: 821–826, 1999.

L K Lee, C Whitehurst, M L Pantelides, D I Vernon, and J V Moore. Interstitial photodynamic therapy in the Dunning R3327-at6 prostatic carcinoma. *Las. Med. Sci.*, 11:155–161, 1996.

D A Levy, J Schwartz, M Ostermeyer, S L Jacques, and A C von Eschenbach. Transurethral in vivo optical properties of the human prostate gland. *Proc. of SPIE*, 2671:329–333, 1996.

L Lilge and B C Wilson. The accuracy of interstitial measurements of absolute light fluence rate in the determination of tissue optical properties. *Laser-Tissue Interaction IV SPIE*, 1882:291–304, 1993.

R L Lipson, J H Pratt, E J Baldes, and M B Dockerty. Hematoporphyrin derivative for detection of cervical cancer. *J. Nat. Canc. Inst*, 24:78– 84, 1964.

I J MacDonald and T J Dougherty. Basic principles of photodynamic therapy. *J Porphyrins and Phthalocynanines*, 5:105–129, 2001.

J F McNeil, D G Bostwick, R A Kindrachuk, E A Redwine, F S Freiha, and T A Stamey. Patterns of progression of prostate cancer. *Lancet*, 1:60, 1986.

J Moan. Properties for optimai PDT sensitizers. *J. Photochem. Photobiol.*, B5: 521–524, 1986.

R B Moore, J D Chapman, J R Mercer, R H Mannan, L I Wiebe, A J McEwan, and M S McPhee. Measurement of PDT-induced hypoxia in dunning prostate tumors by iodine-123-iodoazomycine arabisnoside. *J Nucl. Med.*, 34:405–411, 1993.

S Muller, H Walt, D Dobler-Girdziunaite, D Fiedler, and U Haller. Enhanced photodynamic effects using fractionated laser light. *J. Photochem. Photobiol. B*, 42: 67–70, 1998.

L H P Murrer, P A Marijnissen, and W M Star. Light distribution by linear diffusing sources for photodynamic therapy. *Phys Med Biol*, 41:951–961, 1996.

National Cancer Institute of Canada. *Canadian Cancer Statistics 2003*. Canadian Cancer Society, Toronto, April 2003.

M Panjehpour, R E Sneed, D L Frazier, M A Barnhill, S F O'Brian, W Barb, and B F Overholt. Quantification of phthalocyanine concentration in rat tissue using laser-induced fluorescence spectroscopy. *Lasers Surg. Med.*, 13:23–30, 1993.

B W Pogue, R D Braun, J L Lanzen, C Erickson, and M W Dewhirst. Analysis of the hetereogeneity of pO_2 dynamics during photodynamic therapy with verteporfin. *Photochem. Photobiol*, 74(5):700–706, 2001.

A Policard. Eitudes sure les aspects offerts par des tumeurs experimentales examinee a la lumiere woods. *Z. Biol.*, 91:1423–1424, 1924.

S A Prahl, M Keijze, S L Jacques, and A J Welch. A Monte Carlo model of light propagation in tissue. *SPIE Ins. Ser*, IS5:102–111, 1989.

O Raab. Uber die wirkung fluorescierender stoffe auf infusoriera. *Z Biol*, 39:524, 1900.

A M Richter, E Waterfield, A K Jain, B Allison, E D Sternberg, D Dolphin, and J G Levy. Photosensitizing potency of structural analogues of benzoporphyrin derivative (bpd) in a mouse tumour model. *BJ Cancer*, 63:87–93, 1991.

F Ronchese. The fluorescence of cancer under the wood light. *Oral Surg Oral Med Oral Path*, 7:967–971, 1954.

K K Sen and S J Wilson. *Radiative Transfer in Curved Media*. World Scientific, Singapore, 1990.

W M Star. Comparing the P3-Approximation with diffusion theory and the with monte carlo calculations of light propogation in a slab geometry. *SPIE Instrum. Ser.*, 5:146–54, 1989.

W M Star. *Optical Thermal Response of Laser Irradiated Tissue*, chapter Diffusion Theory of Light Transport, pages 131–205. Plenum, New York, 1997.

M L Talston and R I Jennrich. Dud a derivative-free algorithm for nonlinear least squares. *Technometrics*, 20(1):7–14, 1978.

H J van Stavaren, C J M Moes, J van Marle, S A Prahl, and M J C van Gemert. Light scattering in intralipid-10400-1100 nm. *Appl. Opt.*, 30:4507–14, 1991.

K R Weishaupt, C J Gomer, and T J Dougherty. Identification of singlet oxygen as the cytotoxic agent in photo-inactivation of a murine tumour. *Cancer Res.*, 36: 2326–2329, 1976.

A J Welch and M J C van Gemert, editors. *Optical thermal response of Laser-Irradiated tissue*. Plenum, New York, 1995.

C Whitehurst, M L Pantelides, J V Moore, P J C Brooman, and N J Blacklock. In vivo laser light distribution in human prostatic carcinoma. *J. Urol.*, 151:1411–15, 1994.

P A Wilkisch and F Jacka. *Porphyrin Localization and Treatment of Tumours*, chapter Studies of light propogation through tissue, pages 149–161. Alan R. Liss, New York, 1984.

B C Wilson and G Adam. A Monte Carlo model for the absorption and flux distributions of light in tissues. *Med. Phys.*, 10:824–830, 1983.

B C Wilson, M S Patterson, and S T Flock. Indirect versus direct techniques for the measurement of the optical properties of tissues. *Photochem. Photobiol.*, 46(5): 601–608, 1987.

B.C. Wilson, M.S. Patterson, and L. Lilge. Implicit and explicit dosimetry in photodynamic therapy: A new paradigm. *Laser Med. Sci.*, 12:182–199, 1997.

Z Xiao, Y Tamimi, K M Brown, J Tulip, and R B Moore. Interstitial photodynamic therapy in subcutaneously implanted urologic tumours in rats after intravenous administration of 5-aminolevulinic acid. *Urologic Oncology*, 7(3):125–32, 2002.

W K Young, B Vojnovic, and P Wardman. Comparison of tumour and normal oxygen tension in tumoursby time-resolved fluorescence. *Br. J. Cancer*, 74:S256–S269, 1996.

Appendix A

Mathematica Formulation of the P3-Approximation for an Isotropic Point Source

The code was produced using Mathematica 4.01 for Linux (Wolfram Research). For the mathematica code included, the following nomenclature is used:

s – scattering coefficient (σ_s)

a – absorption coefficient (σ_a)

t – total attenuation coefficient (σ_t)

e0 – initial power

The commands should be executed in the order that they are presented. The results for A_n and C_n are not presented because the results require multiple pages to display. However, the commands required to obtain these values are included.

```
In[1]:= planea = {{(t - s), -t, 0, 0}, {-t, 3 * (t - g * s), -2 * t, 0},
           {0, -2 * t, 5 * (t - s * g^2), -3 * t}, {0, 0, -3 * t, 7 * (t - s * g^3)}}
Out[1]= {{-s + t, -t, 0, 0}, {-t, 3 (-g s + t), -2 t, 0},
          {0, -2 t, 5 (-g^2 s + t), -3 t}, {0, 0, -3 t, 7 (-g^3 s + t)}}
In[2]:= coeffa = {A0, A1, A2, A3}
Out[2]= {A0, A1, A2, A3}
In[3]:= {}
Out[4]= particular = {e0 * s * Exp[-t * r]/(4 * π * r)^2,
           e0 * s * g * Exp[-t * r]/(4 * π * r)^2,
           e0 * s * g^2 * Exp[-t * r]/(4 * π * r)^2,
           e0 * s * g^3 * Exp[-t * r]/(4 * π * r)^2}
In[5]:= {e^(-r t) e0 s/(16 π^2 r^2), e^(-r t) e0 g s/(16 π^2 r^2), e^(-r t) e0 g^2 s/(16 π^2 r^2), e^(-r t) e0 g^3 s/(16 π^2 r^2)}
```

```
In[6]:= Solve[b00[a, s, t, g, r, μ] + b01[a, s, t, g, r, μ] * B1 == 0, B1] //
          InputForm
Out[6]= {{B1 -> (s - 4*π*t)/(4*μ*π)}}

In[7]:= Solve[
            b10[a, s, t, g, r, μ] +
              b11[a, s, t, g, r, μ] * B1[a, s, t, g, r, μ] +
              b12[a, s, t, g, r, μ] * B2 == 0, B2] //InputForm
Out[7]= {{B2 -> (-8*μ*π - 4*μ^2*π*r + 9*g*r*s^2 -
          9*g*r*s*t - 12*π*r*s*t + 12*π*r*t^2)/
          (8*μ*π*(-1 + μ*r))}}

In[8]:= Solve[b21[a, s, t, g, r, μ] * B1[a, s, t, g, r, μ] +
              b22[a, s, t, g, r, μ] * B2[a, s, t, g, r, μ] +
              b23[a, s, t, g, r, μ] * B3 == 0, B3] //InputForm
Out[8]= {{B3 -> (((2*μ + 6/r) * (-s + t))/μ -
          (5*((-5*g^2*s)/(4*π) + t)*
           (-μ + (3*(-s + t) * (-(g*s) + t))/μ))/(2*μ))/
          (3*μ - 6/r)}}

In[9]:= B0 := 1

In[10]:= B1[a_, s_, t_, g_, r_, mu_] := (s - 4*π*t)/(4*μ*π)

In[11]:= B2[a_, s_, t_, g_, r_, mu_] :=
           (-8*μ*π - 4*μ^2*π*r + 9*g*r*s^2 - 9*g*r*s*t -
             12*π*r*s*t + 12*π*r*t^2)/(8*μ*π*(-1 + μ*r))

In[12]:= B3[a_, s_, t_, g_, r_, mu_] :=
           (((2*μ + 6/r) * (-s + t))/μ -
             (5*((-5*g^2*s)/(4*π) + t)*
               (-μ + (3*(-s + t) * (-(g*s) + t))/μ))/(2*μ))/(3*μ - 6/r)


In[13]:= Limit[B1[a, s, t, g, r, μ], r → ∞]
Out[13]= (s - 4πt)/(4μπ)

In[14]:= Limit[B2[a, s, t, g, r, μ], r → ∞]
Out[14]= (-4μ^2π + 3(s - t)(3gs - 4πt))/(8μ^2π)

In[15]:= Limit[B3[a, s, t, g, r, μ], r → ∞]
Out[15]= 1/(24μ^3π) (75g^3s^2(s - t) - 60gπs(s - t)t -
           25g^2s(μ^2 + 3(s - t)t) + 4π(15(s - t)t^2 + μ^2(-4s + 9t)))
```

```
In[16]:= sigma0[a_, s_, t_, g_, r_] :=
          (-24 * π * r+
               Sqrt[2]*
                 Sqrt[
                   r^2 * (1440 * π^2 + 81 * g * r^2 * s^2+
                        196 * g^3 * r^2 * s^2 + 1225 * g^5 * r^2 * s^2-
                  220 * π * r^2 * s * t - 324 * g * π * r^2 * s * t-
                  700 * g^2 * π * r^2 * s * t-
                  1764 * g^3 * π * r^2 * s * t+
                  1440 * π^2 * r^2 * t^2-
                  Sqrt[
                    (g * (81 + 196 * g^2 + 1225 * g^4) * r^2 * s^2-
                          4 * (55 + 81 * g + 175 * g^2 + 441 * g^3) *
                            π * r^2 * s * t + 288 * π^2*
                             (4 + 5 * r^2 * t^2))^2-
                       108 * r^2 * (s - 4 * π * t) *
                         (3675 * g^6 * r^2 * s^3-
                            2940 * g^4 * π * r^2 * s^2 * t-
                            4900 * g^5 * π * r^2 * s^2 * t+
                            2800 * g^2 * π^2 * r^2 * s * t^2-
                            320 * π^3 * t * (20 + 7 * r^2 * t^2) +
                            48 * g * π^2 * s * (72 + 35 * r^2 * t^2) +
                            28 * g^3 * π * s * (-75 * r^2 * s * t+
                                 28 * π * (4 + 5 * r^2 * t^2)))]])]) /
     (24 * π * r^2)
```

```
In[17]:= sigma1[a_, s_, t_, g_, r_] :=
          -(24 * π * r+
                Sqrt[2]*
                  Sqrt[
                    r^2 * (1440 * π^2 + 81 * g * r^2 * s^2+
                          196 * g^3 * r^2 * s^2 + 1225 * g^5 * r^2 * s^2-
                          220 * π * r^2 * s * t - 324 * g * π * r^2 * s * t-
                          700 * g^2 * π * r^2 * s * t-
                          1764 * g^3 * π * r^2 * s * t+
                          1440 * π^2 * r^2 * t^2-
                          Sqrt[
                            (g * (81 + 196 * g^2 + 1225 * g^4) * r^2*
                                    s^2 - 4 * (55 + 81 * g + 175 * g^2 + 441 * g^3)*
                                    π * r^2 * s * t + 288 * π^2*
                                    (4 + 5 * r^2 * t^2))^2-
                              108 * r^2 * (s - 4 * π * t)*
                                (3675 * g^6 * r^2 * s^3 - 2940 * g^4*
                                    π * r^2 * s^2 * t - 4900 * g^5 * π*
                                    r^2 * s^2 * t + 2800 * g^2 * π^2*
                                  r^2 * s * t^2 - 320 * π^3 * t*
                                  (20 + 7 * r^2 * t^2) + 48 * g * π^2*
                                  s * (72 + 35 * r^2 * t^2) + 28 * g^3*
                                  π * s * (-75 * r^2 * s * t+
                                     28 * π * (4 + 5 * r^2 * t^2)))])])/
     (24 * π * r^2)
```

```
In[18]:= sigma2[a_, s_, t_, g_, r_] :=
          (-24 * π * r+
               Sqrt[2]*
                 Sqrt[
                   r^2 * (1440 * π^2 + 81 * g * r^2 * s^2+
                        196 * g^3 * r^2 * s^2 + 1225 * g^5 * r^2 * s^2-
                        220 * π * r^2 * s * t - 324 * g * π * r^2 * s * t-
                        700 * g^2 * π * r^2 * s * t-
                        1764 * g^3 * π * r^2 * s * t+
                        1440 * π^2 * r^2 * t^2+
                        Sqrt[
                          (g * (81 + 196 * g^2 + 1225 * g^4) * r^2 * s^2-
                                4 * (55 + 81 * g + 175 * g^2 + 441 * g^3) *
                                  π * r^2 * s * t + 288 * π^2*
                                   (4 + 5 * r^2 * t^2))^2-
                             108 * r^2 * (s - 4 * π * t) *
                               (3675 * g^6 * r^2 * s^3-
                                  2940 * g^4 * π * r^2 * s^2 * t-
                                  4900 * g^5 * π * r^2 * s^2 * t+
                        2800 * g^2 * π^2 * r^2 * s * t^2-
                        320 * π^3 * t * (20 + 7 * r^2 * t^2) +
                        48 * g * π^2 * s * (72 + 35 * r^2 * t^2) +
                        28 * g^3 * π * s * (-75 * r^2 * s * t+
                             28 * π * (4 + 5 * r^2 * t^2)))]])]) /
     (24 * π * r^2)
```

```
In[19]:= sigma3[a_, s_, t_, g_, r_] :=
          -(24 * π * r+
                Sqrt[2]*
                  Sqrt[
                    r^2 * (1440 * π^2 + 81 * g * r^2 * s^2+
                          196 * g^3 * r^2 * s^2 + 1225 * g^5 * r^2 * s^2-
                          220 * π * r^2 * s * t - 324 * g * π * r^2 * s * t-
                          700 * g^2 * π * r^2 * s * t-
                          1764 * g^3 * π * r^2 * s * t+
                          1440 * π^2 * r^2 * t^2+
                          Sqrt[
                            (g * (81 + 196 * g^2 + 1225 * g^4) * r^2*
                                    s^2 - 4 * (55 + 81 * g + 175 * g^2 + 441 * g^3) *
                                    π * r^2 * s * t + 288 * π^2*
                                    (4 + 5 * r^2 * t^2))^2-
                              108 * r^2 * (s - 4 * π * t) *
                                (3675 * g^6 * r^2 * s^3 - 2940 * g^4*
                                    π * r^2 * s^2 * t - 4900 * g^5 * π*
                                    r^2 * s^2 * t + 2800 * g^2 * π^2*
                                r^2 * s * t^2 - 320 * π^3 * t*
                                (20 + 7 * r^2 * t^2) + 48 * g * π^2*
                                s * (72 + 35 * r^2 * t^2) + 28 * g^3*
                                π * s * (-75 * r^2 * s * t+
                                   28 * π * (4 + 5 * r^2 * t^2)))]])]) /
          (24 * π * r^2)
```

```
In[20]:= intmatrixb =
          {{dtemp0[1, B1[a, s, t, g, sigma0], B2[a, s, t, g, sigma0],
              B3[a, s, t, g, sigma0], sigma0, j],
            dtemp0[1, B1[a, s, t, g, sigma1], B2[a, s, t, g, sigma1],
              B3[a, s, t, g, sigma1], sigma1, j],
            dtemp0[1, B1[a, s, t, g, sigma2], B2[a, s, t, g, sigma2],
              B3[a, s, t, g, sigma2], sigma2, j],
            dtemp0[1, B1[a, s, t, g, sigma3], B2[a, s, t, g, sigma3],
              B3[a, s, t, g, sigma3], sigma3, j]},
           {dtemp1[1, B1[a, s, t, g, sigma0], B2[a, s, t, g, sigma0],
              B3[a, s, t, g, sigma0], sigma0, j],
            dtemp1[1, B1[a, s, t, g, sigma1], B2[a, s, t, g, sigma1],
              B3[a, s, t, g, sigma1], sigma1, j],
            dtemp1[1, B1[a, s, t, g, sigma2], B2[a, s, t, g, sigma2],
              B3[a, s, t, g, sigma2], sigma2, j],
            dtemp1[1, B1[a, s, t, g, sigma3], B2[a, s, t, g, sigma3],
              B3[a, s, t, g, sigma3], sigma3, j]},
           {dtemp2[1, B1[a, s, t, g, sigma0], B2[a, s, t, g, sigma0],
              B3[a, s, t, g, sigma0], sigma0, j],
            dtemp2[1, B1[a, s, t, g, sigma1], B2[a, s, t, g, sigma1],
              B3[a, s, t, g, sigma1], sigma1, j],
            dtemp2[1, B1[a, s, t, g, sigma2], B2[a, s, t, g, sigma2],
              B3[a, s, t, g, sigma2], sigma2, j],
            dtemp2[1, B1[a, s, t, g, sigma3], B2[a, s, t, g, sigma3],
              B3[a, s, t, g, sigma3], sigma3, j]},
           {dtemp3[1, B1[a, s, t, g, sigma0], B2[a, s, t, g, sigma0],
              B3[a, s, t, g, sigma0], sigma0, j],
            dtemp3[1, B1[a, s, t, g, sigma1], B2[a, s, t, g, sigma1],
              B3[a, s, t, g, sigma1], sigma1, j],
            dtemp3[1, B1[a, s, t, g, sigma2], B2[a, s, t, g, sigma2],
              B3[a, s, t, g, sigma2], sigma2, j],
            dtemp3[1, B1[a, s, t, g, sigma3], B2[a, s, t, g, sigma3],
              B3[a, s, t, g, sigma3], sigma3, j]}};

In[21]:= intcoeff = {C0, C1, C2, C3}
Out[21]= {C0, C1, C2, C3}

In[22]:= intparti =
          {-dtemp0[A0[a, s, t, g, j, e0], A1[a, s, t, g, j, e0],
              A2[a, s, t, g, j, e0], A3[a, s, t, g, j, e0], t, j],
           -dtemp1[A0[a, s, t, g, j, e0], A1[a, s, t, g, j, e0],
              A2[a, s, t, g, j, e0], A3[a, s, t, g, j, e0], t, j],
           -dtemp2[A0[a, s, t, g, k, e0], A1[a, s, t, g, k, e0],
              A2[a, s, t, g, k, e0], A3[a, s, t, g, k, e0], t, k],
           -dtemp3[A0[a, s, t, g, k, e0], A1[a, s, t, g, k, e0],
              A2[a, s, t, g, k, e0], A3[a, s, t, g, k, e0], t, k]};
```

```
In[23]:= Solve[intmatrixb.intcoeff == intparti, intcoeff]//InputForm

In[24]:= L[f0_, f1_, f2_, f3_, atten_, r_, m_] :=
          (f0 * LegendreP[0, m] + 3 * f1 * LegendreP[1, m] +
              5 * f2 * LegendreP[2, m] + 7 * f3 * LegendreP[3, m]) *
            Exp[sigma2 * r]

In[25]:= Integrate[L[f0, f1, f2, f3, atten, j, z] * LegendreP[1, z],
            {z, 0, 1}] +
          Integrate[L[f0, f1, f2, f3, atten, j, z] * LegendreP[1, z],
            {z, -0.7, 0}] +
          Integrate[
            L[f0, f1, f2, f3, atten, j, -(x^2/(10.2391)^2 + 0.7)] *
              LegendreP[1, x^2/(10.2391)^2 + 0.7] *
              (1 + 0.9758 * (Exp[-x] - 1)) * 2 * x/(10.2391)^2,
            {x, 5.6082, 0}]//InputForm
Out[25]= e^(j * sigma2) * (f0/2 + f1 + (5 * f2)/8) +
         e^(j * sigma2) * (-0.245 * f0 +
          0.343 * f1 + 0.162313 * f2 -
          0.612255 * f3) + 0.0190767*
         e^(j * sigma2) * (-2.1165 x 10^-7 *
          (1.4001 x 10^6 * f0 - 3.48622 x 10^6 *
           f1 + 3.67512 x 10^6 * f2 -
           1.24241 x 10^6 * f3) + 0.0000577071*
          (-12804.4 * f0 + 29475.3 * f1 -
          25620.4 * f2 + 5132.36 * f3))

In[26]:= dtemp0[f0_, f1_, f2_, f3_, atten_, j_] :=
          e^(j * sigma2) * (f0/2 + f1 + (5 * f2)/8) +
            e^(j * sigma2) *
              (-0.245 * f0 + 0.343 * f1 +
                 0.162313 * f2 - 0.612255 * f3) +
            0.0190767 * e^(j * sigma2) *
              (-2.1165 10^-7 *
                   (1.4001 10^6 * f0 - 3.48622 10^6 * f1 +
                      3.67512 10^6 * f2 - 1.24241 10^6 * f3) +
                0.0000577071*
                  (-12804.4 * f0 + 29475.3 * f1 -
                     25620.4 * f2 + 5132.36 * f3))
```

```
In[27]:= Integrate[L[f0, f1, f2, f3, atten, j, z] * LegendreP[3, z],
           {z, 0, 1}]+
         Integrate[L[f0, f1, f2, f3, atten, j, z] * LegendreP[3, z],
           {z, -0.7, 0}]+
         Integrate[
           L[f0, f1, f2, f3, atten, j, -(x^2/(10.2391)^2 + 0.7)]*
             LegendreP[3, x^2/(10.2391)^2 + 0.7]*
              (1 + 0.9758 * (Exp[-x] - 1)) * 2 * x/(10.2391)^2,
           {x, 5.6082, 0}] //InputForm
Out[27]= e^(j * sigma2) * (0.217438 * f0 -
          0.262395 * f1 - 0.235966 * f2 +
          0.550729 * f3) + e^(j * sigma2) *
          (-f0/8 + (5 * f2)/8 + f3) - 0.0286151*
          e^(j * sigma2) * (-4.37518 x 10^-9*
           (-33844.5 * f0 + 1.93411 x 10^7 * f1 -
           1.02121 x 10^8 * f2 + 3.55834 x 10^8*
            f3) + 1.60467 x 10^-11*
           (2.56442 x 10^9 * f0 - 4.68199 x 10^9 * f1 -
           6.11397 x 10^9 * f2 + 6.21849 x 10^10 * f3))

In[28]:= dtemp1[f0_, f1_, f2_, f3_, atten_, j_] :=
          e^(j * sigma2) *
              (0.217438 * f0 - 0.262395 * f1-
                  0.235966 * f2 + 0.550729 * f3)+
            e^(j * sigma2) * (-f0/8 + (5 * f2)/8 + f3)-
            0.0286151 * e^(j * sigma2) *
              (-4.37518 10^-9*
                   (-33844.5 * f0 + 1.93411 10^7 * f1-
                      1.02121 10^8 * f2 + 3.55834 10^8 * f3)+
                1.60467 10^-11*
                  (2.56442 10^9 * f0 - 4.68199 10^9 * f1-
                     6.11397 10^9 * f2 + 6.21849 10^10 * f3))

In[29]:= Integrate[L[f0, f1, f2, f3, atten, k, z] * LegendreP[1, z],
           {z, 0, 0.7}]-
         Integrate[
           L[f0, f1, f2, f3, atten, k, -(x^2/(10.2391)^2 + 0.7)]*
             LegendreP[1, x^2/(10.2391)^2 + 0.7]*
              (1 + 0.9758 * (Exp[-x] - 1)) * 2 * x/(10.2391)^2,
           {x, 0, 5.6082}]-
         Integrate[L[f0, f1, f2, f3, atten, k, z] * LegendreP[1, z],
           {z, -1, 0}]//InputForm
```

```
Out[29]= -(e^(k * sigma2) * (-f0/2 + f1 - (5 * f2)/8)) +
         e^(k * sigma2) * (0.245 * f0 +
          0.343 * f1 - 0.162313 * f2 -
          0.612255 * f3) - 0.0190767*
         e^(k * sigma2) * (2.1165 x 10^-7*
          (1.4001 x 10^6 * f0 - 3.48622 x 10^6*
           f1 + 3.67512 x 10^6 * f2 -
          1.24241 x 10^6 * f3) - 0.0000577071*
          (-12804.4 * f0 + 29475.3 * f1 -
          25620.4 * f2 + 5132.36 * f3))
```

```
In[30]:= dtemp2[f0_, f1_, f2_, f3_, atten_, k_] :=
          -(e^(k * sigma2) * (-f0/2 + f1 - (5 * f2)/8)) +
            e^(k * sigma2) *
              (0.245 * f0 + 0.343 * f1 -
                 0.162313 * f2 - 0.612255 * f3) -
            0.0190767 * e^(k * sigma2) *
              (2.1165 10^-7 *
                   (1.4001 10^6 * f0 - 3.48622 10^6 * f1 +
                      3.67512 10^6 * f2 - 1.24241 10^6 * f3) -
                 0.0000577071 *
                   (-12804.4 * f0 + 29475.3 * f1 -
                      25620.4 * f2 + 5132.36 * f3))
```

```
In[31]:= Integrate[L[f0, f1, f2, f3, atten, k, z] * LegendreP[3, z],
           {z, -1, 0}] -
         Integrate[L[f0, f1, f2, f3, atten, k, z] * LegendreP[3, z],
           {z, 0, 0.7}] -
         Integrate[
           L[f0, f1, f2, f3, atten, k, -(x^2/(10.2391)^2 + 0.7)] *
             LegendreP[3, x^2/(10.2391)^2 + 0.7] *
             (1 + 0.9758 * (Exp[-x] - 1)) * 2 * x/(10.2391)^2,
           {x, 0, 5.6082}]//InputForm
```

```
Out[31]= -(e^(k * sigma2) * (-0.217438 * f0 -
          0.262395 * f1 + 0.235966 * f2 +
          0.550729 * f3)) +
         e^(k * sigma2) * (f0/8 - (5 * f2)/8 + f3) +
         0.0286151 * e^(k * sigma2) *
          (4.37518 x 10^-9 * (-33844.5 * f0 +
           1.93411 x 10^7 * f1 - 1.02121 x 10^8 * f2 +
           3.55834 x 10^8 * f3) - 1.60467 x 10^-11 *
           (2.56442 x 10^9 * f0 - 4.68199 x 10^9 * f1 -
           6.11397 x 10^9 * f2 + 6.21849 x 10^10 * f3))
```

```
In[32]:= dtemp3[f0_, f1_, f2_, f3_, atten_, k_] :=
          -(e^(k * sigma2) *
                (-0.217438 * f0 - 0.262395 * f1 +
                   0.235966 * f2 + 0.550729 * f3)) +
            e^(k * sigma2) * (f0/8 - (5 * f2)/8 + f3) +
            0.0286151 * e^(k * sigma2) *
              (4.37518 10^-9 *
                   (-33844.5 * f0 + 1.93411 10^7 * f1 -
                      1.02121 10^8 * f2 + 3.55834 10^8 * f3) -
                1.60467 10^-11 *
                  (2.56442 10^9 * f0 - 4.68199 10^9 * f1 -
                     6.11397 10^9 * f2 + 6.21849 10^10 * f3))

In[33]:= rad[a_, s_, t_, g_, r_, j_, k_, e0_, m_] :=
           (1 * LegendreP[0, m] + 3 * LegendreP[1, m] + 5 * LegendreP[2, m] +
                7 * LegendreP[3, m]) *
             C0[a, s, t, g, j, k, e0, sigma0[a, s, t, g], sigma1[a, s, t, g],
               sigma2[a, s, t, g], sigma3[a, s, t, g]] *
             Exp[sigma0[a, s, t, g] * r] +
            (1 * B1[a, s, t, g, sigma0[a, s, t, g]] * LegendreP[0, m] +
                3 * B1[a, s, t, g, sigma1[a, s, t, g]] * LegendreP[1, m] +
                5 * B1[a, s, t, g, sigma2[a, s, t, g]] * LegendreP[2, m] +
                7 * B1[a, s, t, g, sigma3[a, s, t, g]] * LegendreP[3, m]) *
             C1[a, s, t, g, j, k, e0, sigma0[a, s, t, g], sigma1[a, s, t, g],
               sigma2[a, s, t, g], sigma3[a, s, t, g]] *
             Exp[sigma1[a, s, t, g] * r] +
            (1 * B2[a, s, t, g, sigma0[a, s, t, g]] * LegendreP[0, m] +
                3 * B2[a, s, t, g, sigma1[a, s, t, g]] * LegendreP[1, m] +
                5 * B2[a, s, t, g, sigma2[a, s, t, g]] * LegendreP[2, m] +
                7 * B2[a, s, t, g, sigma3[a, s, t, g]] * LegendreP[3, m]) *
             C2[a, s, t, g, j, k, e0, sigma0[a, s, t, g], sigma1[a, s, t, g],
               sigma2[a, s, t, g], sigma3[a, s, t, g]] *
             Exp[sigma2[a, s, t, g] * r] +
            (1 * B3[a, s, t, g, sigma0[a, s, t, g]] * LegendreP[0, m] +
                3 * B3[a, s, t, g, sigma1[a, s, t, g]] * LegendreP[1, m] +
                5 * B3[a, s, t, g, sigma2[a, s, t, g]] * LegendreP[2, m] +
                7 * B3[a, s, t, g, sigma3[a, s, t, g]] * LegendreP[3, m]) *
             C3[a, s, t, g, j, k, e0, sigma0[a, s, t, g], sigma1[a, s, t, g],
               sigma2[a, s, t, g], sigma3[a, s, t, g]] *
             Exp[sigma3[a, s, t, g] * r] +
            (1 * A0[a, s, t, g, r, e0] * LegendreP[0, m] +
                3 * A1[a, s, t, g, r, e0] * LegendreP[1, m] +
                5 * A2[a, s, t, g, r, e0] * LegendreP[2, m] +
                7 * A3[a, s, t, g, r, e0] * LegendreP[3, m]) * Exp[-t * r]
```

```
In[34]:= fluence[a_, s_, t_, g_, j_, k_, e0_, r_] :=
           (2 * A0[a, s, t, g, r, e0]) * e^(-r * t) +
            2 * e^(r * sigma0[a, s, t, g]) *
              C0[a, s, t, g, j, k, e0, sigma0[a, s, t, g], sigma1[a, s, t, g],
                sigma2[a, s, t, g], sigma3[a, s, t, g]] +
            2 * e^(r * sigma1[a, s, t, g]) *
              C1[a, s, t, g, j, k, e0, sigma0[a, s, t, g], sigma1[a, s, t, g],
                sigma2[a, s, t, g], sigma3[a, s, t, g]] +
            2 * e^(r * sigma2[a, s, t, g]) *
              C2[a, s, t, g, j, k, e0, sigma0[a, s, t, g], sigma1[a, s, t, g],
                sigma2[a, s, t, g], sigma3[a, s, t, g]] +
            2 * e^(r * sigma3[a, s, t, g]) *
              C3[a, s, t, g, j, k, e0, sigma0[a, s, t, g], sigma1[a, s, t, g],
                sigma2[a, s, t, g], sigma3[a, s, t, g]]

In[35]:= flu1[a_, s_, t_, g_, j_, k_, e0_, r_] :=
           (2 * A0[a, s, t, g, r, e0]) * e^(-r * t)

In[36]:= flu2[a_, s_, t_, g_, j_, k_, e0_, r_] :=
           2 * e^(r * sigma0[a, s, t, g]) *
             C0[a, s, t, g, j, k, e0, sigma0[a, s, t, g], sigma1[a, s, t, g],
               sigma2[a, s, t, g], sigma3[a, s, t, g]]

In[37]:= flu3[a_, s_, t_, g_, j_, k_, e0_, r_] :=
           2 * e^(r * sigma1[a, s, t, g]) *
             C1[a, s, t, g, j, k, e0, sigma0[a, s, t, g], sigma1[a, s, t, g],
               sigma2[a, s, t, g], sigma3[a, s, t, g]]

In[38]:= flu4[a_, s_, t_, g_, j_, k_, e0_, r_] :=
           2 * e^(r * sigma2[a, s, t, g]) *
             C2[a, s, t, g, j, k, e0, sigma0[a, s, t, g], sigma1[a, s, t, g],
               sigma2[a, s, t, g], sigma3[a, s, t, g]]

In[39]:= flu5[a_, s_, t_, g_, j_, k_, e0_, r_] :=
           2 * e^(r * sigma3[a, s, t, g]) *
             C3[a, s, t, g, j, k, e0, sigma0[a, s, t, g], sigma1[a, s, t, g],
               sigma2[a, s, t, g], sigma3[a, s, t, g]]
```

```
In[40]:= flu6[a_, s_, t_, g_, j_, k_, e0_, r_] :=
           (2 * A0[a, s, t, g, r, e0]) * e^(-r * t) +
            2 * e^(r * sigma0[a, s, t, g]) *
             C0[a, s, t, g, j, k, e0, sigma0[a, s, t, g], sigma1[a, s, t, g],
               sigma2[a, s, t, g], sigma3[a, s, t, g]] +
            2 * e^(r * sigma1[a, s, t, g]) *
             C1[a, s, t, g, j, k, e0, sigma0[a, s, t, g], sigma1[a, s, t, g],
               sigma2[a, s, t, g], sigma3[a, s, t, g]] +
            2 * e^(r * sigma2[a, s, t, g]) *
             C2[a, s, t, g, j, k, e0, sigma0[a, s, t, g], sigma1[a, s, t, g],
               sigma2[a, s, t, g], sigma3[a, s, t, g]]

In[41]:= flu7[a_, s_, t_, g_, j_, k_, e0_, r_] :=
           (2 * A0[a, s, t, g, r, e0]) * e^(-r * t) +
            2 * e^(r * sigma0[a, s, t, g]) *
             C0[a, s, t, g, j, k, e0, sigma0[a, s, t, g], sigma1[a, s, t, g],
               sigma2[a, s, t, g], sigma3[a, s, t, g]] +
            2 * e^(r * sigma1[a, s, t, g]) *
             C1[a, s, t, g, j, k, e0, sigma0[a, s, t, g], sigma1[a, s, t, g],
               sigma2[a, s, t, g], sigma3[a, s, t, g]]
```

Appendix B

Mathematica Formulation of a Huygens-Diffusion Theory

The code was produced using Mathematica 4.01 for Linux (Wolfram Research). For the mathematica code included, the following nomenclature is used:

s – scattering coefficient (σ_s)

a – absorption coefficient (σ_a)

t – total attenuation coefficient (σ_t)

e0 – initial power

```
In[42]:= (* global constants *)
         (*a = 0.07;
           s = 22;
           g = 0.88;
           ρ = 0.1;
           z = 1;
           e0 = 1;
         *)

In[43]:=
         (* diffusion functions *)

In[44]:= tot[a_, s_] := a + s;

         tr[a_, s_, g_] := a + (1 - g) * s;

         eff[a_, s_, g_] := Sqrt[3 * a * (a + (1 - g) * s)];
```

```
In[45]:= (*Point source function*)

         pntsrc[a_, s_, e0_, r_] := e0 * Exp[-(s + a) * r]/(4 * π * r^2)

In[46]:= (* (*Source function of array of spherical sources in
              a cylindrical geometry*)

           generalsource[r_, z_, rho_, t_] :=
            (r * z/(r + ρ)) * Exp[-(t * r/(r + ρ)) * Sqrt[(r + ρ)^2 + z^2]]/
              (((r + ρ)^2 + z^2)^(3/2))
             lowlim = N[tot[a, s] * r];
           uplim = N[tot[a, s] * r * Sqrt[1 + (z/(2 * (r + ρ)))^2]];
           cylsource = NIntegrate[Exp[-u]/u^2, {u, lowlim, uplim}];

           src[e0_, total_, radius_, cylrad_, cylsrc_] :=
            (e0 * tot/(2 * π)) * (radius/(radius + cylrad))^2 * cylsrc*)

In[47]:= (*the coefficient for particular term*)
         coeffgamma[a_, s_, g_, rho_, e0_] :=
          (Sqrt[3] * e^(ρ * (a + s)) * e0 * (a + a * g + s))/
           (8 * π * Sqrt[a * (a + s - g * s)])

In[48]:= (*below are the equations to execute, in order,
           to get the particular solution

             partsln[f_, t_, const_, r_] :=
            (const/2) *
             (Exp[f * r] * Gamma[0, (f + t) * r] - Exp[-f * r] * Gamma[0, (t - f) * r])

             partsln[eff[a, s, g], tot[a, s], coeffgamma[a, s, g, ρ, e0],
              r]

         Simplify[%] //InputForm*)

         (*particular solution*)

         partsln[a_, s_, g_, rho_, e0_, r_] :=
          (Sqrt[3] * e^(ρ * (a + s) - Sqrt[3] * r * Sqrt[a * (a + s - g * s)]) *
              e0 * (a + a * g + s) *
              (-ExpIntegralE[1, r * (a + s - Sqrt[3] * Sqrt[a * (a + s - g * s)])] +
                 e^(2 * Sqrt[3] * r * Sqrt[a * (a + s - g * s)]) *
                  ExpIntegralE[1,
                   r * (a + s + Sqrt[3] * Sqrt[a * (a + s - g * s)])]))/
           (16 * π * Sqrt[a * (a + s - g * s)])
```

```
In[49]:=
        (* homogeneous solution *)


        (* Coeffgamma is located below in the particular solution
             area above

             homocoeff[d_, f_, t_, g_, s_, e0_, rho_] :=
           ((3 * g * e0 * s) / e^(f * ρ) -
                 (2 * d * f * π * ρ^2 * ExpIntegralE[1, -(f * ρ) + ρ * t]) /
                  e^(2 * f * ρ) - 2 * d * f * π * ρ^2 *
                  ExpIntegralE[1, f * ρ + ρ * t]) / (-4 * π + 4 * f * π * ρ)

             homocoeff[coeffgamma[a, s, g, ρ, e0], eff[a, s, g],
              tot[a, s], g, s, e0, ρ] *)


        coeffhomo[a_, s_, g_, rho_, e0_] :=
          (3 * e0 * ((4 * g * s) / e^(Sqrt[3] * ρ * Sqrt[a * (a + s - g * s)]) -
                 (e^(ρ * (a + s - 2 * Sqrt[3] * Sqrt[a * (a + s - g * s)]))) *
                      π * ρ^2 * (a + a * g + s) *
                      ExpIntegralE[1,
                        ρ * (a + s - Sqrt[3] * Sqrt[a * (a + s - g * s)])]) / π -
                 (e^(ρ * (a + s)) * π * ρ^2 * (a + a * g + s) *
                      ExpIntegralE[1,
                        ρ * (a + s + Sqrt[3] * Sqrt[a * (a + s - g * s)])]) / π)) /
            (16 * π * (-1 + Sqrt[3] * ρ * Sqrt[a * (a + s - g * s)]))
```

```
In[50]:= (*Below is located the steps for obtaining the homogeneos
         solution

         homosln[k_, mueff_, r_] := 2*k*Exp[-mueff*r]/r

       homosln[coeffhom
                 o[a_, s_, g_, rho_, e0_], eff[a, s, g], r]

         Simplify[%] //InputForm*)

       homosln[a_, s_, g_, rho_, e0_, r_] :=
        (3*e0*((4*g*s)/e^(Sqrt[3]*ρ*Sqrt[a*(a+s-g*s)])-
              (e^(ρ*(a+s-2*Sqrt[3]*Sqrt[a*(a+s-g*s)]))*
                 π*ρ^2*(a+a*g+s)*
                 ExpIntegralE[1,
               ρ*(a+s-Sqrt[3]*Sqrt[a*(a+s-g*s)])])/π-
        (e^(ρ*(a+s))*π*ρ^2*(a+a*g+s)*
           ExpIntegralE[1,
            ρ*(a+s+Sqrt[3]*Sqrt[a*(a+s-g*s)])])/π))/
    (8*e^(Sqrt[3]*r*Sqrt[a*(a+s-g*s)])*π*r*
      (-1+Sqrt[3]*ρ*Sqrt[a*(a+s-g*s)]))
```

```
In[51]:= (* final Solution *)

         (* *)

         finalsln[a_, s_, g_, rho_, e0_, r_] :=
           (e0 * (4/(e^(r * (a + s)) * π * r^2) +
                  (Sqrt[3] *
                       e^(ρ * (a + s) - Sqrt[3] * r * Sqrt[a * (a + s - g * s)]) *
                       (a + a * g + s) *
                       (-ExpIntegralE[1,
                              r * (a + s - Sqrt[3] * Sqrt[a * (a + s - g * s)])] +
                          e^(2 * Sqrt[3] * r * Sqrt[a * (a + s - g * s)]) *
                            ExpIntegralE[1,
                              r * (a + s + Sqrt[3] * Sqrt[a * (a + s - g * s)])]))) /
                    (π * Sqrt[a * (a + s - g * s)]) +
                  (6 * ((4 * g * s) / e^(Sqrt[3] * ρ * Sqrt[a * (a + s - g * s)]) -
                        (e^(ρ * (a + s - 2 * Sqrt[3] * Sqrt[a * (a + s - g * s)])) *
                           π * ρ^2 * (a + a * g + s) *
                           ExpIntegralE[1, ρ *
                               (a + s - Sqrt[3] * Sqrt[a * (a + s - g * s)])]) / π -
                        (e^(ρ * (a + s)) * π * ρ^2 * (a + a * g + s) *
                           ExpIntegralE[1, ρ *
                        (a + s + Sqrt[3] * Sqrt[a * (a + s - g * s)])]) / π)) /
             (e^(Sqrt[3] * r * Sqrt[a * (a + s - g * s)]) * π * r *
                (-1 + Sqrt[3] * ρ * Sqrt[a * (a + s - g * s)])))) / 16

In[52]:=
Out[52]= {8.87044, 5.80107, 4.04932, 2.92357, 2.15612,
          1.61439, 1.22307, 0.935653, 0.721791, 0.560948,
          0.438863, 0.345438, 0.273418, 0.217525, 0.173879,
          0.139601, 0.112538, 0.0910654, 0.0739504, 0.0602499}
```

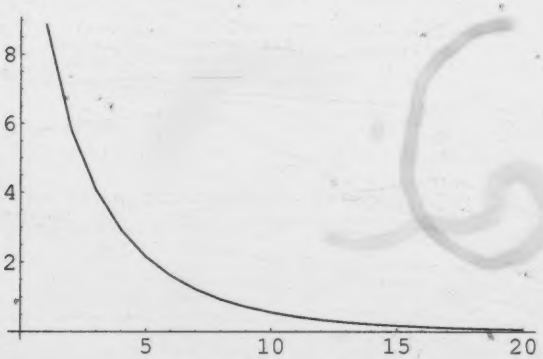


```
Out[52]= -Graphics-
```

Appendix C

Intra-arterial drug delivery

Typical drug administration is intravenous for internal malignancies or topical for treatment of superficial malignancies. There is still preferential accumulation of photosensitizer in malignant tissues, but it is not sufficient to avoid the possibility of collateral damage to tissues. Many methods of delivering the drug preferentially to the tumour have been studied to increase accumlation in malignant tissues. Intra-arterial administration of the photosensitizer forces the photosensitizer to be directly adminstered to the target volume. With the proper formulation of the drug, it embolizes in the microvasculature of the target. We studied the effects of intra-arterial drug adminstration to the canine prostate.

To determine the efficacy of intra-arterial administration, anesthetized (sodium pentobarbital 60mg/kg IV) large male mongrel dogs were examined for the time dependence of redistribution of 3 photosensitizers: free Aluminum phthalocyanine (AlPc) , Benzo-porphyrin derivative monoacid ring A (BPD-MA) , liposomal entrapped BPD-MA. A radiolabeled photosensitizer was co-administered with 99mTC-MAA. Following administration, the dogs were sacrificed at 20mins., 1h., 3h.. The pelvic tissues (bladder, prostate, urethra and rectum) was removed, cooled on ice for im-

mediate imaging using a gamma-camera. The prostate and surrounding tissues were divided into portions. Each portion was weighed and counted in a well counter to determine the relative amount of drug delivered. The cellular content of BPD-MA or AlPc was determined by spectrofluorometric assay. Tissue portions were homogenated, lysed in distilled water and a suspension generated with 2% sodium dodecyl sulfate and a 0.1N NaOH to yield soluble monomeric prodicts. Fluorescence was measured using a spectrofluorometer and converted to absolute concentrations from standard curves. Other representative portions were cryosectioned and examined with confocal scanning microscopy to determine the cellular location and relative amounts of photosensitizer. The optimum timing was determined to be only 20 minutes following intra-arterial injection. Accumulations were much greater in the prostate to the rectum were 100:1. Such high ratios lend confidence that a lethal drug/light combination may be delivered with decreasing probability of damaging proximate tissues. Of the 2 photosensitzers, liposomal BPD-MA was determined to be a more potent photosensitizer with higher relative accumulations in the prostate. Therefore, this photosensitizer was used in the preliminary studies to treat canine prostate.